

Development of TDEM system with SQUID and fluxgate for geophysical and NDE applications

By

IJEE MOHANTY

Enrolment No: PHYS02201504016

Indira Gandhi Centre for Atomic Research, Kalpakkam

A thesis submitted to the

Board of Studies in Physical Sciences

In partial fulfillment of requirements

for the Degree of

DOCTOR OF PHILOSOPHY

of

HOMI BHABHA NATIONAL INSTITUTE



February, 2021

Homi Bhabha National Institute

Recommendations of the Viva Voce Committee

As members of the Viva Voce Committee, we certify that we have read the dissertation prepared by **Ijee Mohanty** entitled “**Development of TDEM system with SQUID and fluxgate for geophysical and NDE applications**” and recommend that it may be accepted as fulfilling the thesis requirement for the award of Degree of Doctor of Philosophy.

Chairman - **Dr. N. V. Chandra Shekar**

N.V. Chandra Shekar
18/6/2021

Guide / Convener - **Dr. Awadhesh Mani**

Awadhesh Mani
18/6/2021

Examiner - **Prof. Dr. Hans-Joachim Krause**

By VC For Raj
18/06/2021

Member 1 - **Dr. B. P. C. Rao**

BPC Rao
18/6/2021

Member 2 - **Dr. S. Tripura Sundari**

S. Tripura Sundari
18/6/21

Member 3 - **Dr. R. Nagendran**

R. Nagendran
18/6/21

Final approval and acceptance of this thesis is contingent upon the candidate's submission of the final copies of the thesis to HBNI.

I hereby certify that I have read this thesis prepared under my direction and recommend that it may be accepted as fulfilling the thesis requirement.

Date: 18/06/2021

Place: Kalpakkom

Awadhesh Mani
Dr. Awadhesh Mani
(Guide)

STATEMENT BY AUTHOR

This dissertation has been submitted in partial fulfillment of requirements for an advanced degree at Homi Bhabha National Institute (HBNI) and is deposited in the Library to be made available to borrowers under rules of the HBNI.

Brief quotations from this dissertation are allowable without special permission, provided that accurate acknowledgement of source is made. Requests for permission for extended quotation from or reproduction of this manuscript in whole or in part may be granted by the Competent Authority of HBNI when in his or her judgment the proposed use of the material is in the interests of scholarship. In all other instances, however, permission must be obtained from the author.

Date: 18/06/2021

Place : Kalpakkam



Ijee Mohanty


DECLARATION

I, hereby declare that the investigation presented in the thesis has been carried out by me.

The work is original and has not been submitted earlier as a whole or in part for a degree / diploma at this or any other Institution / University.

Date: 18/06/2021

Place : Kalpakkam

A handwritten signature in black ink, reading "Ijee Mohanty". The signature is written in a cursive style with a large initial 'I' and a long, flowing 'M'.

Ijee Mohanty

List of Publications arising from the thesis

Journal

1. “Correlation of defect depth with diffusion time of eddy currents for the defects in conducting materials using transient eddy current NDE.”, Ijee Mohanty, R. Nagendran, A. V Thanikai Arasu, R. Baskaran, and A. Mani, *Meas. Sci. Technol.*, **2018**, Vol 29 (10), 10561.
2. “Characterization of TDEM System with SQUID and Fluxgate Magnetometers for Geophysical Applications.”, R. Nagendran and Ijee Mohanty, *IEEE Trans. Appl. Supercond.*, **2020**, Vol. 30 (2).
3. “Transient Eddy Current NDE System Based on Fluxgate Sensor for the Detection of Defects in Multilayered Conducting Material.”, R. Nagendran, Ijee Mohanty, A. V. Thanikai Arasu, and R. Baskaran, *J. Nondestruct. Eval.*, **2018**, Vol. 37 (3), pp. 1–6.
4. “Development of SQUID based TDEM system and its utilization for field survey at Tumallapalle, Andhra Pradesh, India”, Ijee Mohanty, R. Nagendran, Lata Bisht, A. V. Thanikai Arasu, R. Baskaran, B. V. L. Kumar, M. B. Verma, *J. Appl. Geophy.*, (Under Review).
5. “Observation of the dual behavior of the fluxgate magnetometer in Time Domain Electromagnetic (TDEM) field survey measurements.”, R. Nagendran, Ijee Mohanty, Lata Bisht; *J. Appl. Geophy.*, *J. Appl. Geophy.*, (Under Review).

Conference proceedings

1. “Development of SQUID based TDEM system for geophysical applications.”, R. Nagendran, A. V. T. Arasu, I. Mohanty, N. Chinnasamy, R. Baskaran, and A. Mani, *AIP Conference Proceedings*, **2017**, Vol. 1832, 060018.

Conference presentations

1. “Field test of low Tc SQUID based TDEM system for geophysical exploration.”, Ijee Mohanty, Lata Bisht, R. Nagendran; Oral presentation during *Applied Superconductivity Conference (ASC-2020)*, Virtual conference 2020 (Oct 24-Nov 07).
2. “Applicability of low Tc SQUID magnetometer for detection of buried conducting object.”, Ijee Mohanty, R. Nagendran, A V Thanikai Arasu, R. Baskaran, Awadhesh Mani; Poster presentation during *International Conference on Magnetic Materials and Applications (ICMAGMA)*, National Institute of Science Education and Research (NISER), Bhubaneswar, Odisha, India 2018 (December 9-13).
3. “Time Domain Electro-Magnetic geophysical survey with fluxgate magnetometer.”, Ijee Mohanty, R. Nagendran, A.V. Thanikai Arasu, P. Allipeera, R. Baskaran, Awadhesh Mani; Poster presentation during *Research Scholar Meet on Material Science and Engineering of Nuclear*

Materials (RSM-MSENM), HBNI, IGCAR, Kalpakkam, India, 2018 (May 7-9).

4. “Development of SQUID based TDEM system for geophysical application.”, R. Nagendran, A. V. T. Arasu, I. Mohanty, N. Chinnasamy, R. Baskaran, and A. Mani, poster presentation during *61st DAE Solid State Symposium (DAE SSPS)*, KIIT University, Bhubaneswar, Odisha, India 2016 (December 26-30).

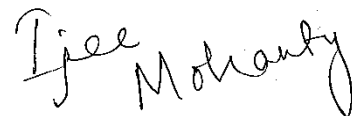
Publications not included in thesis

Journal

1. “A novel method for thickness measurement in conducting materials by apparent conductivity calculation through transient eddy current NDE.”, R. Nagendran, Lata Bisht, and Ijee Mohanty, *J. Nondestruct. Eval.*, **2021**, Vol. 40 (1), 30.

Conference proceedings

2. “Subsurface defect detection in conducting materials through transient eddy current NDE and apparent conductivity calculations.”, Lata Bisht, Ijee Mohanty and R. Nagendran, (Under Review).



Ijee Mohanty

DEDICATIONS

To my beloved parents

MAMATA and BIGYAN

ACKNOWLEDGEMENTS

This thesis would not have been a reality without the support and encouragement of many individuals. I would extend my sincere gratitude towards all of them.

First, I take this opportunity to thank my supervisor, Dr Awadhesh Mani (Scientific Officer-H and Head, Low Temperature Studies Section, IGCAR), for his invaluable support throughout my research. He has always been a source of motivation for me in difficult times during the research work.

I would like to express my sincere and heartfelt gratitude towards my Technology Advisor (TA), Dr R. Nagendran (Scientific Officer-H, SQUID and Application Section, IGCAR) for his undeniable support and encouragement. His intellectual inputs and guidance has immensely helped in my research and writing this thesis. I am extremely grateful towards him for making this thesis a success.

I thank my doctoral committee members Dr N. V. Chandra Shekar (Chairman), Dr B. P. C. Rao (Member) and Dr S. Tripura Sundari (Member) for their encouragement, helpful suggestions and time-to-time evaluation of the thesis work. I express my gratefulness towards Dr K. Gireeshen, Scientific Officer-G, and Mr R. Baskaran, Head-SQUID and Application Section (SAS) for supporting various experimental works for this thesis. I thank my colleagues Dr L. S. Vaidhyanathan, Mr N. Chinnasamy, Ms Lata Bisht, Mr A. V. Thanikai Arasu, Mr S. Sengottuvel and Mr Rajesh Patel and other members of SAS for their professional and personal support from time-to-time. I am also thankful to Dr. R. Rajaraman, Dean (Academic) for his efforts and sincerity which resulted in timely completion of the thesis work. I am thankful to former and present division heads of Condensed Matter Physics Division (CMPD) and group directors of Material Sciences Group (MSG) and director of IGCAR not only for providing me with the resources but

also for providing this wonderful environment of Kalpakkam, which has been my home during this journey.

This work also has commendable contributions from collaborators at the Atomic Mineral Directorate (AMD). I want to thank Mr P. Alliperra, Mr B. V. L. Kumar, Mr Murugan, and other AMD members for their support during the field survey conducted as part of this thesis work.

None of the work would have been possible without my friends and family members' emotional support and encouragement. I am eternally grateful to Surojit for providing me with immense strength and encouragement during this journey. I would also like to thank my dearest friends Shubhra, Fayaz, Pragyna, Teena, Alaka, Arpita, Anuj, Raktima, Manali, Twisha, Bijay, Gopi, Akshaya and Parvathy for supporting me in both good and bad times.

I would take this opportunity to thank my family members, particularly my siblings Ms Amrita Pattanayak and Mr Sthitapragnya Pattanayak for providing me with every support required throughout my career. I would also like to thank Ms Saswata Subhadarshini for lending me an ear whenever needed. Finally, I express my deepest gratitude to my sister Mrs. Smita Mohanty, brother-in-law Dr Dharani Dhar Das, brother Mr Abinash Mohanty, and my parents Mrs Mamata Pattanayak and Mr Bigyan Bhusan Mohanty. It is their faith in me that has resulted in the fruitful career that I have.

Apart from the people referred above, many others have helped me in numerous ways throughout this work — my sincere gratitude to those whom I could not mention here.


Ijee Mohanty

Table of contents

| | |
|----------------------------|--------|
| Table of contents | xvii |
| Abstract | xxi |
| List of Figures | xxiii |
| List of tables | xxxix |
| List of Abbreviations..... | xxxiii |
| List of Symbols | xxxv |

Chapter 1 INTRODUCTION TO GEOPHYSICAL EXPLORATION AND NDE TECHNIQUES1

| | |
|---|----|
| 1.1. Introduction | 1 |
| 1.1.1. Various geophysical techniques | 2 |
| 1.1.2. Various NDE techniques | 6 |
| 1.2. Different EM induction techniques..... | 8 |
| 1.3. TDEM and its application | 11 |
| 1.3.1. TDEM in geophysical survey | 11 |
| 1.3.2. TDEM in NDE | 14 |
| 1.4. Sensors for TDEM applications | 17 |
| 1.5. Motivation and brief outline of thesis | 18 |
| 1.5.1. Motivation | 18 |
| 1.5.2. Outline of the thesis | 21 |

Chapter 2 DEVELOPMENT OF SQUID BASED TDEM SYSTEM FOR GEOPHYSICAL APPLICATIONS23

| | |
|---|----|
| 2.1. Introduction | 23 |
| 2.2. Working principle of TDEM | 24 |
| 2.2.1. Data processing in TDEM measurements | 25 |
| 2.2.2. General scheme used to eliminate power line noise..... | 27 |
| 2.3. Sensors used in the work..... | 28 |
| 2.3.1. Induction coil..... | 28 |
| 2.3.2. Fluxgate magnetometer | 31 |
| 2.3.3. SQUIDS | 34 |
| 2.3.4. SQUIDS with Additional Positive Feedback (APF)..... | 39 |
| 2.4. Integration and performance testing of TDEM system with portable transmitter loop | 43 |
| 2.5. TDEM experiments with induction coil as receiver | 46 |
| 2.6. TDEM experiments with SQUID as receiver | 49 |

| | |
|---|-----------|
| Chapter 3 TDEM SURVEY AT TUMALAPALLE USING SQUID, INDUCTION COIL AND FLUXGATE..... | 53 |
| 3.1. Introduction..... | 53 |
| 3.2. Simulations of central loop sounding results using synthetic forward models ... | 55 |
| 3.2.1. Effect of increasing transmitter current..... | 58 |
| 3.2.2. Effect of increasing number of turns of the transmitter loop | 59 |
| 3.2.3. Effect of increasing the area of the transmitter loop | 60 |
| 3.3. Central loop sounding test at Kalpakkam (Site 1) | 61 |
| 3.3.1. Experimental details and results..... | 62 |
| 3.4. Central loop TDEM survey at Tumallapalle (Site 2)..... | 63 |
| 3.4.1. Details of terrain..... | 63 |
| 3.4.2. Experimental details | 64 |
| 3.4.3. Results and discussion..... | 66 |
| 3.4.4. Modeling and estimation of the depth of conducting layer..... | 71 |
| 3.5. Conclusion | 73 |
| Chapter 4 DUAL BEHAVIOR OF THE FLUXGATE MAGNETOMETER IN TDEM GEOPHYSICAL MEASUREMENTS | 75 |
| 4.1. Introduction..... | 75 |
| 4.2. Preliminary observation of the dual behavior of the fluxgate magnetometer..... | 76 |
| 4.3. Comparison of TDEM experimental results performed with portable transmitter by using fluxgate and SQUID as receivers..... | 79 |
| 4.4. Explanation for the negative response of the fluxgate in TDEM measurements with typical TDEM output waveforms for an induction coil and magnetometer | 84 |
| 4.5. TDEM measurements in the field with larger transmitter loops | 88 |
| 4.6. Laboratory simulation experiments with fluxgate sensor for the confirmation of its dual behavior in TDEM measurements | 91 |
| 4.7. Additional voltage generation with different frequency at the output of the fluxgate | 94 |
| 4.8. Conclusion | 98 |
| Chapter 5 DEVELOPMENT OF TRANSIENT EDDY CURRENT NDE SYSTEM FOR DETECTION OF DEFECTS IN CONDUCTING MATERIALS | 99 |
| 5.1. Introduction..... | 99 |
| 5.2. Principle of operation of transient eddy current NDE technique..... | 105 |
| 5.3. Advantages of magnetometer over an induction coil | 106 |
| 5.4. Advantages of double “D” excitation Coil | 107 |
| 5.5. Fluxgate based transient eddy current NDE System | 108 |

| | |
|--|-------------------|
| 5.6. Experimental details..... | 112 |
| 5.7. Results and discussion | 114 |
| 5.8. Conclusion | 122 |
| <i>Chapter 6 SUMMARY AND FUTURE SCOPE</i> | <i>123</i> |
| 6.1. Summary | 123 |
| 6.2. Future scope | 124 |
| <i>References</i> | <i>127</i> |

List of Figures

| | | |
|---------|---|----|
| Fig 1.1 | Illustration of (a) passive and (b) active electromagnetic geophysical exploration techniques. | 8 |
| Fig 1.2 | Illustrative representation showing different skin depth δ in two conductive objects with identical electrical conductivity σ and magnetic permeability μ with applied excitation signal of two different frequencies. The width of the dotted lines represents strength of the eddy current. | 10 |
| Fig 1.3 | Geophysical exploration for buried conductive targets based on TDEM technique; the dashed red lines represent primary magnetic fields while the blue ones represent secondary magnetic fields. | 12 |
| Fig 1.4 | Different configuration of TDEM based geophysical survey setup: (a) single loop, (b) coincident loop, (c) in loop, (d) Slingram-type, (e) fixed loop and moving receiver; the transmitter is shown in black while the receiver is shown in red color. | 13 |
| Fig 1.5 | Illustration of electromagnetic induction based NDE setup | 15 |
| Fig 2.1 | (a) Current in the transmitter loop or primary magnetic field produced by the transmitter loop, (b) electromotive force induced in the ground due to the changes of the primary magnetic field, and the net magnetic field measured by (c) an induction coil and (d) a magnetometer. | 25 |
| Fig 2.2 | Data processing for the TDEM measurements with a magnetometer. (a). Current in the transmitter loop (dotted line) and decay of the secondary magnetic field (b) Inversion of the negative decay of the secondary magnetic field (c) Averaging and window averaging of the decay of the secondary magnetic field. | 26 |
| Fig 2.3 | Data processing for the TDEM measurement with an induction coil. (a) Current in the transmitter loop (dotted line) and decay of the secondary magnetic field (b) Inversion of the negative decay of the secondary magnetic field (c) Averaging and window averaging of the decay of the secondary magnetic field. | 26 |
| Fig 2.4 | Example of data processing showing (a) raw data with 8 stacks, (b) Averaging of positive and negative transients (inset shows the presence of large power line noise), (c) inversion of negative transient and averaging with positive transient (inset shows the reduction of power line noise) and (d) final window averaged transient decay. | 27 |
| Fig 2.5 | Circuit diagram of the amplifier designed for the induction coil | 30 |
| Fig 2.6 | Photographs of the (a) amplifier and the (b) induction coil with amplifier. | 30 |
| Fig 2.7 | (a) Noise in time domain, (b) spectral density of the field noise measured by placing the induction coil at the center of the long μ -metal cylinder. | 31 |

| | | |
|----------|---|----|
| Fig 2.8 | Block diagram of rod shaped double core fluxgate magnetometer with readout electronics. | 32 |
| Fig 2.9 | Photograph of the Bartington's three-axis fluxgate magnetometer Mag-03MCL-100 | 33 |
| Fig 2.10 | (a) Noise in time domain and (b) spectral density of the field noise of the fluxgate magnetometer measured inside the MSR. | 34 |
| Fig 2.11 | (a) Schematic configuration of the DC SQUID and (b) I-V characteristics of the DC SQUID when the external magnetic flux coupled to the SQUID. | 36 |
| Fig 2.12 | Schematic diagram of the flux readout electronics operated with flux modulation scheme. | 39 |
| Fig 2.13 | (a) Schematic view and (b) photograph of the Magnicon multi-loop SQUID. | 40 |
| Fig 2.14 | Schematic view of the direct readout electronics of the SQUID with APF | 41 |
| Fig 2.15 | Typical transmitter waveform with half period for a transmitter loop size of 100 m x 100 m and with transmitter current of 20 A. | 41 |
| Fig 2.16 | (a) Typical output of the multi-loop SQUID optimum bias current I_b , bias voltage V_b and bias flux Φ_b (b) V- Φ curve of the SQUID for the input flux of one flux quantum without optimum and with optimum values I_b , V_b and Φ_b . | 42 |
| Fig 2.17 | (a) Noise recorded in time domain and (b) spectral density of the field noise of the SQUID magnetometer measured inside the MSR | 43 |
| Fig 2.18 | (a) Schematic view of the SQUID based TDEM setup with transmitter loop of 2 m x 2 m, (b) Photograph of the FRP liquid helium cryostat with SQUID probe and transmitter loop and (c) Output of the SQUID when the current (equivalent to $40 \Phi_0$) passing through the transmitter is suddenly switched off. | 44 |
| Fig 2.19 | Images showing the typical output screens displaying (a) raw data, (b) stacked data, (c) decay and, (d) profile recorded using a magnetometer. | 45 |
| Fig 2.20 | (a), (b) and (c) are the decay of the secondary magnetic field recorded by the induction coil for the aluminum plate with thickness of 2 mm, 4 mm and 6 mm moving away from the center of the transmitter respectively and the corresponding enlarged views with time decay between 2 ms and 12 ms are shown in (d), (e) and (f). | 47 |
| Fig 2.21 | Field profile recorded by using an induction coil perpendicular to the plane of the transmitter loop (z component) for the aluminum plates with thicknesses of (a) 2 mm, (b) 4 mm and (c) 6 mm. | 48 |
| Fig 2.22 | (a) Changes of the induction coil output at different time gates for the aluminum plate thicknesses of 2 mm, 4 mm and 6 mm (b) enlarged view of the same. | 48 |

| | | |
|----------|---|----|
| Fig 2.23 | (a), (b) and (c) are the decay of the secondary magnetic field recorded by the induction coil for the aluminum plate with thickness of 2 mm, 4 mm and 6 mm moving away from the center of the transmitter respectively and the corresponding enlarged views with time decay between 2 ms and 12 ms are shown in (d), (e) and (f). | 50 |
| Fig 2.24 | Field profile recorded by using SQUID sensor perpendicular to the plane of the transmitter loop (z component) for the aluminum plates with thicknesses of (a) 2 mm, (b) 4 mm and (c) 6 mm. | 51 |
| Fig 2.25 | Changes of the SQUID output at different time gates for the aluminum plate thicknesses of 2 mm, 4 mm and 6 mm. | 51 |
| Fig 2.26 | Profile recorded by the induction coil at early and late time gates for the aluminums plates with thickness of (a) 2 mm, (b) 4 mm and (c) 6 mm. | 52 |
| Fig 2.27 | Profile recorded by the SQUID for the aluminum plates with thickness of (a) 2 mm, (b) 4 mm and (c) 6 mm. | 52 |
| Fig 3.1 | Maxwell plate model showing top plate (P1) used for overburden simulation and bottom plate (P2) for conductive target below intermediate resistive layer. | 56 |
| Fig 3.2 | Plots in log-log scale showing vertical magnetic field response of a layered model with a square transmitter loop of side length of 100 m and current of 5 A. | 57 |
| Fig 3.3 | Simulated log-log plots showing decay of vertical component of secondary magnetic field over a layered model for different Tx currents using one turn square transmitter loop of side length of 100 m. | 58 |
| Fig 3.4 | Primary magnetic field versus depth for different transmitter currents. | 58 |
| Fig 3.5 | Simulated plots in log-log scale showing decay of vertical component of secondary magnetic field over a layered model for different turns of Tx loop with 25 A current transmitted using the loop of side 100 m. | 59 |
| Fig 3.6 | Variation of magnetic field with depth below the surface with different Tx turns. | 59 |
| Fig 3.7 | Simulated log-log plots showing decay of vertical component of secondary magnetic for Tx loops of different sizes with transmitter current of 25 A. | 60 |
| Fig 3.8 | Variation of primary magnetic field versus depth with transmitters of different sizes. | 61 |
| Fig 3.9 | Satellite image showing coordinates of the corners of square transmitter loop of side 100 m and the of loop where the SQUID magnetometer is placed during measurement at Site 1. | 62 |
| Fig 3.10 | Transients showing decay of vertical component of secondary magnetic field recorded at Site 1 using SQUID sensor for transmitter currents of different base frequencies. | 63 |

| | | |
|----------|--|----|
| Fig 3.11 | The stratigraphy of the terrain | 64 |
| Fig 3.12 | Satellite image showing coordinates of the transmitter loop with side length of 400 m along with photographs showing the data acquisition system and the partially buried SQUID at center of the loop and location of transmitter and batteries. | 65 |
| Fig 3.13 | Plots in log-log scale showing decay of the vertical component of the secondary magnetic field recorded with base frequency of 6.25 Hz using induction coil with transmitter loop size of (a) 100 m x 100 m, and (b) 400 m x 400 m. Similarly, (c) and (d) correspond to decay of the secondary magnetic field recorded using SQUID with transmitter loop size of 100 m x 100 m and 400 m x 400 m respectively with the same base frequency. | 66 |
| Fig 3.14 | Decay of the vertical component of the secondary magnetic field recorded with base frequency of 6.25 Hz and with transmitter loop size of 400 m x 400 m using (a) induction coil, (b) fluxgate, and (c) SQUID. | 67 |
| Fig 3.15 | The decay of the secondary magnetic field (log-log scale) recorded by (a) SQUID and (b) induction coil with different base frequencies for transmitter loop of side length 100 m with applied current of 25 A. | 69 |
| Fig 3.16 | The decay of the secondary magnetic field (log-log scale) recorded by (a) SQUID and (b) induction coil with different base frequencies for transmitter loop of side length 400 m with applied current of 27 A. | 70 |
| Fig 3.17 | Layered model showing top plate P1 (conductive overburden) and bottom plate P2 (buried target layer) at depth of 285m. | 72 |
| Fig 3.18 | Vertical magnetic field decay response showing in log-log scales for simulated and experimental data. | 72 |
| Fig 4.1 | (a) Decay of the secondary magnetic field for the central loop sounding measurements with fluxgate as a receiver (b) Enlarged view at the earlier time. | 77 |
| Fig 4.2 | (a) Schematic diagram of the TDEM system with fluxgate receiver and transmitter loop of 2 m x 2 m and (b) Photograph of the TDEM system with fluxgate. | 78 |
| Fig 4.3 | The decay of the secondary magnetic field recorded by the SMARTem24 with SQUID as a receiver when the aluminum plate approaches SQUID system. (a), (b) and (c) are the entire decay profiles for the plate thicknesses of 2 mm, 4 mm and 6 mm respectively and (d), (e) and (f) are the corresponding enlarged view of the decay profile where the signal change occurred at larger value. | 80 |
| Fig 4.4 | Change of the secondary magnetic field recorded by the SQUID with positional scan coordinates for the aluminum plates with a thickness of (a) 2 mm, (b) 4 mm and (c) 6 mm at different time gates (From top to bottom - early, intermediate and late time gates). | 81 |

| | | |
|----------|---|----|
| Fig 4.5 | The decay of the secondary magnetic field recorded by the SMARTem24 with fluxgate as a receiver when the aluminum plate approaches fluxgate. (a), (b) and (c) are the entire decay profiles for the plate thicknesses of 2 mm, 4 mm and 6 mm respectively and (d), (e) and (f) are the corresponding enlarged view of the decay profile where the signal change occurred at larger value. | 82 |
| Fig 4.6 | Change of the secondary magnetic field recorded by the fluxgate with positional scan coordinates for the aluminum plates with a thickness of (a) 2 mm, (b) 4 mm and (c) 6 mm at different time gates (From top to bottom - early, intermediate and late time gates). | 83 |
| Fig 4.7 | Change of the secondary magnetic field recorded by the fluxgate with positional scan coordinates for the aluminum plates with a thickness of 2 mm and transmitter current of (a) 0.212 A (b) 2 A at different time gates. | 84 |
| Fig 4.8 | Schematic view of the TDEM waveforms (a) Typical shape of the current pulse applied to the transmitter loop (left) and typical TDEM central loop configuration, (b) Net magnetic field measured by the magnetometer and data processing [(b1) raw data , (b2) stacked and averaged with suitable inversion and (b3) final window averaged)] and (c) Net magnetic field measured by an induction coil and data processing [(c1) raw data , (c2) stacked and averaged with suitable inversion and (c3) final window averaged)]. | 85 |
| Fig 4.9 | The schematic representation of the decay profiles for different targets with different sensors (magnetometer and an induction coil) in TDEM measurements. (a) and (b) are the decay profiles of the conductive and resistive targets measured with magnetometer and induction coil respectively and (c) and (d) are the decay profiles measured with the fluxgate sensor which behaves like a combination of both magnetometer and an induction coil for the conductive and resistive targets respectively. | 86 |
| Fig 4.10 | (a) Schematic diagram of the TDEM system. (b) Photograph of the setup with SQUID and (c) fluxgate in the field. | 88 |
| Fig 4.11 | Decay profile recorded by the fluxgate and SQUID with different sizes of the transmitter loop and transmitter currents, (a) and (b) are log-log plots of the decay profile recorded by the Fluxgate and SQUID respectively, (c) and the inset of (c) are semi log plots of the decay profile (the region where the output of the fluxgate reaches to a negative value) recorded by the fluxgate with transmitter loop size of 100 m x 100 m and 400 m x 400 m respectively, (d) difference between field recorded using SQUID and fluxgate. | 90 |
| Fig 4.12 | Primary magnetic field produced by the transmitter loop A and B along its axis. | 90 |
| Fig 4.13 | Schematic diagram and photograph of the experimental setup with fluxgate. | 92 |

| | | |
|----------|---|-----|
| Fig 4.14 | The predominant peak voltages and the corresponding frequencies measured at the output of the fluxgate for the input magnetic field with different frequencies. (a) The frequency of the voltage at the output of the fluxgate which is proportional to the input magnetic field is same as the input frequency of the magnetic field where as the frequency of the output voltage which is proportional to the rate of change of magnetic field is different from the input frequency. (b) The frequencies of the fluxgate output voltage ($f_{\text{ref}} - f_{\text{sig}}$) and ($f_{\text{ref}} + f_{\text{sig}}$) for the given input magnetic field at different frequencies. | 92 |
| Fig 4.15 | Schematic diagram of the fluxgate with its readout electronics | 94 |
| Fig 4.16 | Spectrum showing signals for f_{ref} , ($f_{\text{ref}} - f_{\text{sig}}$) and ($f_{\text{ref}} + f_{\text{sig}}$) for (a) $f_{\text{sig}} = 8$ kHz, (b) $f_{\text{sig}} = 9$ kHz and (c) $f_{\text{sig}} = 10$ kHz, (d) $f_{\text{sig}} = 11$ kHz, (e) $f_{\text{sig}} = 12$ kHz | 96 |
| Fig 5.1 | Illustration of the eddy current NDE system showing eddy currents in conducting specimen in (a) frequency domain using sinusoidal excitation signal of (i) higher frequency and (ii) relatively lower frequency. For given conductivity and permeability, skin depth is inversely proportional to frequency and thus, depth of investigation is limited by excitation frequency. However, (b) pulsed excitation used in time-domain consists of continuum of frequencies; each diffusion depth corresponds to a transient time and thus, different depths can be investigated using same excitation. Here, strength of the current is proportional to line thickness of the eddy current loops. | 103 |
| Fig 5.2 | (a) Excitation current in the form of trapezoidal pulses applied to the excitation coil, (b) primary magnetic field generated as a result of the excitation current, (c) resultant field measured by magnetic field sensor, (d) generation of eddy current and its associated secondary magnetic field in conducting specimen, (e) decay of secondary field after processing and (f) perturbation of eddy currents due to the presence of defect in conducting specimen. | 105 |
| Fig 5.3 | (a) Aluminum plates without defect; (b) 1.5 thick Aluminum plate with defect. | 109 |
| Fig 5.4 | Schematic of the double “D” excitation coil, (b) three-axis fluxgate magnetometer, photographs of (c) double “D” excitation coil, (d) the fluxgate magnetometer and (e) schematic view of the orientation of the double “D” excitation coil and fluxgate magnetometer | 110 |
| Fig 5.5 | Block diagram of the fluxgate based TDEM NDE system | 112 |
| Fig 5.6 | Photograph of the fluxgate based TDEM NDE system | 113 |
| Fig 5.7 | (a) Pictorial representation of the eddy current flow patterns due to the double ‘D’ excitation coil in the vicinity of a defect (from (A) to (E)) and corresponding decay transients for a defect at a depth of 4 mm and 6 mm below the surface. (b) Field profile derived from the decay transients recorded by scanning across the defect where the maximum eddy current perturbation occurs. | 114 |

| | | |
|----------|---|-----|
| Fig 5.8 | Decay of the differential secondary magnetic field at different positions for the defect located at a depth of 2 mm | 115 |
| Fig 5.9 | Profile plots showing decay of secondary magnetic fields for defect at a depth of 2 mm at (a) early, (b) intermediate and (c) late time windows | 116 |
| Fig 5.10 | Decay of the differential secondary magnetic field at different positions for the defect located at a depth of 10 mm. | 117 |
| Fig 5.11 | Profile plots showing decay of secondary magnetic fields for defect at a depth of 10 mm at (a) early, (b) intermediate and (c) late time windows. | 118 |
| Fig 5.12 | (a) Decay and (b) profile plots for changes of secondary magnetic field due to defect at depth of 20 mm. | 119 |
| Fig 5.13 | Changes of secondary magnetic field with decay times for defect at different depths | 120 |
| Fig 5.14 | Square root of diffusion time (t_m) for defect located at various depths. | 121 |

Chapter 6

SUMMARY AND FUTURE SCOPE

This chapter summarizes the major outcomes of the thesis and provides an idea about future scope for further research.

6.1. Summary

This thesis focused on the development of a SQUID based TDEM system and its utilization for geophysical exploration in a terrain where a thin conducting object is buried under thick resistive layer. While advantages of using a magnetometer such as SQUID instead of conventional induction coil are emphasized, the drawback of using a fluxgate magnetometer for TDEM survey is also detailed. In addition to this, a fluxgate based transient eddy current NDE technique to detect subsurface defects in conducting material is also described. The major outcomes of the thesis are summarized below:

A SQUID based TDEM system was developed by integrating a multi-loop SQUID magnetometer as receiver and commercial transmitter, transmitter controller and data acquisition system.

In order to compare the performance of the SQUID based system with induction coil which has been conventionally used as receiver; an induction coil along with its amplifier was designed and developed.

The TDEM system was tested at the laboratory level using a small square transmitter loop of side length of 2 m and set of Aluminum plates as targets. Comparing the performance of SQUID and induction coil in such TDEM test, it was concluded that SQUID sensor is more suitable to locate the conducting target buried in deep sub-surface of the earth due to its extremely high sensitivity maintained at low frequency.

The TDEM system was further utilized for central loop TDEM sounding measurements at YSR Kadapa district of Andhra Pradesh, India where the terrain consists of a thin conductive target buried under thick resistive layer. Here, in order to compare the performance of different sensors, the induction coil, the SQUID magnetometer and a commercial fluxgate magnetometer were used as receiver. The results of the TDEM measurements using different transmitter moments and different receivers showed that sensitive magnetometers such as SQUID and larger transmitter moments are essential to delineate such buried conductive targets below thick resistive subsurface.

The reason for anomalous response of the fluxgate magnetometer during the TDEM central loop sounding measurements was further investigated and through laboratory simulation experiments, it was verified that the fluxgate magnetometer behaves like an induction coil at early times and as a magnetometer at late times during the transient decay.

A transient eddy current NDE system was developed using the commercial fluxgate magnetometer as sensor and a double “D” differential excitation coil. The system was utilized to detect defect in stack of Aluminum plates up to depth of 20 mm. The parameter diffusion time, “ t_m ”, was obtained from the experimental results and a linear correlation between “ $\sqrt{t_m}$ ” and depth of the defect was demonstrated.

6.2. Future scope

The thesis emphasized the advantage of TDEM technique over FDEM in eddy current measurement systems. The work also detailed the importance of use of magnetometers in transient eddy current measurements and further details the development and utilization of a SQUID based TDEM system in geophysical exploration surveys. During the TDEM measurements, it was observed that the decaying secondary magnetic field reached negative values at later time. A substantial instrumental drift from higher value towards a

lower value was observed in the raw data. Further experiments can be performed to investigate the reason and improve the system performance.

The thesis also described the benefit of improved transmitter moment on the depth of investigation. Thus, SQUID based central loop sounding experiments can be performed by introducing the SQUID sensors with different sensitivities (such as $7 \text{ nT}/\Phi_0$) in the SQUID system in order to enhance the investigation depth by increasing the transmitter moment.

The transient eddy current NDE system described in the thesis provides a technique to correlate the depth of subsurface defect in conducting metals to experimentally obtained diffusion time, " t_m ". Further work can also be extended for measurement of thickness of metals and thin conductive coatings by combining transient eddy current NDE and calculation of apparent conductivity. Systems using differential as well as absolute induction coil sensors can also be designed for thickness measurement in metallic tubes using such technique. This may find application in detection of corrosion in metallic parts

Abstract

Electromagnetic induction methods have been widely used for geophysical exploration of potential resources as well as non-destructive evaluation (NDE) of conducting specimen such as detection of subsurface flaws. Time Domain Electromagnetic (TDEM) technique is one of the widely used electromagnetic geophysical techniques to obtain the electrical resistivity of the earth. In this technique, magnetic field in the form of pulses is applied to the ground to induce eddy currents into the ground. In response, the decay of these eddy currents and the associated secondary magnetic field is sensed by a suitable sensor. Similar pulsed excitation can be used to induce eddy currents into conducting metal specimen and the response can be recorded. The presence of subsurface flaws alters the path of eddy currents resulting in perturbations in the corresponding secondary magnetic fields thus providing signature of presence of flaws in the specimen.

The decaying magnetic field in such electromagnetic measurements can be measured using an induction coil or a magnetic field sensor such as fluxgate or Superconducting QUantum Interference Device (SQUID). The voltage induced in the induction coil is proportional to the rate of change of the secondary magnetic field; this induced voltage decays faster than the decay of the secondary magnetic field itself. In contrast, the magnetic field sensor such as SQUID directly measures the magnetic field and hence it enhances the depth of investigation.

The goal of this thesis is the development and utilization of a SQUID based TDEM system and its utilization in geophysical exploration of buried conductive targets. Locating a thin conducting layer which is covered by a thick and highly resistive layer is a challenging task due to the induction of weak eddy currents in the upper resistive layer. TDEM central loop sounding measurements have been carried out by using the developed SQUID system in such a terrain to probe the conductive target buried under a thick and

highly resistive layer. The decay results have been analyzed and compared to simulated models to verify the presence of the conducting layer. The system performance has also been compared with the central loop sounding measurements performed with an induction coil sensor and fluxgate magnetometer.

While conducting experimental TDEM tests using the fluxgate magnetometer, it was observed that the output of the fluxgate reached negative values. Subsequently, simulation experiments were performed at the laboratory and it was confirmed that the fluxgate shows dual behavior. This means that the fluxgate behaves as an induction coil at early times of the transient and as a magnetometer in late times.

Similarly, by using the same TDEM system, a novel transient eddy current NDE technique has been established for the detection of defects in conducting materials with a fluxgate magnetometer and by using a double “D” differential excitation coil. This NDE system is utilized for the detection of defect in an aluminum plate at different depths ranging from 2 mm to 20 mm, in steps of 2 mm, below the surface of a stack of flawless aluminum plates. From these results, it has been shown that the diffusion time, “ t_m ”, at which the decay of the eddy current due to the defect reaches maximum directly provides information about the depth of the defect.

Therefore, the work in the thesis shows that for deeper geophysical investigation of conductive targets buried under thick resistive overburden, a transmitter loop with larger area and sensitive magnetometer such as SQUID are indispensable. The use of fluxgate magnetometers should also be avoided in such transient measurements where the time rate of change of magnetic field is extremely high. In addition to this, the NDE technique presented in this thesis provides a direct way to correlate the depth of defect in conducting specimen with diffusion time, “ t_m ”.

Chapter 1

INTRODUCTION TO GEOPHYSICAL EXPLORATION AND NDE TECHNIQUES

This chapter provides (1) an introduction to various geophysical exploration as well as non-destructive evaluation techniques; (2) Time Domain Electromagnetic induction (TDEM) technique and its applications; (3) sensors used in TDEM based geophysical exploration; and (4) motivation and a short outline of the thesis.

1.1. Introduction

The quest for valuable assets buried under the earth can be traced back to the beginning of civilizations. Since then, humans have tried to dig the earth to obtain important resources for their needs. With population growing at a fast pace, the demand for minerals, oil, and natural gas has also peaked. Over time, human society has developed several methods for the feasible extraction of resources from nature. Today, the importance of mineral exploration has shifted from just a household requirement to paving the path of development for a nation. Although many of the minerals are found in the upper layers of the earth, they are very low in concentration and their extraction may not produce feasible output. The continuous need for both metallic and non-metallic minerals, oil, and gas has increased the necessity to develop techniques for deeper exploration to be able to extract economically viable minerals. Mineral deposits are strongly related to the terrain that hosts them. Therefore, it is also important to have knowledge of the mineral deposit and its geologic environment.

Exploring and extracting minerals from deep deposits requires multi-disciplinary approach which include profound knowledge and expertise in geology, geochemistry, geophysics as well as drilling [1]. Geology provides information about the geological backdrop in which the potential mineral deposit exists. Various geophysical techniques

can then be applied to obtain detailed mapping and quantification of the potential deposits. Accordingly, an extraction technique is determined and finally the minerals are mined and further analyzed using suitable geochemical approaches. Geophysical methods have also proven to be useful for extraction of archaeological information as well as helped in solving environmental problems such as detecting unidentified ordnances, urban geological mapping, locating cavities or voids, dam or reservoir leaks, landfill boundaries and many more [2–5].

Similarly, non-destructive evaluation (NDE) of material aims to extract information about physical, mechanical, chemical, and/or metallurgical properties of material without affecting its serviceability. Every system or structure is composed of various metallic/non-metallic components that may have manufacturing defects or may exhibit degradation during service over a period of time. NDE is essential to detect defects and underlying corrosion of material that occur during manufacturing or post-manufacturing wear and tear. In order to use NDE for quality assurance, surface preparation is not necessary and this leads to reduction in cost as well as inspection time. Non-destructive evaluation finds applications in the aerospace, automotive, petrochemical, defense and manufacturing industries. Therefore, it is essential to develop reliable NDE methods for regular health monitoring as well as in-service inspection and assessment of residual life.

The subsequent subsections highlight the most commonly used geophysical and NDE techniques.

1.1.1. Various geophysical techniques

The first step towards successfully obtaining information on any buried target is to adopt a proper geophysical exploration technique. There are number of approaches to geophysical exploration which vary with the factors such as type and quality of target, availability of the requisite technique and expertise, feasibility of exploration and

extraction [6]. The earth comprises of numerous components like clay, shale as well as mineral ores with varying physical properties such as magnetic susceptibility, electrical conductivity, density, and acoustic velocity. More often, geophysical exploration comprises of a suitable amalgamation of methods such as gravity, seismic and electromagnetic to measure physical properties of the earth's subsurface as well as the anomalies present in it [7,8]. Analyses of such measurements reveal variation of physical properties both laterally and vertically. Table 1.1 summarizes the various geophysical techniques used for exploration and survey based on the properties of the target. Of all the methods mentioned in Table 1.1 methods such as magnetic and magnetotelluric (MT) are passive methods which do not need a trigger. On the contrary, seismic, direct current (DC) resistivity, frequency domain and time domain electromagnetic are some of the methods that can be categorized as active geophysical methods and require an excitation to generate the response.

Seismic survey technique is employed to understand subsurface discontinuities, possible intruding structures, layering, and investigation of minerals or huge metal deposits. An explosion producing acoustic waves serves as the source of seismic waves and an array of receivers known as geophones are used to record the reflected/refracted acoustic waves from different layers of the earth [9,10].

Magnetic field is another physical property which can be used to identify buried mineral resources such as pyrrhotite and magnetite with natural magnetic fields. A magnetic survey can be utilized to identify such materials using a magnetic field sensor called magnetometer such as a proton precision magnetometer. In addition to mineral exploration, magnetic survey technique can also be utilized in archaeology and solving geotechnical problems such as finding buried iron structures [11,12].

Similarly, gamma radiometry is the investigation of the earth using gamma rays emitted by naturally occurring radio elements in the earth such as thorium and uranium. Both airborne and ground-based radiometry techniques are commonly used as preliminary survey to assess the availability of renewable energy resources [13,14]. The density of different rocks beneath the earth's crust varies from place to place. This density can be estimated by measuring the gravitational field above the surface. Absolute and differential gravimeters are used in gravity geophysical survey to obtain information about subsurface rocks based on their density [15].

Electrical resistivity is another important physical parameter that can be used to understand subsurface layers and/or buried conductive bodies. The DC resistivity and the electromagnetic methods are employed to identify targets using their resistivity. The DC resistivity technique can be used to image the subsurface of the earth on both water and land, in two-dimensional sections and/or three-dimensional volumes. This technique uses an array of electrodes to inject a direct current into the ground. The path of currents depends on the variation of resistivity in the subsurface. Good conductors allow the flow of currents through them while the resistors do not. Electrical charges building up at interfaces separate bodies with different conductivity and generate a potential difference which is measured at the surface or in a borehole. Such measurements at many different locations are performed to obtain a spatial image of subsurface resistivity distribution [16]. DC resistivity technique finds application in estimating depth to bedrock and water tables, mapping geological features such as fracture zones, delineating quarry deposits, measure earth impedance for laying grounding circuits [17]. However, this technique requires longer current carrying wires even for investigation of shallow depths, thus making it less efficient for large scale surveys. The transmission of current is difficult in terrains such as deserts where resistivity of upper layer is very high. Signals from DC resistivity

measurements are also highly affected by lateral variations which renders this technique disadvantageous for 1-dimensional interpretation of conductivity versus depth [18,19]

Electromagnetic technique is another geophysical survey method in which a magnetic field is induced into the subsurface, resulting in eddy current and an associated secondary magnetic field. The decay of the eddy current and its associated secondary magnetic field is influenced by the electrical property of the subsurface or the target. The rate of decay of eddy current can be measured by recording the associated voltage using an induction coil or by measuring the change in secondary magnetic field using a magnetometer [20].

During such electrical or electromagnetic geophysical surveys, sometimes the measured voltage shows induced polarization (IP) effects. This IP effect arises as a result of the capability of rocks to hold the electrical charge for a brief period after the turn-off of the transmitter current. Such effects can be used to obtain valuable information such as faults, geological structures or mineralization. Mapping IP effects, in particular, helps in delineating pyrite crystals that occur above hydrocarbon mineralization [21].

Table 1.1 Geophysical exploration methods based on physical characteristics of targets.

| PHYSICAL CHARACTERISTICS | GEOPHYSICAL METHODS | PROSPECTION TECHNIQUE |
|--|--------------------------------|------------------------------------|
| Electrical resistivity/conductivity | DC Resistivity | Resistivity profiling and sounding |
| | Electromagnetic | MT, FDEM, TDEM |
| Acoustic velocity | Seismic | Reflection, Refraction |
| Density | Gravity | Gravity gradiometer, Microgravity |
| Gamma radiation | Radiometric survey | |
| Charge ability | Induced polarization | |
| Magnetism | Magnetic field measurements | |
| Dielectric constant | Ground-penetrating radar (GPR) | |

Using such geophysical methods, potential resources can be identified. Once potential resources are identified using such non-invasive geophysical exploration methods, more rigorous technique of drilling is used to obtain information on the suitability for building a mine.

1.1.2. Various NDE techniques

The defects commonly introduced in material during manufacturing, processing and service operations are voids, cracks, delamination, and local weakness due to friction. Such flaws can be detected by adopting the appropriate NDE technique.

Visual inspection (VI) is used for detection of macroscopic defects such as surface breaks and poor welds, large cracks, dents, cavities, missing components, etc.[22]. Appropriate lighting, operator training and circumspection are important in determining the effectiveness of the VI technique.

Acoustic emission (AE) testing is a passive NDE technique which relies on detection of short bursts of acoustic signals emitted by an active crack under a load. This is a frequent method of NDE used for proof test of pressure vessels [23]. AE is also used for detection of leaks, noise from welding, rolling and machining during fabrication [24].

The liquid penetrant (LP) testing uses a low-viscous fluid that seeps into cracks in a non-porous material. The penetrant can be applied by dipping, brushing or spraying. Later, after removing excess penetrant, a developer is applied so that the penetrant liquid seeps upwards and a visual indication of an underlying flaw is created. The technique can be most efficiently used on structures with smooth surface finish so that excess fluid can be easily removed. Inspection is usually performed under white light or ultraviolet light based on the type of dye. Metals, glass, ceramics as well as plastic material are commonly inspected using LP test [25].

The magnetic particle inspection (MPI) uses magnetic fields to find flaws near surface of ferromagnetic material such as iron, cobalt or nickel [26]. The concept of MPI is that discontinuities on or near the surface of magnetic material tend to distort magnetic field, generating ‘leakage field’ which deviate beyond the specimen. Thus, the leakage of magnetic flux through magnetic particles coated on the surface of the specimen provides information about the defects near its surface.

In the radiography testing, high frequency gamma-rays or x-rays are used to examine a specimen. A radiographic image shows internal structure of specimen along with any variation in thickness or physical density arising due to defects or cracks. The resulting image can be obtained using radiographic film, computed tomography or radioscopy [27].

Thermal or infrared testing (IR) is another method that can be used as both active and passive NDE technique. In passive thermal testing, the wavelength of radiation emitted from the specimen is measured; temperature is calculated and/or presented as false color image showing variation of thermal radiation over the specimen. Such technique is used in detecting wearing out in bearings that overheat due to friction. However, in active thermography, temperature gradient is introduced through the specimen. Variation in inner features affect the surface temperature variations which are further analyzed to obtain information about flaws such as defects in bonding in composites [28].

Ultrasonic testing is a popular NDE technique in which high frequency sound waves are transmitted through the specimen. The results can be analyzed to detect discontinuities within the material based on the reflection or attenuated transmission of the ultrasonic waves. Ultrasonic tests can be used to detect micro-cracks and voids [29].

The electromagnetic or eddy current NDE technique is an active method that uses a time-varying magnetic field to induce eddy currents in a conducting specimen. A defect or discontinuity in the specimen disturbs the flow of these eddy currents and the changes in

the pattern of eddy currents can be recorded using a suitable sensor to analyze presence of flaws [30].

Based on the preconditions, one of these suitable NDE techniques is chosen to analyze and monitor the quality of material from time-to-time.

1.2. Different EM induction techniques

Electromagnetic geophysical methods not only find application in mineral exploration, but also in engineering and geotechnical applications, groundwater survey as well as to solve environmental issues. EM methods have the potential to support geophysical survey ranging from surface exploration to delineation of mantle boundaries. EM measurements can be performed at the surface, from an airborne setup, in the sea or inside boreholes.

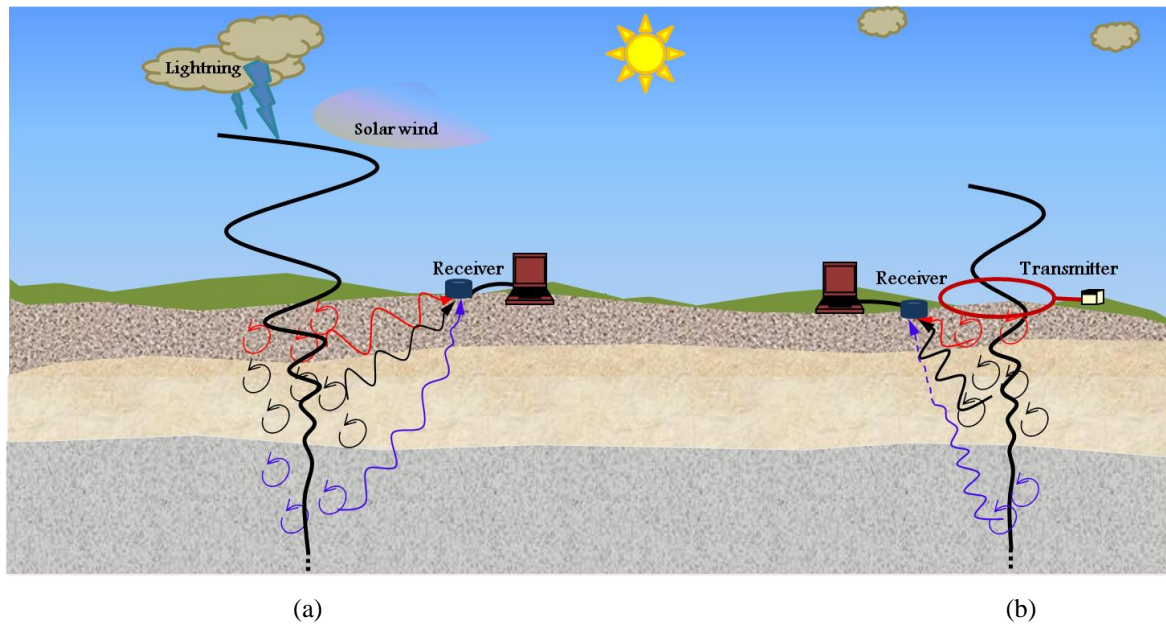


Fig 1.1 Illustration of (a) passive and (b) active electromagnetic geophysical exploration techniques.

The EM methods can be broadly classified into passive (for natural sources such as lightning and solar winds) and active (for controlled sources). An illustration of both techniques is presented in Fig 1.1. The idea of natural source EM technique known as magnetotellurics (MT) was conceived in the 1950s and has been extensively used since the 1960s [13]. In this technique, natural EM fields of the order of 1 mHz to 10 kHz are used

as source of excitation. Electrical storm or lightning results in EM fields between 1 Hz to 10 kHz while fields of frequency lower to 1 Hz originate from hydromagnetic waves within magnetosphere [31]. These primary excitations penetrating deeper layers of the earth produce eddy currents and the decay of these eddy currents and the associated magnetic field is recorded using suitable instruments. Owing to the broad range of frequencies of natural EM sources, the MT method is effective in shallow as well as deeper investigations ranging from few meters to even hundreds of kilometers [32].

In controlled source EM methods, an EM field is generated and transmitted into the nearby conducting bodies using a transmitter and the subsequent response of the conductor is recorded using a receiver. The controlled source EM method can be further categorized into Frequency Domain Electromagnetic (FDEM) and Time Domain Electromagnetic (TDEM) techniques. In FDEM, a sinusoidal current of fixed frequency is transmitted to produce a time varying magnetic field and the receiver records the variations in the voltage due to the induced eddy current or its associated magnetic field [33]. Along with geophysical survey, FDEM is also commonly used in non-destructive evaluation and testing to detect flaws in conducting objects.

The depth of investigation in FDEM technique is related to the diffusion as well as attenuation of EM waves in the medium [34]. The skin depth is an important parameter which gives the depth at which the EM wave is attenuated to $1/e$ times or 37% of its value at the surface. The skin depth is dependent on a number of factors such as electrical conductivity and magnetic permeability of the medium, and frequency of the propagating EM wave. For a given material of conductivity σ and permeability μ , the skin depth δ corresponding to an EM wave of frequency f is given by

$$\delta = 1/\sqrt{\pi\sigma\mu f} \quad (1.1)$$

For a particular target or subsurface, conductivity and permeability are fixed; skin depth varies inversely only with the frequency of transmission and hence, the depth of detection is limited by the frequency of excitation. Thus, using EM fields of single frequency, it is difficult to retrieve information about surface as well as deeper layers. Fig 1.2 shows an illustrative representation of eddy currents for low and high excitation frequencies in a conductive material.

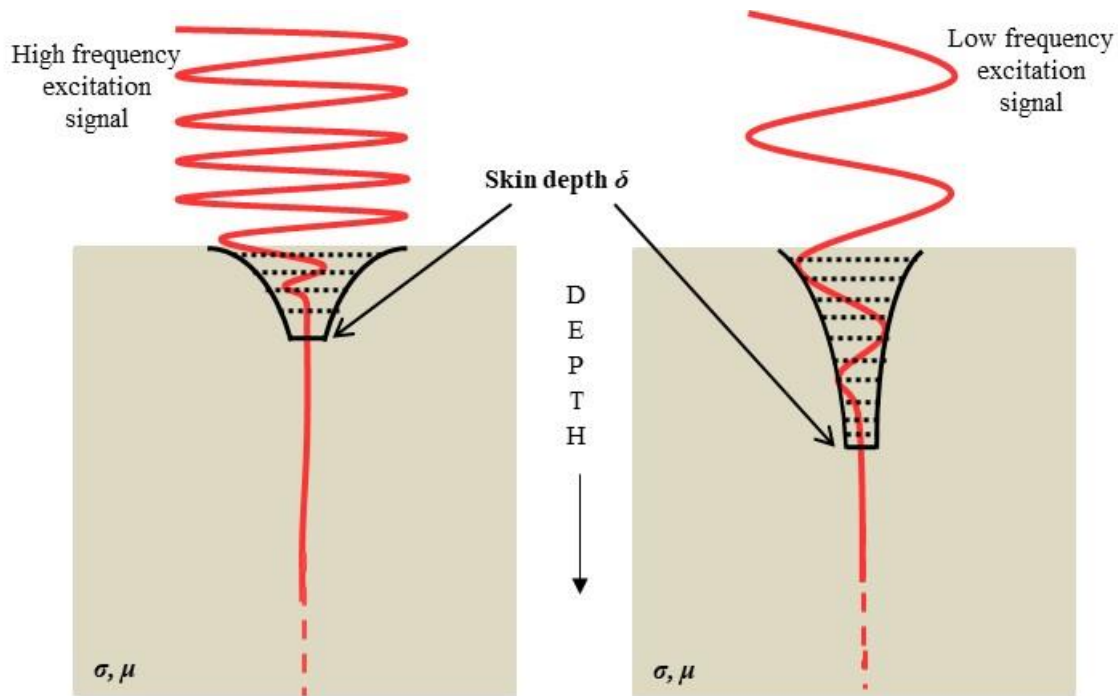


Fig 1.2 Illustrative representation showing different skin depth δ in two conductive objects with identical electrical conductivity σ and magnetic permeability μ with applied excitation signal of two different frequencies. The width of the dotted lines represents strength of the eddy current.

On the contrary, a pulsed electromagnetic excitation signal consist of a range of frequency components, thus a number of depths can be investigated during a single transmission. This reduces the time, effort and cost of geophysical surveys. Thus, the time domain electromagnetic (TDEM) or transient electromagnetic (TEM) method that uses pulsed excitations can be used to investigate different layers of the earth. The TDEM technique and its major applications are discussed in the following sections.

1.3. TDEM and its application

In TDEM technique, time varying electromagnetic field is generated using square wave pulses of current. The switching of these pulses induces eddy currents in the conducting targets, which can then be recorded using the receiver. In the TDEM technique, the diffusion depth, d , of a pulsed EM wave at a given time, t , in a conducting medium of conductivity σ and permeability μ is governed by

$$d = \sqrt{2t/\mu\sigma} \quad (1.2)$$

Being rich in various frequency components, a single excitation can provide necessary information corresponding to different depths. This method has also proven to be advantageous over the FDEM technique for non-destructive testing of metal objects [35]. Thus, the two major applications of TDEM, namely, geophysical survey and pulsed eddy current NDE are discussed briefly in the following sub-sections.

1.3.1. TDEM in geophysical survey

TDEM has been one of the most widely utilized techniques to obtain information on various layers of the earth by identifying contrast and variations in conductivity. This technique is popular in recent days in the field of oil and mineral exploration [36,37], ground water exploration [38], to locate salt and freshwater interface along the shoreline and to study seawater intrusion [39] etc.

The aim of all TDEM prospection is to derive the appropriate model of the earth using most accurate information from deeper layers. An optimal survey planning, experimental design, fast processing and modeling algorithms are necessary to efficiently obtain maximum information about the subsurface. A greater depth of investigation and high sensitivity to the subsurface response are of utmost importance in TDEM surveys. For a particular terrain, while depth of investigation can be improved by altering transmitter

parameters, the sensitivity can be enhanced by using wide-band and highly sensitive receivers.

Fig 1.3 shows a schematic illustration of the TDEM geophysical survey setup for delineation of buried conductive targets. Such TDEM measurements typically consist of a transmitter (Tx) coil to produce the primary magnetic field and a receiver (Rx) to measure the response of the subsurface layers to the applied magnetic field and a data acquisition system to store and interpret the acquired results. The depth of investigation depends on the transmitter moment and the terrain properties [20]. The transmitter moment M is given by

$$M = NIA \quad (1.3)$$

where N = number of turns, I = transmitter current and A = area of the transmitter loop. Increasing the area, or number of turns, or amplitude of transmitter current yields a higher depth of investigation.

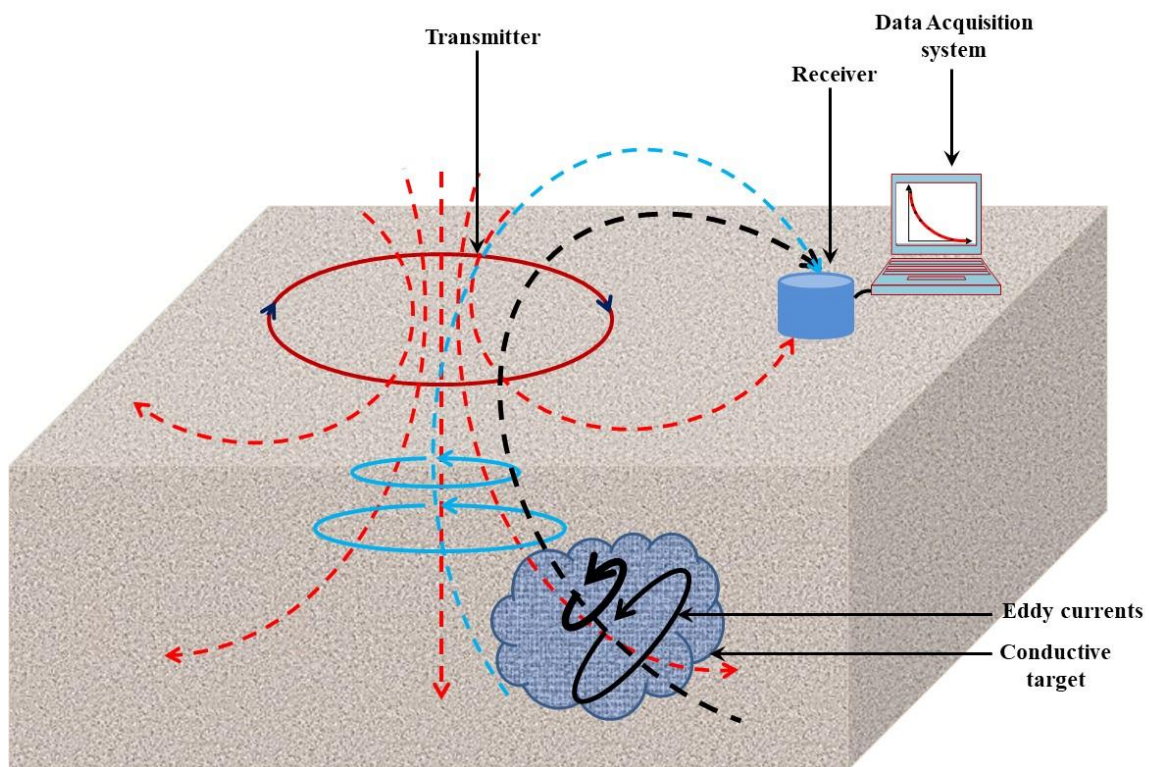


Fig 1.3 Geophysical exploration for buried conductive targets based on TDEM technique; the dashed red lines represent primary magnetic fields while the blue ones represent secondary magnetic fields.

Transmitter-Receiver Configurations: Optimum Tx-Rx configuration is specific to terrain and target properties. Generally, in large ground based TDEM surveys, a square transmitter loop is used. Depending on the specific application, the configuration and geometry of the Tx-Rx can vary. The process of recording the conductivity variation of the subsurface as a function of only depth at a single location is called sounding. A number of such soundings performed at different locations can be compiled together to obtain a spatial variation of conductivity and is known as profiling. Based on the requirement, the transmitter and receiver can be arranged in different forms and some of the common Tx-Rx configurations used in TDEM surveys are shown in Fig 1.4 [40].

In the single loop Tx-Rx system, a conducting loop is used as transmitter as long as current flows in the loop and the same loop serves as the receiver after the current is switched off (Fig 1.4 (a)). The loops are usually square in shape and vary from 5 m to 200 m in side length. The coincident loop system is also similar to the single loop system in geometry and the receiver is an induction coil in both cases (Fig 1.4 (b)). But in coincident loop configuration, both transmitter and receiver loops are laid out separately. The central

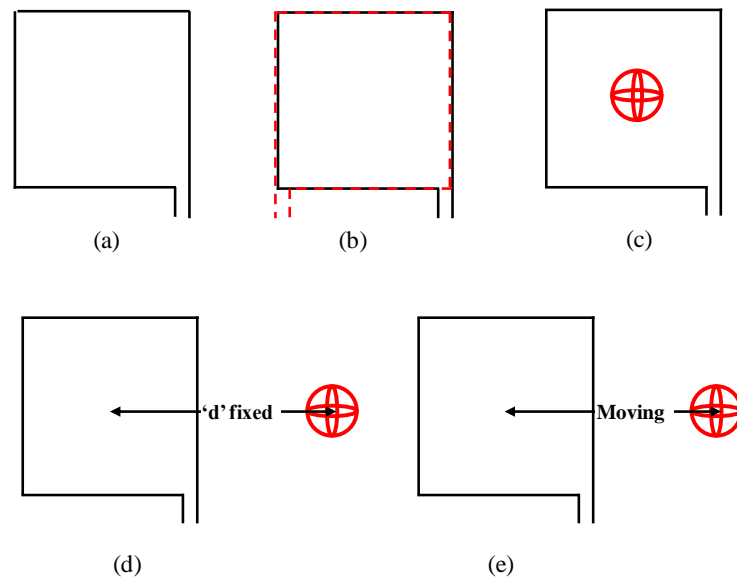


Fig 1.4 Different configuration of TDEM based geophysical survey setup: (a) single loop, (b) coincident loop, (c) in loop, (d) Slingram-type, (e) fixed loop and moving receiver; the transmitter is shown in black while the receiver is shown in red color.

loop or in-loop configuration uses a separate receiver placed at the center of the transmitter loop (Fig 1.4 (c)). The slingram-type configuration consists of the Tx and Rx separated by fixed distance (Fig 1.4 (d)). The size of the Tx is of the order of few tens of a meter. In order to profile a larger area to obtain spatial variations of conductivity, either the Rx can be moved with the Tx fixed (fixed loop), or both Tx and Rx can be moved together (moving loop) (Fig 1.4 (e)). While the single loop and coincident loop configurations can only use induction coils as receivers, the other configurations can use both coils as well as magnetic field sensors as receivers.

1.3.2. TDEM in NDE

The EM NDE exploits the principle of Faraday's law of electromagnetic induction. Fig 1.5 shows an illustration of the basic EM NDE setup. An excitation coil produces a time-varying magnetic field in order to induce eddy currents in a nearby conducting metal specimen. The growth and decay of this eddy current and its associated magnetic field deliver information about the conductivity of the specimen. More the conductivity of the metal, faster is the growth and slower the decay of the eddy currents. The presence of fault or crack acts like an insulating gap in an otherwise conducting material. The eddy current concentration near such flaws increases as they tend to take shorter path. A suitable sensor is used to record the variation in decay of eddy currents near defect from that of a defect-free portion of the specimen. In frequency domain eddy current NDE, both single frequency and multi-frequency techniques are used [41,42]. The single frequency eddy current NDE generally uses sinusoidal excitation. The strength of induced eddy current depends on amplitude and frequency of excitation current, geometry of excitation coil and sensor, and electrical and magnetic properties of the specimen [43–45]. The multi-frequency eddy current NDE technique is advantageous particularly, in cases where the flaws are located in material where the conductivity varies with geometry [46,47].

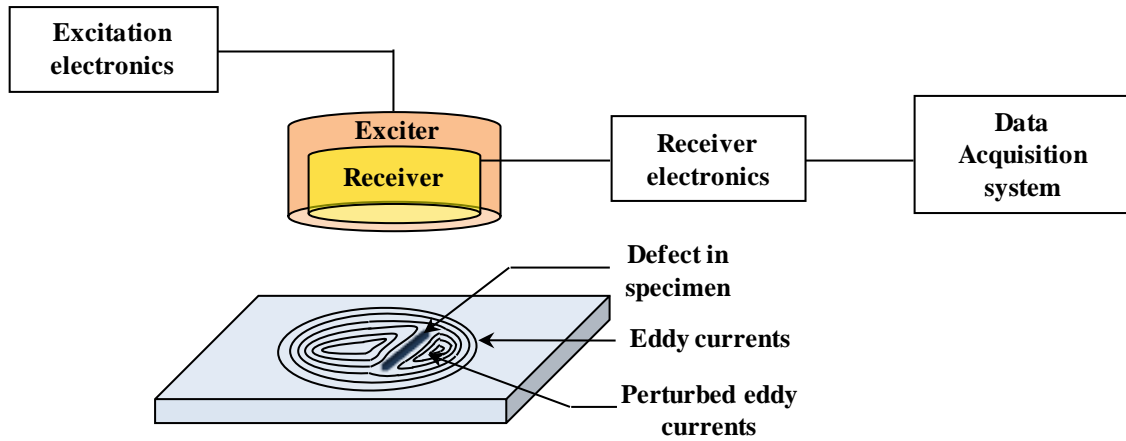


Fig 1.5 Illustration of electromagnetic induction based NDE setup

Since skin depth depends on the frequency of excitation, it is difficult to detect defects at different depths with single excitation frequency. This is particularly disadvantageous in case of thick conducting plates since a large number of scans with different frequencies have to be performed in order to determine the depth of the unknown defect. In such case, the TDEM or transient eddy current NDE is useful as different depths can be investigated with a single scan. Basically, a transient eddy current NDE system uses an excitation coil to transmit a pulsed current which generates a primary magnetic field in the conducting specimen. During the switch-on and switch-off of the pulse, eddy current is induced into the specimen. After the primary current has switched off or attained constant value, the eddy current and its associated secondary magnetic field decays. The rate of decay of these eddy currents and the associated magnetic field is recorded using a suitable sensor (coil or magnetic field sensor). The output signal is then processed to obtain the desired information. Studies on different excitation waveform have shown that the type of waveform does not have significant influence on the resolution of depth of defect and therefore square wave excitation signal is often preferred because of the ease of experimental realization [48]. Similarly, experiments with various pulse widths have also shown that the pulse-modulation eddy current technique (PMEC) is effective in detection

of subsurface corrosion [49,50]. In the following subsections, some of the commonly used excitation coil-receiver configurations, also known as probes, are discussed in brief.

Probes for transient eddy current NDE: A probe for transient eddy current NDE consists of an excitation coil and the sensor. The structure and type of both the excitation coil and the sensor depends on the application. Probes can be surface probe or pancake type (flat surfaces), encircling type (for rods and tubes) or internal coil (for tubes) [51]. Conventionally, in eddy current NDE systems for detection of defects, a reference signal is recorded by the probe at a place where there is no defect and later subtracted from the signal over the surface with an underlying defect in order to filter only the signal due to the defect. However, using a spatially differential probe instead of an absolute one provides the advantage of self-cancellation of field from areas without any defect. Thus, the need to record a reference signal can be avoided. Differential probes utilizing two sensors has been reported to show promising results for subsurface crack detection and characterization in stainless steel (SS) structures [52]. Similarly, differential probes have also been used for detecting cracks in aircraft structures [53]. A symmetric excitation coil generating linear eddy currents provides advantage of zero field in the absence of any defect or flaw [54]. Similarly, square or rectangular excitation coils induce non-circular eddy currents and the sensitivity is higher in particular direction which is beneficial in identifying shape of defect [55]. Probes with ferromagnetic cores and aluminum or iron shielding have also been used to concentrate magnetic flux and improve signal-to-noise ratio. Studies with such probe types like ferrite cored absolute probe and ferrite cored send-receive probe with and without outer shielding has been compared to obtain the most suitable probe for detection of defects in SS plates [56]. In case of inspection of ferromagnetic material, shielding the area between the excitation coil and the sensor with

iron has also been used to obtain higher sensitivity compared to unshielded probes or the ones with aluminum shielding [57].

As much as the configuration and geometry of the transmitter and receiver are important in determining the depth of investigation, the choice of a suitable receiver also plays an important role in obtaining sensitive information from deeper layers in both geophysical exploration as well as NDE applications. Various sensors used as receiver for transient electromagnetic measurements are discussed in the following section.

1.4. Sensors for TDEM applications

Although induction coils are always used for generating excitation signal, the response due to the eddy current from a conducting object can be recorded either in the form of secondary magnetic field using a magnetic field sensor (called magnetometer) or in the form of voltage induced into an induction coil due to the changing secondary magnetic field. Induction coil sensors measure the rate of change of eddy currents while magnetic field sensors or magnetometers directly measure the change in magnetic fields. Compared to magnetometers, induction coil sensors are simpler in design and operation. A major drawback of the induction coil sensor is that it is sensitive only to time-varying magnetic fields, while few magnetometers are sensitive to static magnetic fields as well. Detailed literature on various magnetic field sensors is available elsewhere [58].

When a circular transmitter coil of radius a carrying pulses of current of magnitude I is used to induce eddy currents in a conducting body with conductivity σ and permeability μ , the vertical component of secondary magnetic field recorded using a magnetometer and its time derivative recorded using an induction coil are respectively given by the following late time asymptotically approximate equations [59]

$$B_z = \frac{I\sigma^{3/2}\mu^{5/2}a^2}{30\pi^{1/2}}t^{-3/2} \quad (1.4)$$

$$V_z = \frac{-I\sigma^{3/2}\mu^{5/2}a^2}{20\pi^{1/2}}t^{-5/2} \quad (1.5)$$

where B_z and the induced voltage $V_z \propto \frac{\partial B_z}{\partial t}$ are respectively the vertical components of the secondary magnetic field and its time derivative recorded at time t . Since the voltage induced in the induction coil sensor decays as $t^{-5/2}$ while the magnetic field decays as $t^{-3/2}$, the voltage decays faster than the decay of the magnetic field itself. It is, therefore, obvious that the voltage measured by the induction coil reaches noise floor earlier than the magnetic field. Thus, using a magnetic field sensor or magnetometer to measure the magnetic field directly, higher sensitivity at greater depths can be achieved.

GMR (Giant Magneto-resistance), AMR (Anisotropic magnetoresistive) based magnetometer, Hall sensor, fluxgate and SQUID (Superconducting Quantum Interference Device) are some typical examples of magnetometers being used for NDE based defect detection [60–64] while magnetic field sensors such as SQUIDs and fluxgates are commonly used for TDEM based geophysical prospection [65,66]. The induction coil, fluxgate and SQUID sensors are discussed elaborately in the subsequent chapter.

1.5. Motivation and brief outline of thesis

1.5.1. Motivation

The objective of the thesis is the development of SQUID based TDEM system and its utilization in a terrain to probe the conductive target buried in deep layers of the earth covered by a thick and highly resistive layer. TDEM central loop sounding measurements have been carried out by using this system in the field, and the system performance has been compared with the central loop sounding measurements performed with an induction coil sensor and fluxgate magnetometer. Similarly, by using the same system, a novel transient eddy current NDE technique has been established for detection of defects in conducting materials by replacing the SQUID with fluxgate magnetometer.

Since the depth of investigation in TDEM central loop sounding measurements is proportional to transmitter moment and inversely proportional to the intrinsic noise of the receivers for a given transmitter moment, one can probe deeper layers of the earth using SQUID as compared to using conventional induction coil sensors. Similarly, while the depth of investigation is inversely proportional to the conductivity of the target with the use of an induction coil as the receiver, the same is independent of the nature of the target for the system with the use of magnetometer. Therefore one can probe the conducting target buried in deep layers of the earth by using sensitive magnetometer like SQUID. In addition to this, the voltage induced in the induction coil is proportional to the rate of change of the secondary magnetic field; this induced voltage decays faster than the decay of the secondary magnetic field itself. In contrast, the magnetic field sensor such as SQUID directly measures the magnetic field and hence it enhances the depth of investigation.

The SQUID based TDEM system comprises of the SQUID sensor and its associated fast readout electronics, transmitter, transmitter controller and a fast data acquisition system. The SQUID sensor has been mounted in a nonmetallic and non-magnetic probe, wired with suitable electronic connectors and characterized in a magnetically shielded room to evaluate its important characteristic parameters such as intrinsic noise, slew rate, bandwidth etc. In order to observe the performance of the system, the SQUID probe has been integrated with the other instruments and tested in a relatively noisy environment within the campus with the use of portable transmitter loop (2 m x 2 m) and a set of aluminum plates as targets. Meanwhile, in order to get a field survey experience, central loop sounding measurements were carried out in the test site (site located 350 km from our laboratory) using a fluxgate magnetometer as a receiver with the transmitter loop size of 100 m x 100 m and current of 25 A. In this survey, a strange behavior has been observed

pertaining to the use of fluxgate magnetometer in TDEM central loop sounding measurements; the decay of the secondary magnetic field measured using the fluxgate reaches negative values even at early decay times. Subsequently, detailed experiments have been carried out at our laboratory test site with fluxgate and SQUID magnetometers and compared. From the experimental results, we confirmed that the fluxgate magnetometer behaves like an induction coil at early times and magnetometer at later times.

Later, the TDEM central loop sounding measurements were carried out in the field using the SQUID system with the transmitter loop size of 100 m x 100 m and 400 m x 400 m with currents of 25 A and 27 A respectively. The same experiments were repeated with an induction coil, and fluxgate magnetometers as receivers and the acquired data were compared with data recorded using SQUID. The experimental results obtained with SQUID shows better target resolution as compared to the data obtained with an induction coil and fluxgate magnetometer. In addition to that, the data recorded with the fluxgate magnetometer provides further confirmation of the dual behavior of the fluxgate. Further simulation experiments have been carried out at laboratory level in order to prove the dual behavior of the fluxgate magnetometer in TDEM measurements.

Sub-surface defects and loss of thickness due to corrosion in conducting objects is detected using conventional eddy current NDE technique. In such case, eddy currents are induced at a fixed frequency, and changes of the secondary magnetic field due to the defect are measured in the frequency domain. At lower frequencies, the strength of the signal due to defects is low as the eddy current induced in the conducting object is quite small, while at higher frequencies the eddy current tends to be concentrated at the upper surface of the material owing to the skin effect, thus limiting the depth of detection. In contrast, transient eddy current NDE systems induce eddy currents in the form of pulses,

and the decay of secondary magnetic field is measured in the time domain. Since each pulse consists of a continuum of frequencies, one can simultaneously measure the defects near the surface as well as at depth with a single excitation. In conventional pulsed eddy current NDE, the features such as time to peak, zero cross over time, etc., provides information about the depth of the defect. But in the present transient eddy current NDE system, the feature "diffusion time", t_m directly provides information about the depth of the defect and therefore, has been evaluated for defects located at different depths from 2 mm to 20 mm below the surface of the plate. From this study, it was found that the maximum diffusion time, " t_m ", of the differential secondary magnetic field due to the presence of the defect directly correlates to the depth of the defect. It has been verified that the square root of the diffusion time t_m is proportional to the depth of the defect.

1.5.2. Outline of the thesis

Based on the work performed, the thesis is categorized into four major working chapters which are described briefly as follows:

Chapter 2 discusses the TDEM technique, instrumentation and data acquisition procedure in detail. The chapter also details the instruments developed and sensors used for the work. It also describes the characterization and tests of the TDEM system using the developed SQUID, induction coil and the commercial fluxgate magnetometer.

Chapter 3 describes the results of central loop TDEM field survey performed using the in-house developed SQUID system, induction coil sensor and the commercial fluxgate magnetometer. The chapter emphasizes the fact that detection of thin conducting target below thick resistive layers is a challenging task; however the choice of using a SQUID magnetometer over other sensors can enhance the efficiency of the TDEM system even with compact transmitters.

Chapter 4 deals with the application of fluxgate magnetometers for TDEM based geophysical survey. The results of the TDEM soundings show that the secondary magnetic fields recorded using fluxgate magnetometer attain negative values at earlier times while the data recorded using SQUID under same condition does not reach negative values. This chapter focuses on the experiments performed at the laboratory on fluxgate magnetometers and the results show that the fluxgate behaves like an induction coil at early stages of the decay while it behaves like a magnetometer in later stages of the decay.

Chapter 5 describes the development of a fluxgate based TDEM system using differential double “D” excitation coil for the detection of flaws in stacks of conductive aluminum plates at various depths ranging from 2 mm to 20 mm. The major outcome of this work is that time (t_m) at which the strength of the differential secondary magnetic field reaches maximum could be directly correlated to the depth of the defect.

Chapter 6 summarizes the conclusions and major findings obtained during the work done towards development and application of SQUID based TDEM system for geophysical applications.

Chapter 2

DEVELOPMENT OF SQUID BASED TDEM SYSTEM FOR GEOPHYSICAL APPLICATIONS

This chapter provides (1) introduction to TDEM system for geophysical applications; (2) working principle of TDEM; (3) detailed description and characterization of the sensors used in TDEM experiments (4) Integration and (5) performance testing of the system with the use of portable transmitter loop at laboratory level.

2.1. Introduction

The TDEM technique is an electromagnetic geophysical exploration technique that images the earth's response to the induced electromagnetic fields as a function of conductivity of the earth at subsurface depths. In conventional frequency domain electromagnetic (FDEM) technique, a time varying magnetic field with fixed frequency is applied to induce eddy currents in the ground and its response is sensed by using suitable sensor. The sensor output is phase sensitively detected with respect to the transmission frequency. In such frequency domain systems, the depth of investigation is limited by the use of single frequency and its associated skin depth. In contrast, time domain electromagnetic technique provides information about a range of depths with a single pulsed transmission since the pulsed current consists of a broad range of frequencies. Further, decay of the voltage induced in the induction coil sensor is faster than the decay of the secondary magnetic field itself. Magnetic field sensors such as SQUID measure the magnetic field directly, and therefore SQUID based TDEM systems have the potential to explore the conductivity of the earth at greater depths compared to what is possible with a conventional induction coil based TDEM system. For such a TDEM system, a SQUID probe has been developed, characterized, integrated with the other instruments and tested at laboratory level prior to implementation in field survey. In order to compare

performance of the SQUID based TDEM system, the SQUID sensor has been replaced by a home-built induction coil and a commercial fluxgate magnetometer.

2.2. Working principle of TDEM

The basic principle of TDEM technique is the induction of eddy currents in the ground and detection of subsequent decay of the eddy current using suitable sensor with time. The TDEM measurements are performed by passing current in the form of modified square waves through a large transmitter loop as shown in Fig 2.1 (a). The current in the transmitter loop is slowly raised to reach steady state resulting in static primary magnetic field. Subsequently, the current is rapidly switched off and the change of the primary magnetic field amplitude induces electromotive force (EMF) in the ground as shown in Fig 2.1 (b). The induced EMF drives electromagnetic eddy currents in the ground during the “Ramp Off” time. Then, the induced eddy current and its associated secondary magnetic field start decaying and the decay is measured as a function of time by using suitable receiver; either conventional induction coil or magnetometers such as fluxgate or SQUID. In general, most of the TDEM systems measure the net magnetic field (primary and secondary) as a function of time and the decay of the secondary magnetic field is extracted later for further processing. The net magnetic field measured by the induction coil and magnetometer have been schematically shown in Fig 2.1 (c) and Fig 2.1 (d) respectively. When the current in the transmitter loop is suddenly switched off, the induced eddy current in the ground just below the transmitter loop diffuses downwards and moves away from the transmitter [67]. Therefore, the eddy current induced near the surface decays earlier and the current that diffuses deeper into the ground decays at later times. Therefore, measuring the decay of the secondary magnetic field as a function of time gives information about the resistivity of the Earth as a function of depth [40].

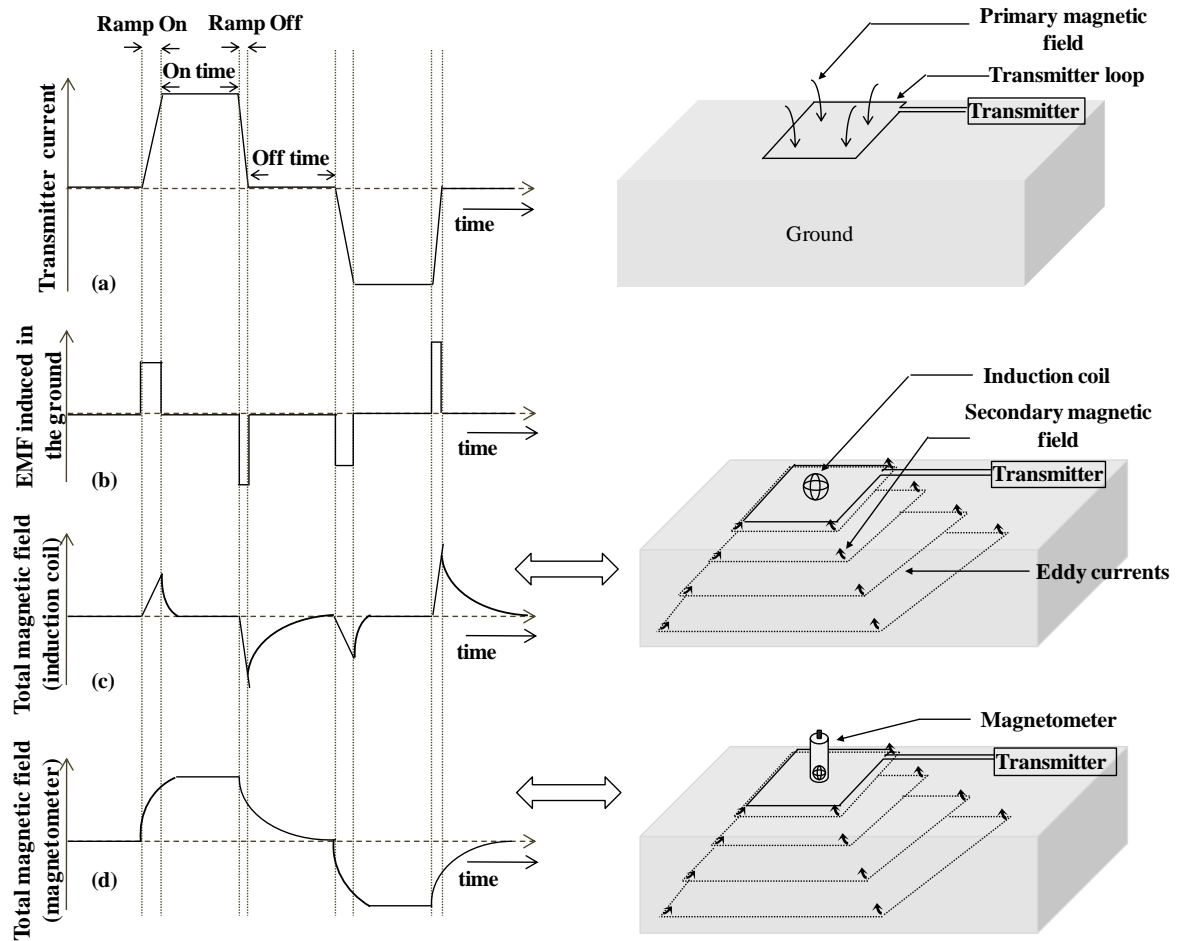


Fig 2.1 (a) Current in the transmitter loop or primary magnetic field produced by the transmitter loop, (b) electromotive force induced in the ground due to the changes of the primary magnetic field, and the net magnetic field measured by (c) an induction coil and (d) a magnetometer.

2.2.1. Data processing in TDEM measurements

The data processing of the TDEM measurements by using an induction coil as a receiver is shown in Fig 2.3. Since the net magnetic field (during “Ramp On”, “On time” and “Ramp Off” and “Off time”) is measured by the receiver, the decay of the secondary magnetic field only during “Off time” in the positive as well as negative half cycle is extracted by data processing because of the absence of the primary magnetic field. The electrical power line noise is eliminated by inverting the negative half cycle and averaging with positive half cycle (Fig 2.3 (b)). To suppress the electrical power line noise, the base frequency of the transmitter current is chosen in such a way that it is even fraction of the

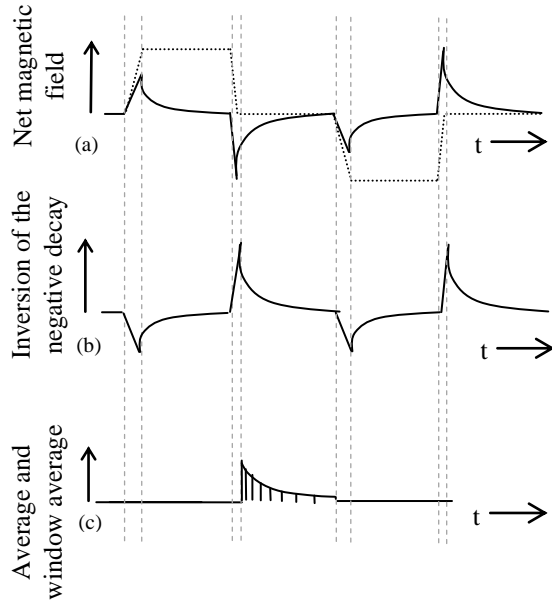


Fig 2.3 Data processing for the TDEM measurement with an induction coil. (a) Current in the transmitter loop (dotted line) and decay of the secondary magnetic field (b) Inversion of the negative decay of the secondary magnetic field (c) Averaging and window averaging of the decay of the secondary magnetic field.

due to poor signals strength as the sensitivity of the receiver reaches its limit. Therefore, the earlier time windows provide information about the decay of the eddy current near the Earth's surface whereas the later time windows provide information about the decay of eddy currents at greater depths. In the same way, the data processing of the TDEM measurements by using a magnetometer as a receiver is shown in Fig 2.2. Since magnetometers measure the

power line frequency (50 Hz / 60 Hz). In addition to this, to improve the signal to noise ratio data has been stacked over a long period of time. The stacked data is further averaged with time windows (time gates) in order to obtain better signal at late time windows. Since the strength of the decay of secondary magnetic field at earlier time is high, the size of the time window is kept shorter (Fig 2.3 (c)). Similarly, the size of the time window is kept longer at later times

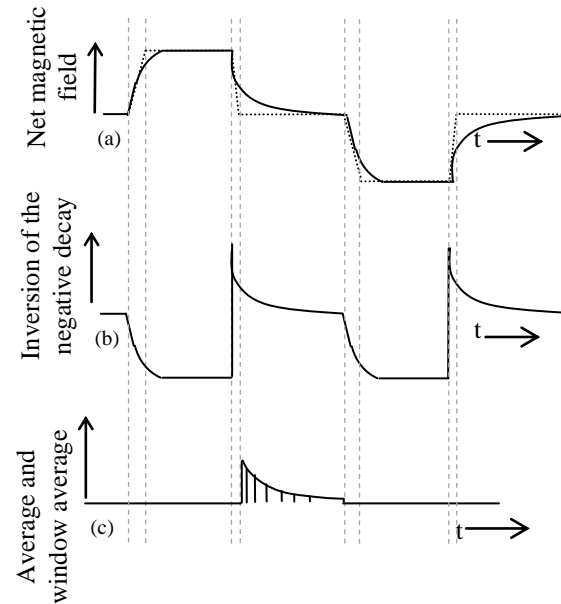


Fig 2.2 Data processing for the TDEM measurements with a magnetometer. (a). Current in the transmitter loop (dotted line) and decay of the secondary magnetic field (b) Inversion of the negative decay of the secondary magnetic field (c) Averaging and window averaging of the decay of the secondary magnetic field.

changes of the magnetic field directly (B_z field), the decay of the secondary magnetic field due to negative half cycle of the transmitter current is inverted and is averaged with first positive half cycle in order to remove the electrical power line noise .

2.2.2. General scheme used to eliminate power line noise

The general scheme used to eliminate power line noise has been briefly described with magnetic field data collected using fluxgate magnetometer. The raw data collected with number of stacks of 8 with base frequency of 2.5 Hz is shown in Fig 2.4 (a). Then, the positive and negative decay transients have been extracted and averaged (Fig 2.4 (b)).

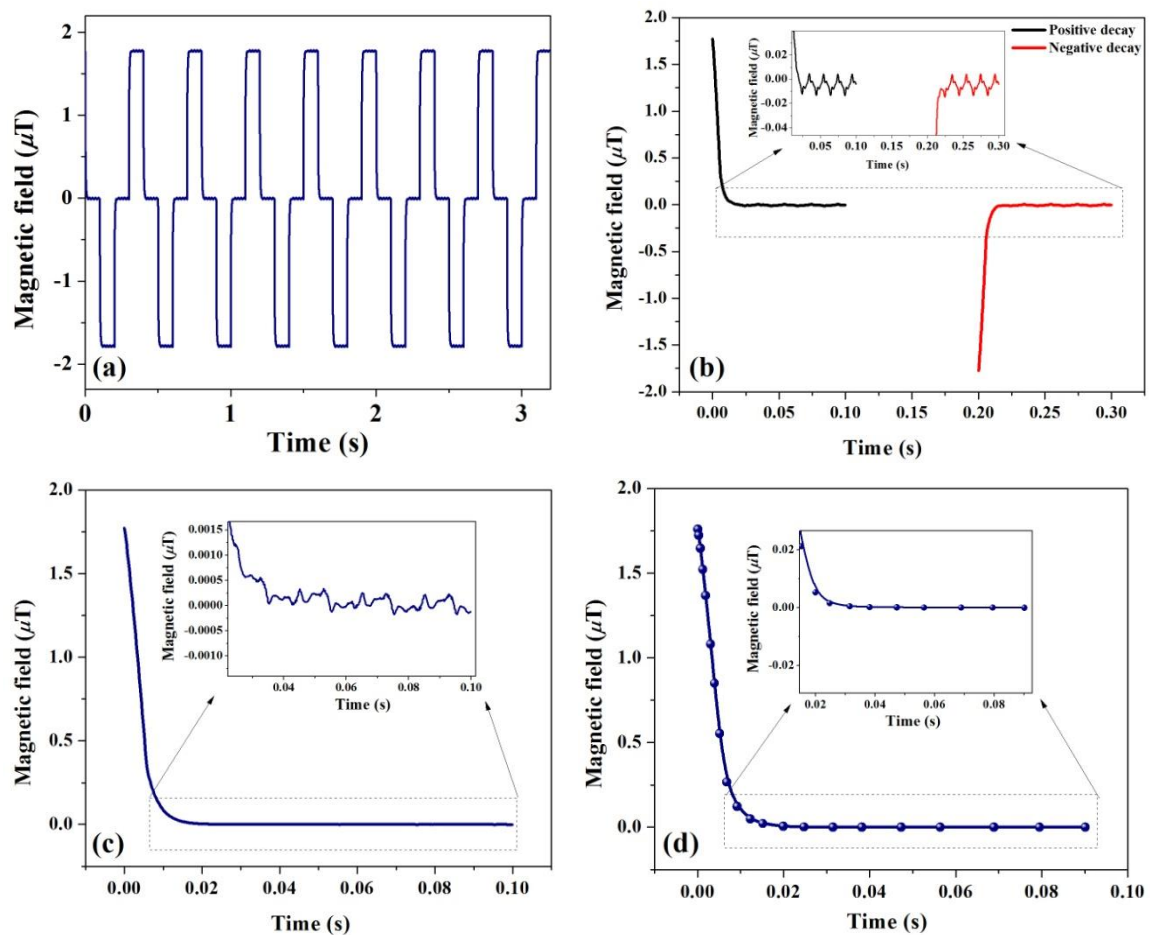


Fig 2.4 Example of data processing showing (a) raw data with 8 stacks, (b) Averaging of positive and negative transients (inset shows the presence of large power line noise), (c) inversion of negative transient and averaging with positive transient (inset shows the reduction of power line noise) and (d) final window averaged transient decay.

Further, the negative decay transient has been inverted and averaged with the positive decay transient (Fig 2.4 (c)). The inset in Fig 2.4 (b) shows the electrical power-line noise during the “Off time”. The inset in Fig 2.4 (c) shows the decay transient after minimizing the electrical power line noise. The data is again window-averaged over logarithmic time scales to display the final decay transient (Fig 2.4 (d)).

2.3. Sensors used in the work

In TDEM measurements, induction coil, fluxgate and SQUIDs are used to sense the decay of the secondary magnetic field. The drawback of using induction coil is that the voltage developed in the induction coil decays much faster than the decay of the secondary field itself and the induction coil reaches its noise floor much earlier [20]. Hence, it is difficult to probe deeply situated targets. Alternatively, magnetometers such as fluxgate and SQUID measure the decay of the secondary magnetic field directly and they give voltage output proportional to the B-field. Therefore, the use of B-field sensors in TDEM measurements provides better target resolution as well as larger depth of investigation. Since the present work is based on the development of SQUID based TDEM system for geophysical applications, an in-house developed induction coil and a commercial fluxgate magnetometer are also used in TDEM measurements in order to compare the performance of the SQUID system. The working principle of the above mentioned sensors, details of the in-house developed induction coil and the design of SQUID probe have been presented in the following sections.

2.3.1. Induction coil

Induction coil is the most commonly used sensor used not only in TDEM measurements but also for other time varying magnetic field [68–71]. The construction and working principle of the induction coil is relatively simple as compared to the other sensors that measure magnetic field such as SQUID and fluxgate [72]. The induction coil sensor works

based on the principle of Faraday's law of electromagnetic induction, that is, whenever a conductor experiences a changing magnetic field, an EMF is induced into it, which can be amplified using a suitable amplifier, and measured to get the rate of change of magnetic field. The output voltage V of the induction coil sensor is given by

$$V = - \left(\frac{d\Phi}{dt} \right) = -NA \left(\frac{dB}{dT} \right) = -\mu_0 NA \left(\frac{dH}{dT} \right) \quad (2.1)$$

where Φ is the magnetic flux passing through the coil with area A and number of turns N , μ_0 is the magnetic permeability of the coil core. Equation 2.1 implies that voltage developed in the induction coil is proportional to time rate of change of magnetic field H . From equation 2.1, it is clear that the sensitivity of the coil depends on number of turns and area of the induction coil. Thus, output voltage developed can be enhanced by increasing both. However, increasing the number of turns limits the bandwidth which may affect the detection of upper layers of the earth. Similarly, reducing the number of turns and area makes it difficult in detecting deeper layers of the earth due to its poor signal to noise ratio. Hence, there is a trade-off between sensitivity and bandwidth and it is difficult to optimize the induction coil for the use of TDEM measurements.

In order to compare performance of the SQUID based TDEM system with an induction coil based system, we designed and fabricated an induction coil along with a low noise amplifier. For this, a fiber reinforced plastic (FRP) former with a diameter of 270 mm and length of 50 mm was used. Copper wire with a gauge of 27, turns of 1300 has been wound over the former and its ends have been terminated by using suitable brass screws. The windings of the induction coil have been wrapped by few layers of aluminum foils and grounded in order to shield the high frequency electromagnetic interference. A low noise preamplifier with LT1028 with variable gain has been fabricated. In order to suppress the output oscillations of the induction coil, the input resistance of the preamplifier and

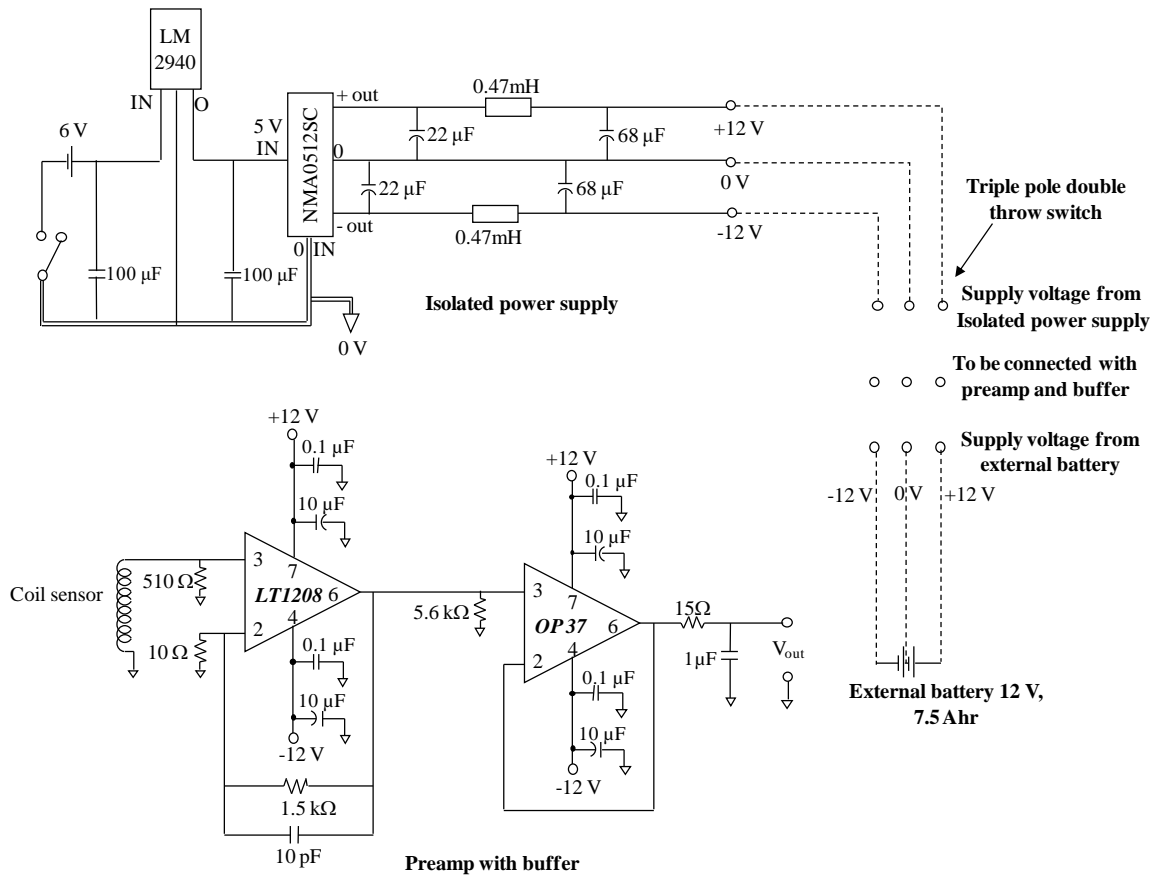


Fig 2.5 Circuit diagram of the amplifier designed for the induction coil

resistance of the induction coil have been matched. The detailed circuit diagram of the amplifier is shown in Fig 2.5 and photograph of the amplifier and induction coil is shown in Fig 2.6 (a) and (b) respectively. The induction coil has been calibrated by placing it in a known magnetic field. For this purpose, a square loop with a side length of 2 m and

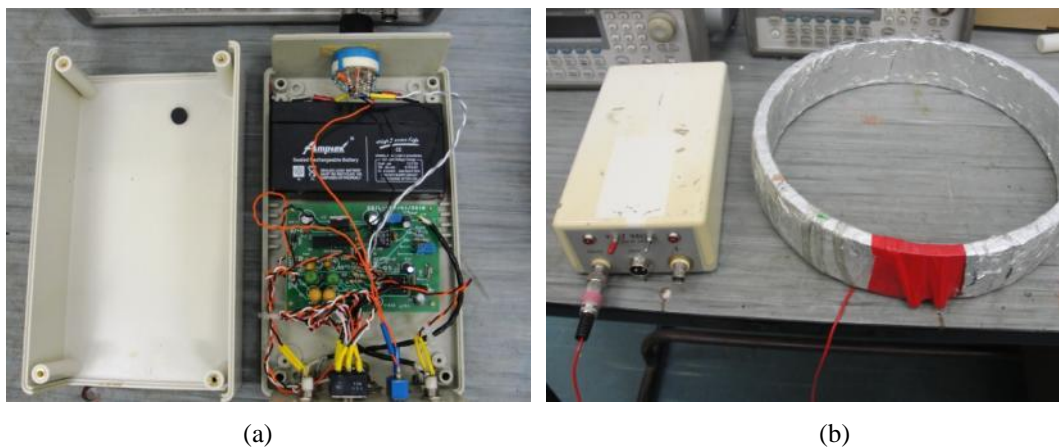


Fig 2.6 Photographs of the (a) amplifier and the (b) induction coil with amplifier.

with 10 turns was used to produce magnetic field using a sinusoidal current of frequency of 1 kHz.

The central magnetic field has been measured using the fluxgate sensor. From this, the coil constant of 10^{-5} Tesla/ Volt is obtained by assuming that the central field coupled to the induction coil is uniform. Further, the spectral density of the voltage noise has been measured by placing the induction coil at the center of a long μ -metal cylinder. Fig 2.7 (a) shows the noise measured in time domain and Fig 2.7 (b) shows the recorded spectral density of the voltage noise to be ~ 20 nV/ $\sqrt{\text{Hz}}$.

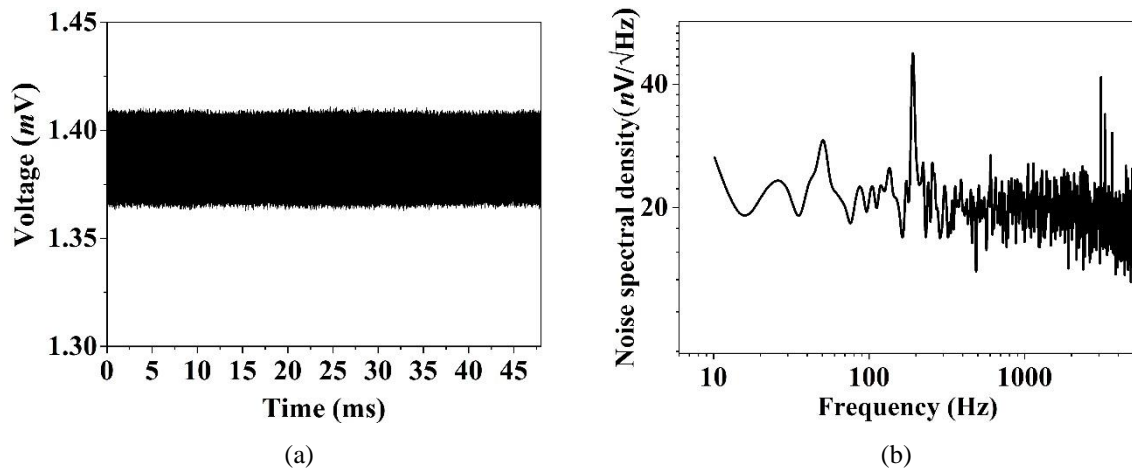


Fig 2.7 (a) Noise in time domain, (b) spectral density of the field noise measured by placing the induction coil at the center of the long μ -metal cylinder.

2.3.2. Fluxgate magnetometer

Fluxgate is a magnetometer, which originated somewhere in the 1940s to find and track submarines. Later, it came into use for airborne geophysical exploration of mineral resources [66,73]. The major advantages of using a fluxgate magnetometer are its ruggedness, reliability and stability [74]. The working principle of the fluxgate is described elaborately elsewhere [75].

The fluxgate magnetometer consists of a ferromagnetic core with high permeability, driving and pickup coils and a feedback coil. The commonly used ferromagnetic core is a

nickel-iron alloy known as permalloy. In general, the output voltage V recorded by the pickup coil is approximated as

$$V = -N \cdot A \cdot \left(\frac{dB_o}{dt} + K \cdot \mu_0 \mu_r \frac{dH_{ext}}{dt} + K \cdot \mu_0 \cdot H_{ext} \frac{d\mu_r}{dt} \right) \quad (2.2)$$

where N denotes number of turns of the pickup coil, A is the cross-sectional area of the core, B_o is the flux density in the ferromagnetic core due to the time varying applied magnetic field through a driving coil and H_{ext} is the externally applied magnetic field to be measured. Constants μ_o and μ_r are the permeability of free space and the core respectively, and K is a dimensionless coupling constant of the field H_{ext} to the core. Here, the first term can be nullified by using two cores instead of one. In such double core type fluxgate magnetometers, two identical ferromagnetic cores are used and the driving coil is wound on each with equal number of turns in such a way that the alternating magnetic field produced using the two driving coils is equal and opposite to each other, thus inducing zero net voltage to the pickup loop. The second term is the voltage induced in the pickup loop due to direct coupling of the time varying external magnetic field which can be eliminated by using a band pass filter with suitable bandwidth. The third term is the voltage induced in the pickup loop due to permeability modulation of the core and the voltage is subsequently processed through phase sensitive detection (PSD) and negative feedback.

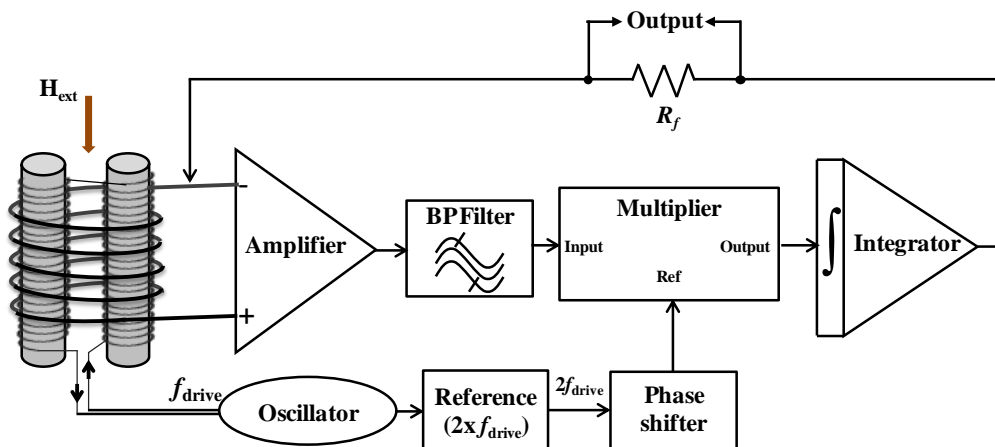


Fig 2.8 Block diagram of rod shaped double core fluxgate magnetometer with readout electronics.



Fig 2.9 Photograph of the Bartington's three-axis fluxgate magnetometer Mag-03MCL-100

The schematic diagram of the readout electronics with double rod core fluxgate is shown in Fig 2.8. Here, the core permeability is modulated by applying high frequency alternating magnetic field to the driving coil whose amplitude is just above the saturation of the core. The external magnetic field which is to be measured makes a shift in the B-H curve of the core and the corresponding voltage induced in the pickup loop will have a second harmonic of the driving frequency whose amplitude is proportional to the strength of the external magnetic field. The amplitude of the second harmonic signal is multiplied by the reference frequency which is twice the frequency of the driving frequency, integrated and fed back to the sensing coil to nullify the input field. Voltage developed at the output of integrator is proportional to the externally applied magnetic field.

A commercial tri-axial fluxgate magnetometer Mag-03MCL-100 from Bartington Instruments, UK has been used in this work and a photograph of the same is shown in Fig 2.9. The important specifications of the Mag-03MCL-100 magnetometer are given in Table 2.1. The intrinsic noise of the fluxgate magnetometer recorded in time domain and frequency domain in the magnetically shielded room (MSR) are shown in Fig 2.10 (a) and (b) respectively.

Table 2.1 Specifications of the Mag-03MCL-100 fluxgate magnetometer [Bartington Mag-03 datasheet].

| Specifications | Values |
|-----------------|--|
| Bandwidth | 3kHz |
| Noise floor | $< 6 \text{ pT}_{\text{rms}}/\sqrt{\text{Hz}}$ at 1 Hz |
| Measuring range | $\pm 100 \text{ } \mu\text{T}$ |
| Scaling | 100 mV/ μT |

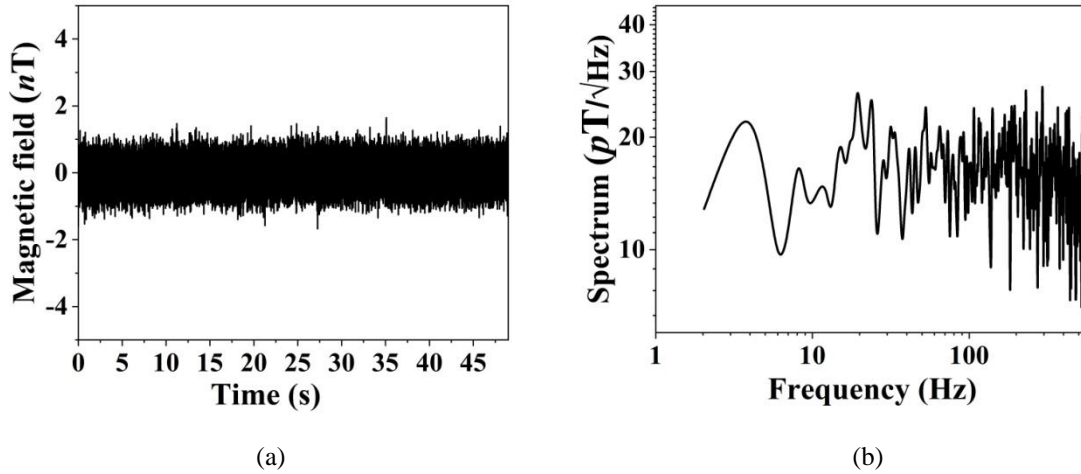


Fig 2.10 (a) Noise in time domain and (b) spectral density of the field noise of the fluxgate magnetometer measured inside the MSR.

2.3.3. SQUIDS

The SQUID sensor is basically a flux to voltage transducer with extremely high sensitivity (femtotesla) and wide operational bandwidth (DC to few GHz). The SQUID works based on the two fundamental physical phenomena, which are Josephson Effect and flux quantization. SQUID can measure any physical quantity that can be converted into magnetic flux for example, magnetic field, magnetic field gradient, magnetic susceptibility, current, voltage, pressure and mechanical displacement. SQUID produces measurable output voltage for tiny changes of input magnetic field which cannot be measured by any other sensor available in the world. SQUID produces periodic output voltage for linearly varying input flux with periodicity of one flux quantum Φ_0 ($\Phi_0 = h/2e = 2.068 \times 10^{-15}$ Wb). Since the output voltage of the SQUID is periodic, it is necessary to linearize the SQUID output to use in applications. This periodic output voltage of the SQUID could be linearized by using Flux locked Loop (FLL) readout electronics [76,77]. By using the SQUID sensor and its associated readout electronics, one can measure the changes of applied magnetic flux much less than one flux quantum. The working of the SQUID sensor along with the process of linearization is explained henceforth.

Whenever two superconductors are separated by a thin insulator, the Cooper pairs are able to tunnel across the barrier without dropping any voltage. The magnitude of the current flow across the Josephson junction depends on the phase difference between the two superconductors.

$$I = I_0 \sin \delta\varphi \quad (2.3)$$

where I_0 is the maximum current that the junction can sustain without developing any voltage and is also known as the critical current of the Josephson junction, and $\delta\varphi$ is the phase difference between the two weakly coupled superconductors.

According to the principle of flux quantization, total flux threaded into the superconducting loop is always integral multiple of flux quantum. Whenever any external magnetic flux (Φ_{ext}) is applied to a superconducting loop, a screening current J is induced in the loop in order to satisfy the relation

$$\Phi_{tot} = \Phi_{ext} + LJ = n\Phi_0 \quad (2.4)$$

where, L is the self-inductance of the superconducting loop and n is an integer.

The configuration of the SQUID is given in Fig 2.11 (a). The SQUID consists of a superconducting ring which is interrupted by two identical Josephson junctions. To describe the operation of the DC SQUID, let us assume that the bias current I_b is swept from zero to a value above the critical current ($2I_0$) of the two junctions with a fixed frequency. A slowly varying magnetic flux is applied perpendicular to plane of the loop and the frequency associated with the variations in magnetic flux is much lower than the frequency associated with the Josephson oscillations. When the applied magnetic flux Φ_{ext} is zero (or $\Phi_{ext} = n\Phi_0$), no screening current circulates around the loop and the bias current I_b simply divides equally between the two junctions, assuming a symmetric SQUID. When a small magnetic flux Φ is applied, the requirement of quantization of magnetic flux generates a screening current $J = -\Phi/L_s$, where L_s is the inductance of the SQUID loop.

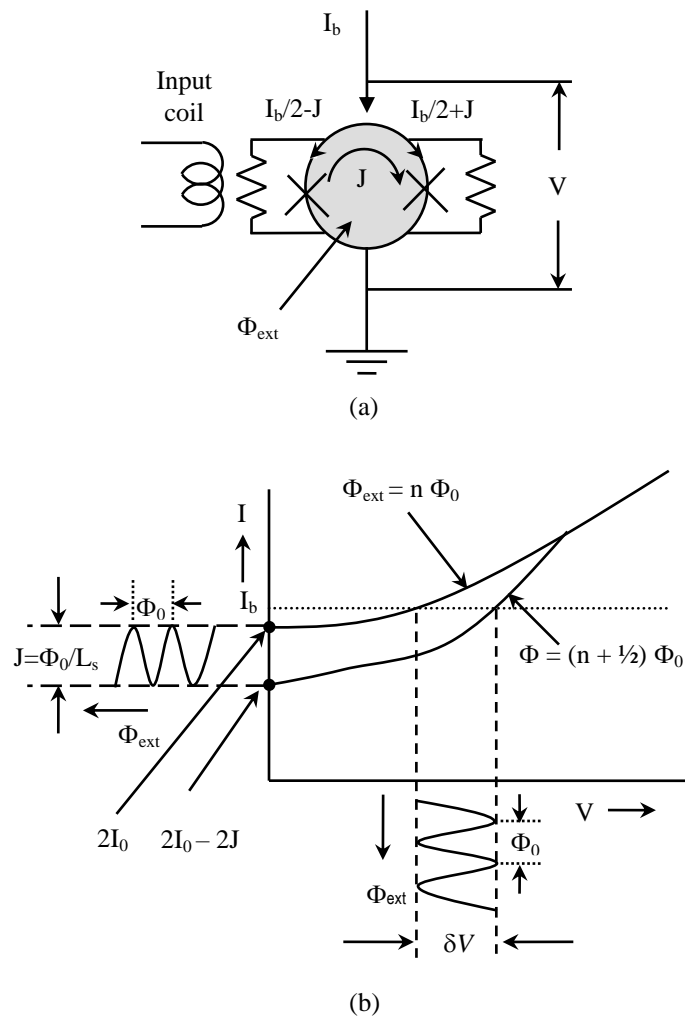


Fig 2.11 (a) Schematic configuration of the DC SQUID and (b) I-V characteristics of the DC SQUID when the external magnetic flux coupled to the SQUID.

The screening current induced in the SQUID loop adds to the bias current flowing through junction 1 and subtracts from that flowing through junction 2. When junction 1 reaches its critical current $I_0 = I_b/2 + J$, the current flowing through the junction 2 is $I_0 - 2J$ and the total current flowing through the SQUID is $2I_0 - 2J$. Hence, when the magnetic flux is applied, SQUID switches to a finite voltage state when the total current flowing through the SQUID is $2I_0 - 2J$ instead of $2I_0$. When the applied flux is increased to $\Phi_0/2$, the screening current J reaches a value of $\Phi_0/2L_s$ and the critical current falls to $2I_0 - \Phi_0/L_s$ as shown in Fig 2.11. When the flux Φ is increased further, the SQUID makes a transition from the flux state $n = 0$ to $n = 1$, J changes its sign and eventually reaches zero when the applied

flux equals Φ_0 . At this point, the critical current of the SQUID is restored to its maximum value of $2I_0$. In this way, the critical current oscillates as a function of applied magnetic flux. If we bias the SQUID with a direct current greater than the critical current of the two Josephson junctions, the voltage developed across the SQUID oscillates with a period Φ_0 for the steadily increasing input magnetic flux. Thus, the SQUID produces output voltage in response to a small input flux $\delta\Phi$ ($\ll\Phi_0$), and is effectively a flux to voltage transducer. The voltage swing δV produced at the output of the SQUID is known as the modulation depth of the SQUID when the applied magnetic flux is changed from 0 to $\Phi_0/2$. The modulation depth of the typical low T_c DC SQUID is ~ 20 to $30 \mu V$. The usable voltage swing δV is optimum for bias currents just above the maximum critical current of the SQUID.

Since the output voltage of the SQUID is a periodic function of the input signal flux, it is necessary to linearize it for use in practical applications. It is also possible to operate the SQUID in small signal mode over a small range of flux around the optimum working point W , which is located near the steepest part of the V - Φ characteristic. However, in most cases, the signal flux to be measured exceeds $\Phi_0/2$ and it may even be many hundreds of flux quanta. In order to keep the non-linearity low and to avoid excess noise at large excursions from the optimum working point, the signal flux has to be kept well below the linearity limits of $\pm\Phi_{lin}/2$. Therefore, the SQUID is operated in a feedback loop as a null detector of magnetic flux and the voltage at the output of FLL is proportional to the input signal flux.

Our group had a program on development of SQUID sensors and its associated FLL (Flux Locked Loop) readout electronics and utilization of these sensors to build high field SQUID magnetometer for magnetization measurement of weak magnetic materials [78] and SQUID based non-destructive evaluation system for engineering applications [79,80].

Our SQUID design is a conventional Ketchen-Jaycox single slit washer geometry (inner hole size of $100\ \mu\text{m} \times 100\ \mu\text{m}$) whose loop inductance (L_s) is large and the effective flux capturing area (A_{eff}) is small. Hence, there is a trade-off between the effective flux capturing area and sensitivity. Since the sensitivity of the SQUID depends on the SQUID loop inductance, it is necessary to mount the SQUID sensor inside the superconducting cylinders in order to shield from external magnetic noise. Similarly, the effective area of the SQUID could be enhanced by connecting an external superconducting pickup loop in the form of either first order or second order gradiometer to the on-chip integrated multi-turn input coil which is built-in over the SQUID loop [81]. This is because the signal source to be measured in most of the SQUID based measurement systems (bio-magnetism, SQUID magnetometer, SQUID based NDT system, SQUID NMR, etc.) are localized except in TDEM applications. In TDEM measurements the signal (decay of the secondary magnetic field) comes from deeper layers of the earth, so gradiometers are not suitable. In addition to this, the flux to voltage transfer coefficient, $(\partial V / \partial \Phi)_b$ of the single slit washer SQUID is small, high frequency (typical modulation frequency 100 kHz to 500 kHz) flux modulation and subsequent phase sensitive detection will be required to enhance the signal to noise ratio of the SQUID in the feedback [82].

For the sake of completeness, the schematic diagram of the readout electronics operated with flux modulation scheme is shown in Fig 2.12. The SQUID is biased with an optimum DC bias current (I_b) to obtain maximum voltage modulation. The magnetic flux, which is to be measured (in actual field measurement applications), is applied to the input coil of the SQUID. This flux is inductively coupled to the SQUID loop via the mutual inductance M_i , between the SQUID loop and the input coil. The signal flux is modulated by a sinusoidal flux ($\sim 100\ \text{kHz}$) whose peak-to-peak amplitude is less than or equal to $\Phi_0/2$. This modulated output voltage is stepped up by an impedance matching transformer and is

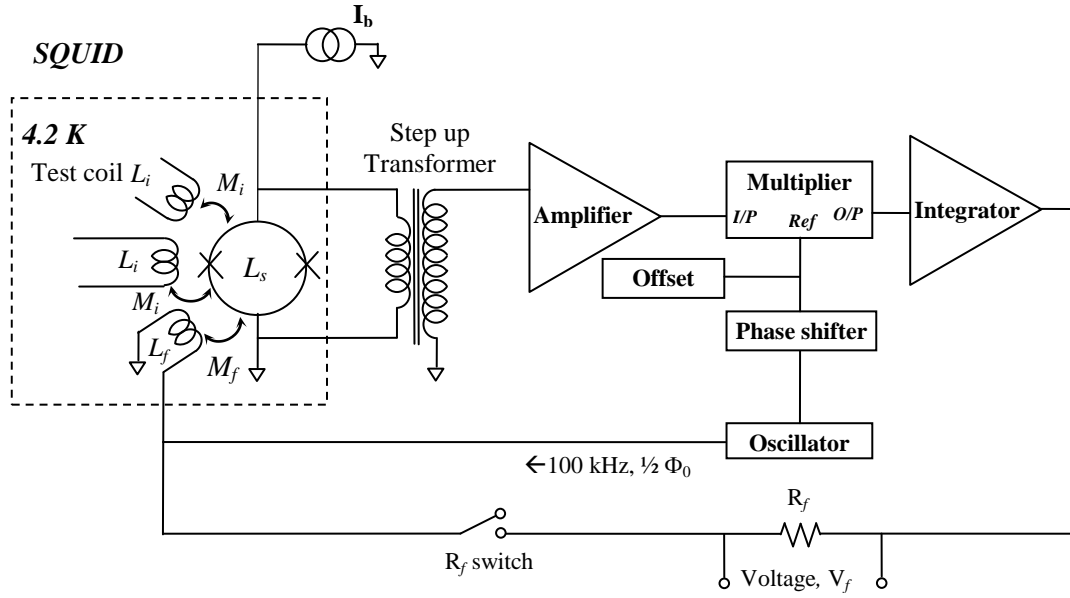


Fig 2.12 Schematic diagram of the flux readout electronics operated with flux modulation scheme.

further amplified by another two stage amplifier with sufficient gain; it is then fed to the input channel of the analog multiplier; the phase of the reference signal is adjusted to maximize the output of the multiplier. The modulated output is phase sensitively detected with respect to reference signal supplied from the same 100 kHz oscillator to the reference input channel of the analog multiplier. The output of the analog multiplier is integrated and fed back as a current through the feedback coil in order to counterbalance the signal flux applied to the SQUID. The voltage, V_f developed across the feedback resistor R_f is proportional to the input flux and the transfer function of the system ($\partial V_{FLL} / \partial \Phi_{sig}$) is given by R_f and M_f , where R_f is the feedback resistance and M_f is the mutual inductance between the feedback coil and SQUID. The bandwidth and slew rate (Φ_0/s) of the FLL readout system are substantially low for the conventional SQUID with the use of flux modulation scheme. The bandwidth and slew rate are important parameters for the use of SQUIDS in TDEM measurements.

2.3.4. SQUIDS with Additional Positive Feedback (APF)

In view of above facts, SQUID sensors with associated fast FLL readout electronics were

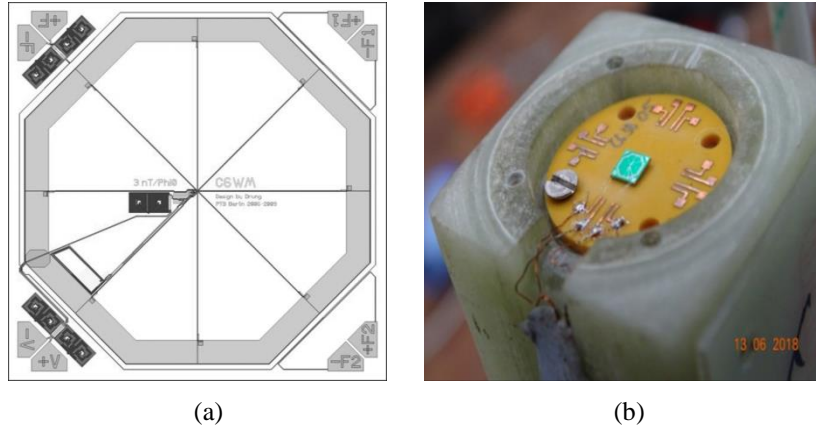


Fig 2.13 (a) Schematic view and (b) photograph of the Magnicon multi-loop SQUID.

procured from Magnicon, Germany (Fig 2.13). Here, the SQUID loops (typically 8 or 16) are connected in parallel in order to reduce the total SQUID loop inductance and increase the effective flux capturing area [83]. In addition to this, an additional positive feedback technique has been used to enhance the flux to voltage transfer coefficient $(\partial V / \partial \Phi)_{I_b}$ at the working point, W and to increase the signal-to-noise ratio of the SQUID output. For this, part of the SQUID output is coupled to the SQUID by connecting optimum shunt resistance (R_{APF}) and inductor (L_{APF}) as shown in Fig 2.14. Since the flux to voltage transfer coefficient of the SQUID is large, direct readout electronics is used to linearize the periodic output voltage of the SQUID. Therefore, the bandwidth and slew rate of the FLL readout electronics is sufficiently large enough to use these sensors in TDEM system for geophysical applications. When the transmitter current is suddenly switched off, the SQUID system should track the changes of the magnetic field (transients consist of continuum of frequencies) without losing lock. The switch off time of the transmitter loop depends on the loop inductance (L) and resistance (R) in addition to the nature of the terrain. In case the terrain is highly resistive, the decay of the magnetic field is abrupt and SQUID system with high slew rate is mandatory. For example, let a square transmitter loop of side length of 100 m carrying a current of 20 A produces magnetic field of 226 nT at the center which is equivalent to 75 Φ_0 for the SQUID with the inverse effective

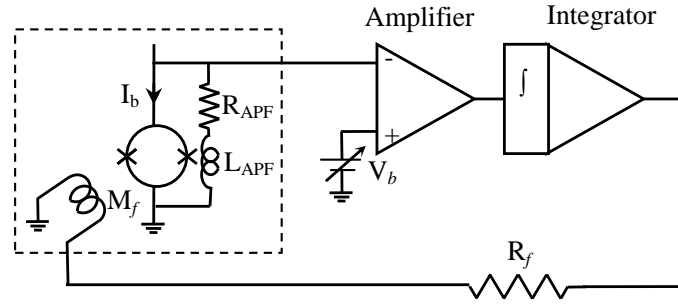


Fig 2.14 Schematic view of the direct readout electronics of the SQUID with APF

area of $3 \text{ nT}/\Phi_0$. For the typical values of switch off time between 100 to 200 μs , the required slew rate of the FLL is $3.75 \times 10^5 \Phi_0/\text{sec}$ to $7.5 \times 10^5 \Phi_0/\text{sec}$. In addition, SQUID system with high slew rate provides stable operation during transient measurements (refer Fig 2.15).

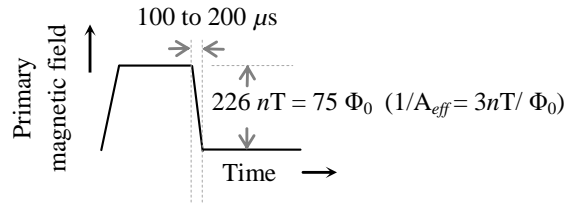


Fig 2.15 Typical transmitter waveform with half period for a transmitter loop size of 100 m x 100 m and with transmitter current of 20 A.

An FRP holder has been fabricated to mount three SQUID sensors in order to make three axis SQUID probe and necessary electrical wiring has been done carefully for biasing leads, the voltage output leads and the feedback leads as instructed by Magnicon [84]. The SQUID probe has been mounted in an FRP liquid helium cryostat to see the performance in the shielded environment. The liquid helium capacity of the cryostat is about 14 liters and its holding time is around 4 to 5 days. Few layers of aluminum foils have been wrapped around the cryostat in order to shield the high frequency electro-magnetic interference. The $V-\Phi$ curve has been displayed in the oscilloscope by passing a current equivalent to one flux quantum through input coil and the optimum bias current, I_b has been adjusted to get maximum output (upper trace in Fig 2.16 (a)). Bias voltage, V_b

has been adjusted to set the working point W, where the flux to voltage transfer coefficient $(\partial V/\partial \Phi)_{I_b}$ is maximum (middle trace in Fig 2.16 (a)). Similarly, bias flux, Φ_b has been adjusted in order to get zero output voltage after locking the SQUID (lower trace in Fig 2.16 (a)). Maximum slew rate of $10^6 \Phi_0/s$ has been obtained in this system by passing current with high frequency through an external coil (coil wrapped around the cryostat at the bottom). Similarly, the spectral density of the field noise has been evaluated by using the inverse effective area of the SQUID, that is $3 \text{ nT}/\Phi_0$ which was calibrated and given by the supplier. The spectral density of the field noise of $25 \text{ fT}/\sqrt{\text{Hz}}$ in the white noise regime has been obtained by operating the FLL with gain of $175 \text{ mV}/\Phi_0$ ($R_f = 10 \text{ k}\Omega$ and

$(I/M_f) = 17.5 \text{ }\mu\text{A}/\Phi_0$) (Fig 2.17)). The noise recorded at the output of the SQUID in time domain inside MSR is shown in Fig 2.17 (a) and the corresponding spectral density of field noise is shown in Fig 2.17 (b).

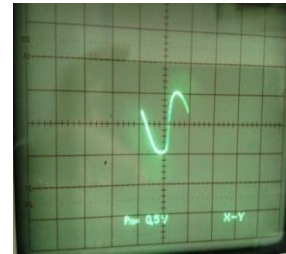
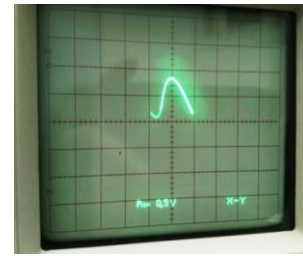
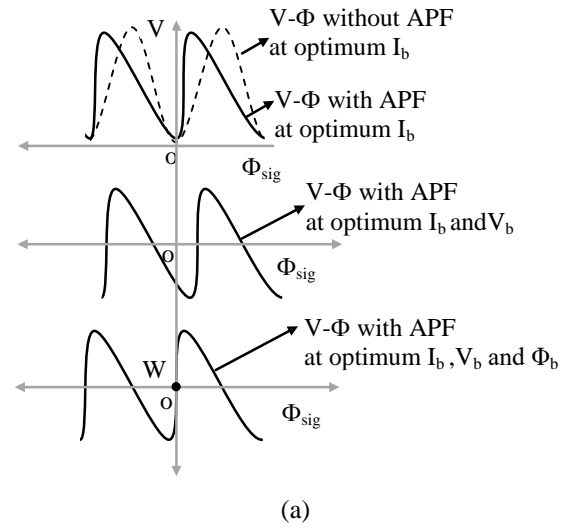


Fig 2.16 (a) Typical output of the multi-loop SQUID optimum bias current I_b , bias voltage V_b and bias flux Φ_b (b) V- Φ curve of the SQUID for the input flux of one flux quantum without optimum and with optimum values I_b , V_b and Φ_b .

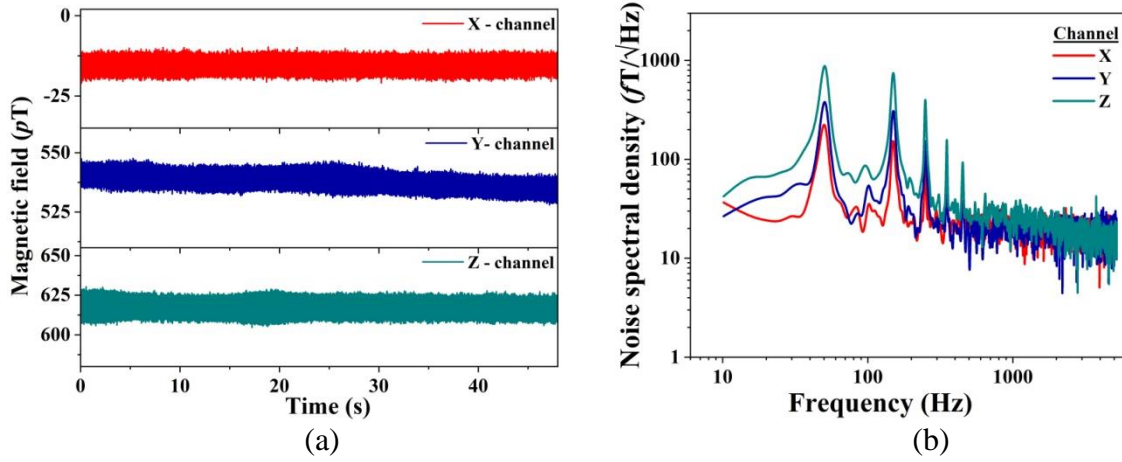


Fig 2.17 (a) Noise recorded in time domain and (b) spectral density of the field noise of the SQUID magnetometer measured inside the MSR

2.4. Integration and performance testing of TDEM system with portable transmitter loop

The SQUID based TDEM system for the use of geophysical application has been developed by integrating the SQUID system as a receiver with the other electronic instruments. The TDEM system comprises of a transmitter (ZT-30 from Zonge International [85]) to drive a current in the form of trapezoidal pulses through the transmitter loop with the help of external batteries, transmitter controller (SMARTem24 from EMIT [86]) to set and control the waveform parameters of the transmitter, transmitter loop (size and shape as desired by the user) and fast data acquisition system (SMARTem24 from EMIT [86]) to record the response of the sensor (induction coil or magnetometer). The data acquisition system can display the recorded data in the form of raw, stacked, decay transients and station profile using built-in software and store it for further processing. The system has been tested at the laboratory level by fabricating a transmitter loop in the form of square with one turn and side length of 2 m. The transmitter loop is placed at a height of about 0.5 m from the earth surface by suitable non-metallic and non-magnetic supports. Since the transmitter is placed far away from the data acquisition system, direct time synchronization is difficult in field survey with larger

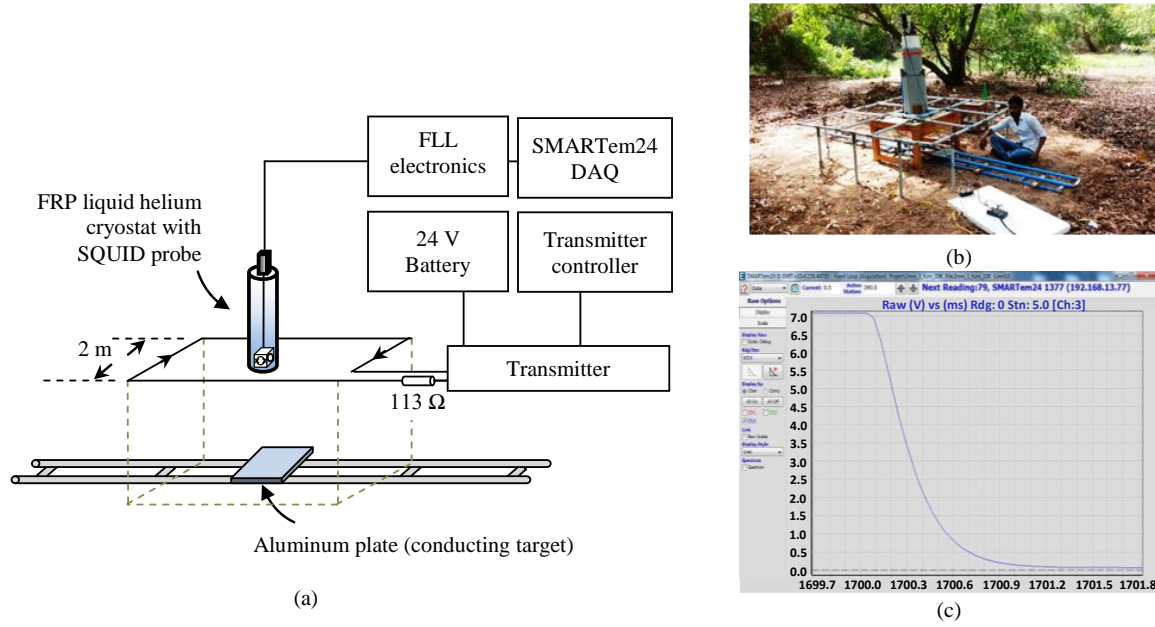


Fig 2.18 (a) Schematic view of the SQUID based TDEM setup with transmitter loop of 2 m x 2 m, (b) Photograph of the FRP liquid helium cryostat with SQUID probe and transmitter loop and (c) Output of the SQUID when the current (equivalent to $40 \Phi_0$) passing through the transmitter is suddenly switched off.

transmitter loops. Therefore, time synchronization has been done between the transmitter controller and data acquisition system before the survey. Then the transmitter is connected to the transmitter controller which controls the base frequency and duty cycle of the current pulses generated by the transmitter. In this case 24 V, 150 Ahr batteries are used to power the transmitter loop which, in turn, supplies current in the form of square pulses at a repetition rate of 400 ms (base frequency of 2.5 Hz). Current of 0.212 A (120 nT at the center so that $40 \Phi_0$ is coupled during switch-off) is transmitted through the transmitter loop using series resistance of 113 ohms. The sensor is placed at the center of the transmitter loop and in the same plane with the transmitter loop. The schematic view of the experimental setup, photograph of the SQUID based TDEM system with portable transmitter loop and output of the SQUID recorded by the SMARTem24 data acquisition system when the current (equivalent to $40 \Phi_0$) passed through the transmitter is suddenly switched off are shown in Fig 2.18 (a), (b) and (c) respectively. The screen shots from the

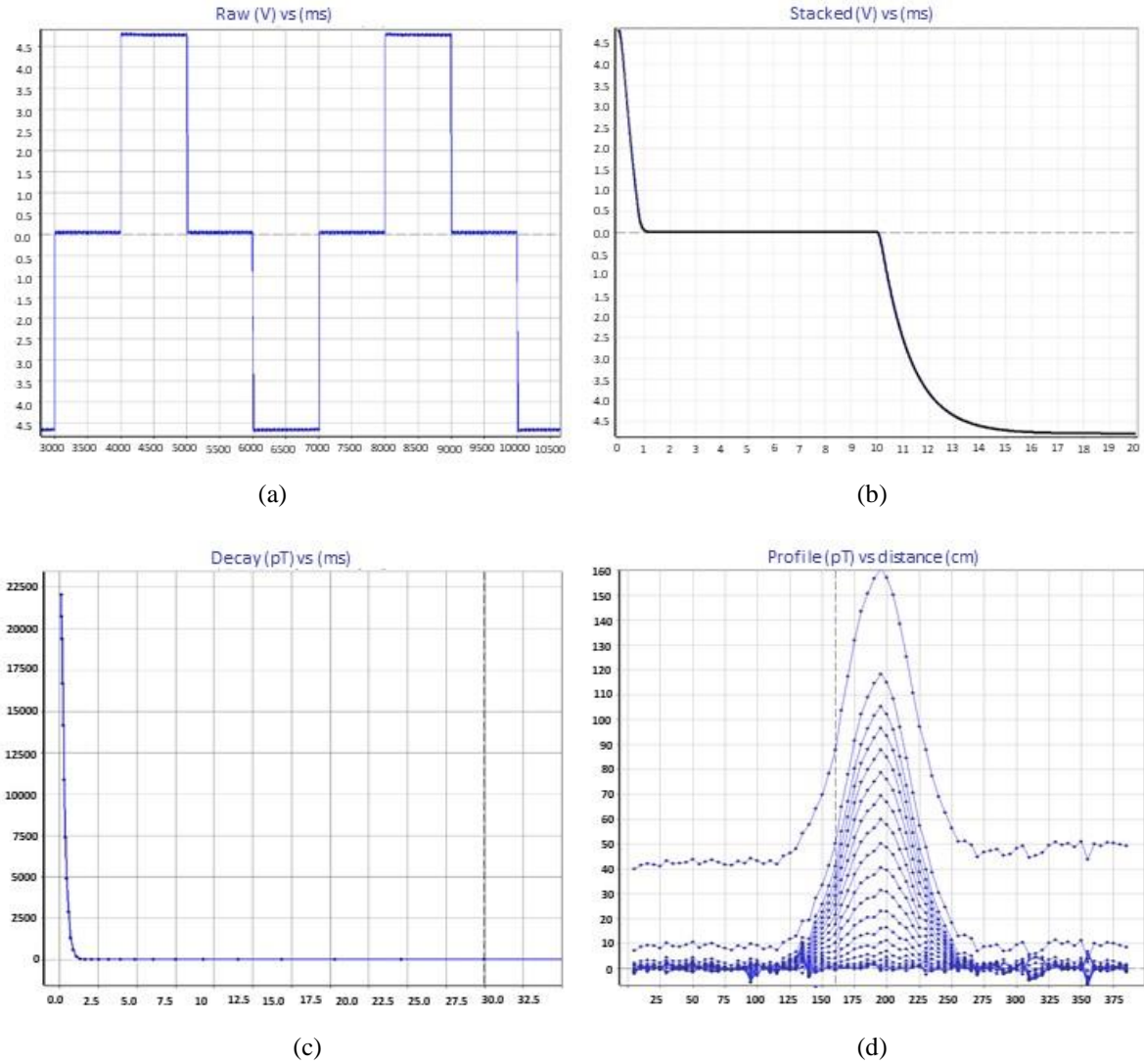


Fig 2.19 Images showing the typical output screens displaying (a) raw data, (b) stacked data, (c) decay and, (d) profile recorded using a magnetometer.

SMARTem24 data acquisition system displaying raw data, stacked data, decay profile and profile data are shown in Fig 2.19 (a), (b), (c) and (d) respectively.

A set of three aluminum plates with length of 300 mm, width of 200 mm and with different thicknesses ranging from 2 mm to 6 mm in steps of 2 mm were scanned below the SQUID. The plates were moved along a platform of 4 m length which was laid 0.5 m below the transmitter. The station interval was chosen to be 0.05 m. At each station, data were recorded, averaged and stacked (128 stacks) in order to reduce noise by using the built-in software in the SMARTem24. The stacked data were further window averaged

and displayed as decay transients as well as station profiles. The decay transient gives the information about the decay of the secondary magnetic field with respect to time and the station profile provides decay of the secondary magnetic field with respect to station for different decay time windows. The same experiments have been repeated by replacing the SQUID with the induction coil sensor for comparison.

2.5. TDEM experiments with induction coil as receiver

The TDEM measurements have been performed by moving the aluminum plates 0.5 m below the transmitter loop with a scanning length of 4 m (2 m on each side of the receiver) and step size of 0.05 m. The decay of the secondary magnetic field recorded by the induction coil for the aluminum plate with thickness of 2 mm, 4 mm and 6 mm moving away from the center of the transmitter loop (from center to 0.25 m in steps of 0.05 m) are shown in Fig 2.20 (a), (b) and (c) respectively. The enlarged views of the same with decay time between 2 ms and 12 ms are shown in Fig 2.20 (d), (e) and (f). The decay data at each location are processed by the SMARTem24 in order to display the secondary magnetic field with respect to the scan coordinates of the aluminum plates (field profile) and the same are shown in Fig 2.21 (a), (b) and (c) for the plate thicknesses of 2 mm, 4 mm and 6 mm respectively. The changes of the induction coil output extracted from the field profile at different time gates for aluminum plate of thicknesses 2 mm, 4 mm and 6 mm have been shown in Fig 2.22 (a) and the enlarged view of the same shown in Fig 2.22 (b). Since the change of the secondary magnetic field due to the change of location of the conducting target (in this case moving aluminum plates) is small as compared to the entire decay, it is difficult to visualize the signal due to the target (overlapping). Hence the offset values between the successive time gates have been removed without altering the signal due to the plates and equal offset values (refer in Fig 2.21) have been introduced for better clarity. From Fig 2.21, it is observed that the voltage change recorded by the induction coil

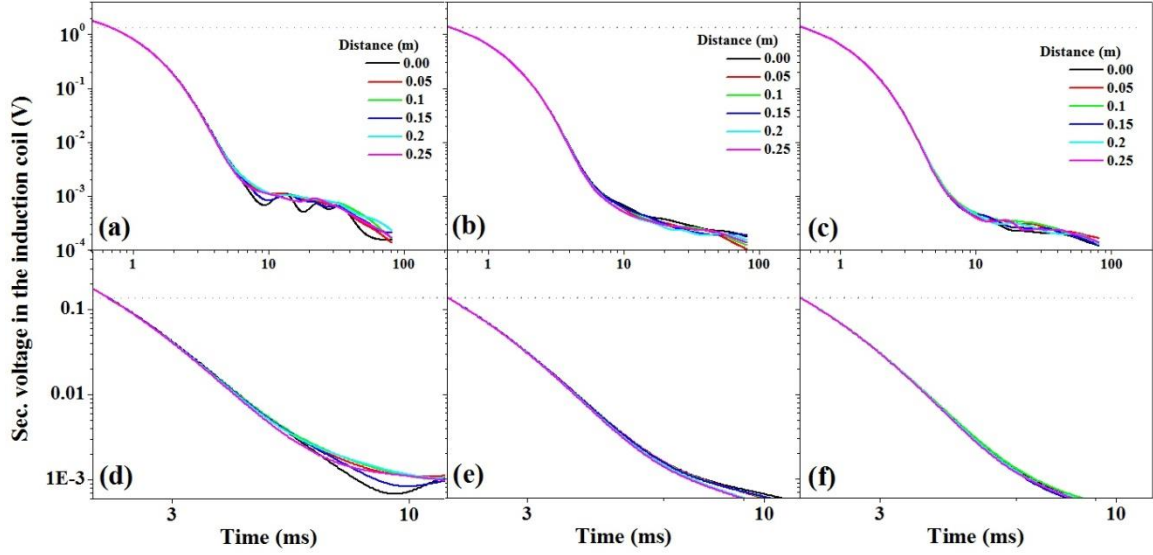


Fig 2.20 (a), (b) and (c) are the decay of the secondary magnetic field recorded by the induction coil for the aluminum plate with thickness of 2 mm, 4 mm and 6 mm moving away from the center of the transmitter respectively and the corresponding enlarged views with time decay between 2 ms and 12 ms are shown in (d), (e) and (f).

is high at early time gates, minimum or zero at intermediate time gates, increases in the reverse direction and reaches the noise floor at later time gates. During the steady flow of current in the transmitter loop, output voltage recorded using the induction coil is zero (induction coil senses only rate of change of magnetic field).

When the transmitter current is suddenly switched off, the output voltage in the induction coil is the summation of the voltage due to the change of the primary magnetic field and the voltage due to the eddy current induced in the conducting target and its associated secondary magnetic field. Therefore, the net voltage in the induction coil at earlier time gate increases, reaches maximum and subsequently decays. The strength of the eddy current induced in the target and its associated secondary magnetic field is proportional to the rate of change of primary magnetic field and the conductivity of the target. In this case, the switch off time of the transmitter is dependent on the inductance and resistance of the transmitter loop (equivalent to excitation frequency in the frequency domain). In addition

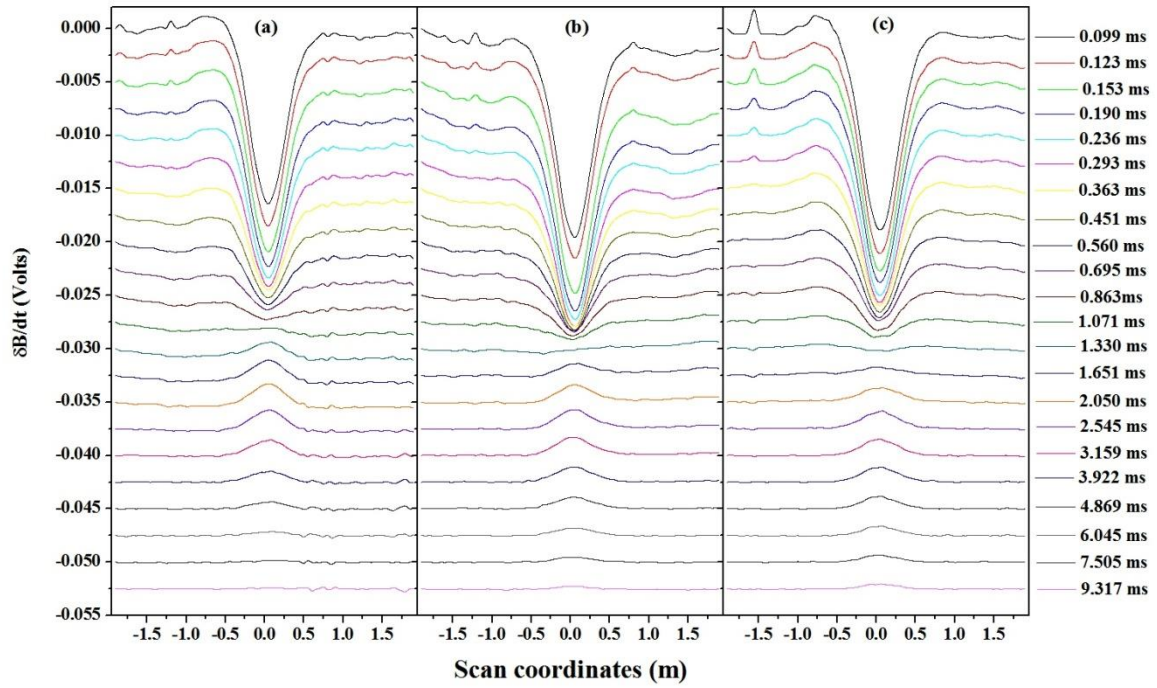


Fig 2.21 Field profile recorded by using an induction coil perpendicular to the plane of the transmitter loop (z component) for the aluminum plates with thicknesses of (a) 2 mm, (b) 4 mm and (c) 6 mm.

to this, the voltage induced in the induction coil is also proportional to rate of change of net magnetic field coupled to the induction coil and hence, the voltage change in the induction coil is high at earlier time gates. When the strength of the induced eddy current in the conducting target and its associated secondary magnetic field reaches a maximum value, the voltage change in the induction coil is zero which was observed at the time gate of 1.071 ms for the plate with thickness of 2 mm (refer Fig 2.21). Subsequently, the induced eddy

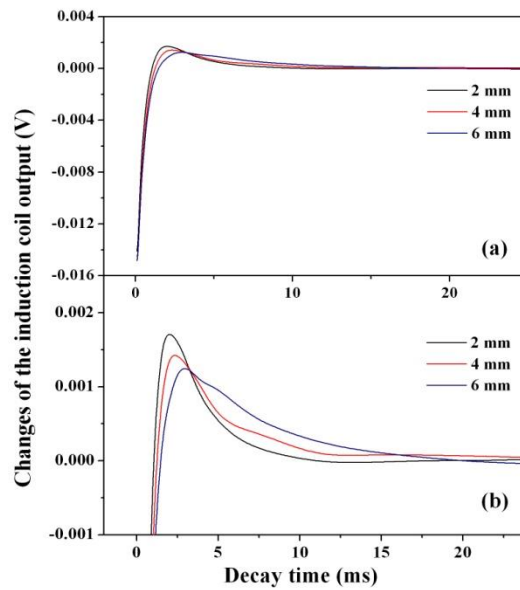


Fig 2.22 (a) Changes of the induction coil output at different time gates for the aluminum plate thicknesses of 2 mm, 4 mm and 6 mm (b) enlarged view of the same.

current starts decaying and its rate of decay depends on the conductivity of the target. The depth at which the decay of the eddy current reaches maximum is the diffusion depth which is analogous to skin depth of the material in frequency domain measurements. The induced eddy current starts decaying and the decay rate is maximum at time gate of 2.05 ms (refer Fig 2.21 and peaks in Fig 2.22). At later times, the induced eddy current decays further reaching zero and the corresponding secondary magnetic field is measured by the induction coil which reaches its noise floor. Similarly, as we increase the plate thickness (4 mm and 6 mm), there is a small change of output voltage in the induction coil due to the induction of eddy currents at earlier time gates. At the same time, the change of output voltage due to the decay of the secondary magnetic field is very small with the increase of plate thicknesses. This is due to the slow variation of the secondary magnetic field or the persistence of eddy current in the target for longer time (refer Fig 2.21 (b)). In other words, it can be said that the voltage induced in the induction coil decays much faster than the decay of the secondary magnetic field itself. Therefore, the induction coil sensors are not suitable for the TDEM measurements with the earth surface covered by a highly conducting layer (conducting overburden).

2.6. TDEM experiments with SQUID as receiver

The same experiments have been repeated simply by replacing the induction coil with SQUID sensor. The decay of the secondary magnetic field recorded by the SQUID for the aluminum plates with thickness of 2 mm, 4 mm and 6 mm moving away from the center of the transmitter loop (from center to 0.25 m in steps of 0.05 m) are shown in Fig 2.23 (a), (b) and (c) respectively. From Fig 2.23 one can observe that there is a large change of the decay of the secondary magnetic field recorded by the SQUID receiver as the aluminum plate moves from one location to another location as well as increasing the plate thicknesses. The decay data at each location is processed by the SMARTem24 in order to

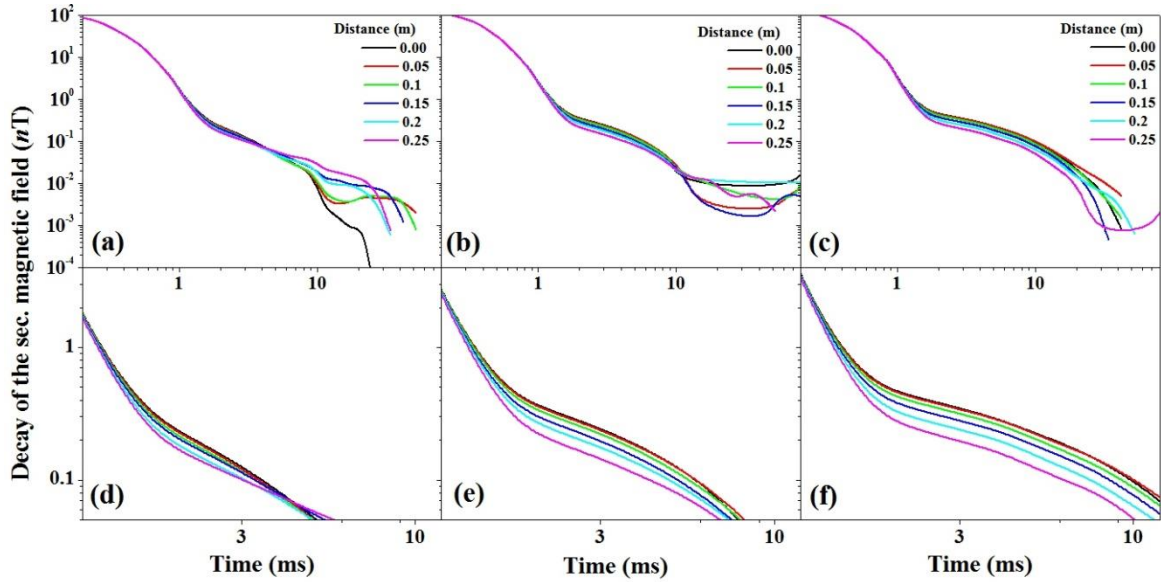


Fig 2.23 (a), (b) and (c) are the decay of the secondary magnetic field recorded by the induction coil for the aluminum plate with thickness of 2 mm, 4 mm and 6 mm moving away from the center of the transmitter respectively and the corresponding enlarged views with time decay between 2 ms and 12 ms are shown in (d), (e) and (f).

display the secondary magnetic field with respect to the scan coordinates of the aluminum plates (field profile) are shown in Fig 2.24 (a), (b) and (c) for the plate thicknesses of 2 mm, 4 mm and 6 mm respectively. From Fig 2.24 it is observed that the strength of the secondary magnetic field increases with the conducting thickness of the aluminum plate even at later time gates. Since the SQUID is a B-field sensor, the SQUID produces steady output voltage during the steady flow of current in the transmitter loop. When the transmitter current is suddenly switched off, the output voltage of the SQUID is again the summation of the voltage due to the change of the primary magnetic field and the voltage due to the eddy currents induced in the conducting target and its associated secondary magnetic field. When the conducting plate thickness increases, the induced eddy currents persist for longer time and its slow decay can be measured by the SQUID. This shows that the SQUID sensors measure the decay of the secondary magnetic field due to the conducting target covered by highly conducting upper layers. The changes of the SQUID

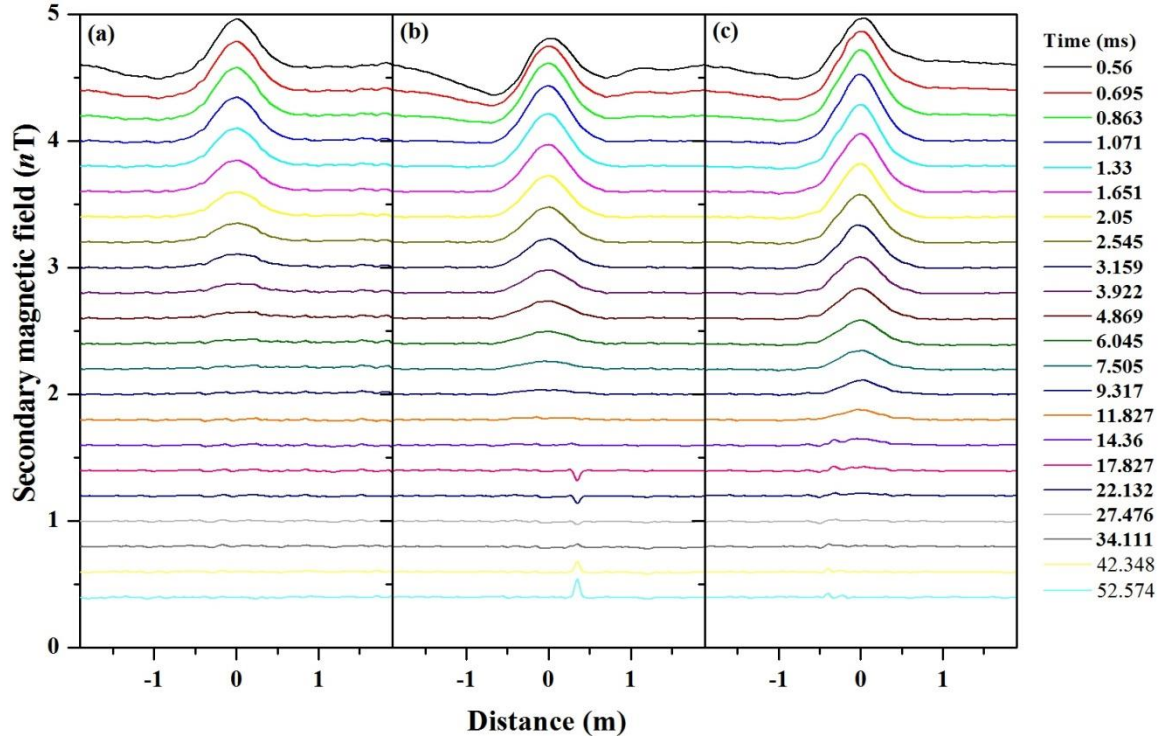


Fig 2.24 Field profile recorded by using SQUID sensor perpendicular to the plane of the transmitter loop (z component) for the aluminum plates with thicknesses of (a) 2 mm, (b) 4 mm and (c) 6 mm.

output extracted from the field profile at different time gates for the aluminum plate thicknesses of 2 mm, 4 mm and 6 mm are shown in Fig 2.25 for comparison with the induction coil.

The profile data recorded by the induction coil and SQUID without altering the offset values between the time gates for the aluminum plates with thickness of 2 mm, 4 mm and 6 mm are given in Fig 2.26 and Fig 2.27 respectively. There is no response of the induction coil for conducting targets located far away from the

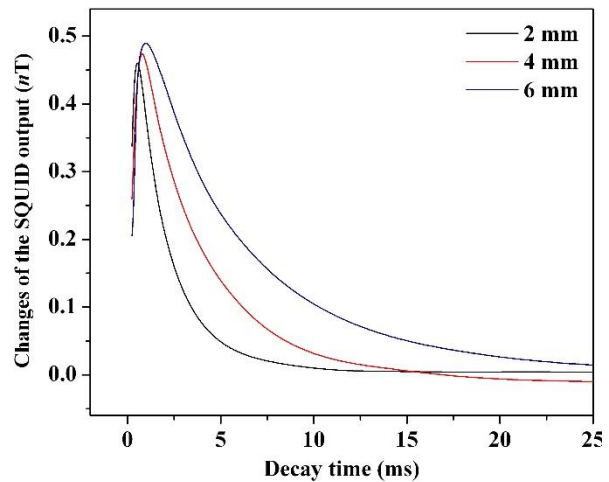


Fig 2.25 Changes of the SQUID output at different time gates for the aluminum plate thicknesses of 2 mm, 4 mm and 6 mm.

center of the receiver either in the early time gates or late time gates. But the SQUID shows the progressive response as the conducting target thickness increases even when the target is far away from the receiver and even at later time gates. It shows that the SQUID sensor is more suitable to locate the conducting target buried in deep sub-surface of the earth due to its extremely high sensitivity maintained at low frequency.

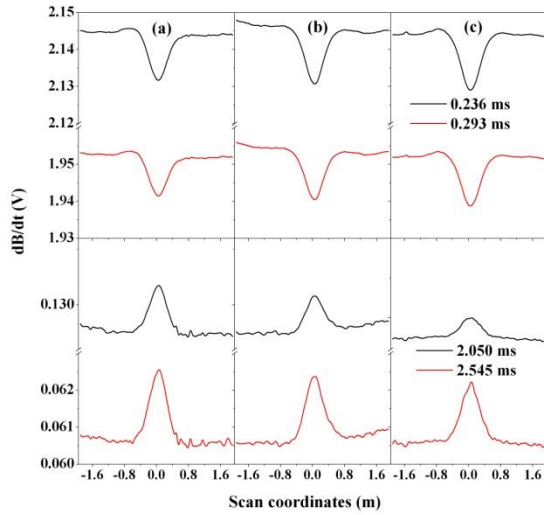


Fig 2.26 Profile recorded by the induction coil at early and late time gates for the aluminum plates with thickness of (a) 2 mm, (b) 4 mm and (c) 6 mm.

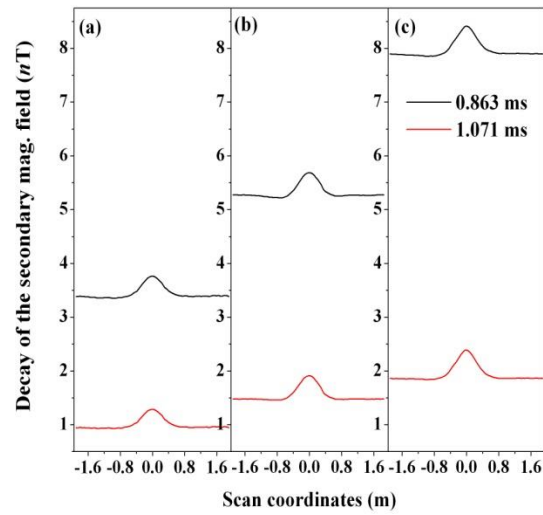


Fig 2.27 Profile recorded by the SQUID for the aluminum plates with thickness of (a) 2 mm, (b) 4 mm and (c) 6 mm.

Chapter 3

TDEM SURVEY AT TUMALAPALLE USING SQUID, INDUCTION COIL AND FLUXGATE

This chapter provides (1) a brief description of advantage of magnetic field sensors over induction coils in the central loop TDEM sounding measurements in different terrains, (2) simulations showing the advantage of increasing the transmitter moment and its effect on the depth of investigation, (3) details of the central loop sounding at a test site and (4) detailed description and experimental results of central loop sounding measurements performed at Tumallapalle, YSR Kadapa district, AP, India using the SQUID, induction coil, and fluxgate magnetometer.

3.1. Introduction

Time-domain electromagnetic sounding in central loop configuration is an essential electromagnetic geophysical technique that has been successfully used for numerous applications that require information on the variation of conductivity/resistivity with vertical depth below the surface of the earth [87]. The TDEM central loop sounding technique finds application in estimating approximate depth and thickness of mineralized zones, approximating depth of ground-water table as well as imaging presence of salt-water layers [36–39].

The TDEM central loop sounding measurements record the vertical component of the ground response in a horizontally layered earth. Such measurements are generally performed using large transmitter loops usually in the form of a square while the receiver is located at the center of the loop. The expression for the maximum depth of investigation, d , for a single layer homogeneous half space geophysical model [20] with a magnetic field sensor (B-field) is

$$d = 2.8 \times 10^{-3} \left(M / \eta_B \right)^{1/3} \quad (3.1)$$

and the same with an induction coil ($\partial B / \partial t$) is

$$d = 0.55 \left(M / \sigma \eta_V \right)^{1/5} \quad (3.2)$$

where M is the transmitter moment (product of the transmitter current, number of turns and area of the transmitter loop), σ is the conductivity of the earth and η_B and η_V are the system noise of the magnetic field sensor and induction coil respectively. From the above equations, it is clear that the investigation depth is proportional to the transmitter moment for a given system noise of the receivers used [88].

In case of TDEM measurements for a terrain where thin conductive layer is buried under thick conductive layer (conductive overburden), the voltage induced in the induction coil is very small due to slow decay of the eddy current. This low voltage in the induction coil reaches its noise floor much earlier than the decay of the eddy current induced in the buried thin conducting layer. This is because the voltage induced in the induction coil decays much faster than the decay of the secondary magnetic field itself. At the same time, B-field sensors like SQUIDs can measure the decay of secondary magnetic field even at a later time due to its sensitivity at low frequencies [65].

Similarly, it is well known that the TDEM measurements are highly transparent for a resistive terrain where negligible or weak eddy currents are induced. At the same time, when a thin conductive layer is buried under thick resistive layer (resistive overburden), the induced eddy currents in the thin conducting layer will decay at later time. In order to enhance the target resolution, transmitter loop with larger size and larger current are required to induce sufficient eddy currents in the thin conducting layer. The target resolution can be achieved even with the use of portable TDEM systems with SQUID as a receiver.

In view of this, the developed SQUID based TDEM system has been utilized in a terrain similar to one mentioned above, that is, a thin conducting layer buried under thick highly resistive layer. To compare the performance of the SQUID, TDEM measurements have also been performed using the indigenously built induction coil as well as the commercial fluxgate magnetometer Mag-03-CL100 described earlier. The TDEM measurements performed with the three different sensors with different transmitter loop sizes and the results obtained have been discussed in detail in this chapter.

3.2. Simulations of central loop sounding results using synthetic forward models

Equation 3.1 clearly shows that using magnetometer such as SQUID for TDEM central loop sounding over a particular terrain, the depth of investigation can be enhanced by increasing the transmitter moment. The transmitter moment (M) is the product of transmitter current (I), number of turns of the transmitter loop (N) and the area of the transmitter (A) [89].

The one-dimensional layered earth is a useful model to understand the behavior of secondary magnetic field response at different depths [59]. Various models involving isolated conductive targets in resistive backgrounds, such as a buried conductive sphere or a rectangular conductive plate can be found in literature [67,90]. Likewise, Maxwell (EMIT, 2005) is a geophysical electromagnetic modeling software that can be used to simulate three-dimensional forward models showing response of targets like thin plates to transient electromagnetic fields. Maxwell aids in the processing, visualization, and modeling of electromagnetic geophysical data. It supports both time and frequency domains as well as ground and airborne systems. For given source parameters such as transmitter moment, base frequency and duty cycle of the transmitter waveform, type of sensor, etc., the Maxwell forward model algorithm calculates the EM response of a thin

rectangular conductive plate by assuming that it constitutes of a number of ribbons representing wire loops carrying the induced eddy currents.

Maxwell thin plate models can be generated to understand and predict the decaying secondary magnetic field response from layered structures. One such layered model is used here to simulate the response to an applied TDEM excitation signal and a screenshot of the same is shown in Fig 3.1. The model consists of a three-layered structure where the upper layer is a highly conductive overburden plate (P1) lying on the surface just below the transmitter loop, a thick resistive intermediate layer and a highly

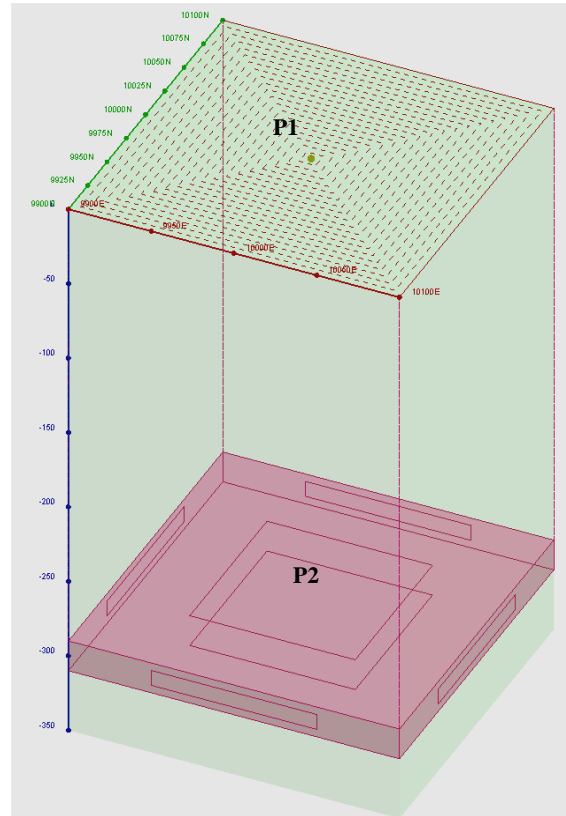


Fig 3.1 Maxwell plate model showing top plate (P1) used for overburden simulation and bottom plate (P2) for conductive target below intermediate resistive layer.

conductive plate (P2) at a depth of about 300 m from the surface. Since Maxwell assumes a highly resistive background by default, no plate was used in between P1 and P2 to simulate the intermediate resistive layer. Both plates are square in shape and the important parameters such as conductivity and thickness of the plates are listed in Table 3.1 and the same are maintained constant throughout the simulations. The central loop vertical

Table 3.1 Parameters of the conductive plates used in the simulations.

| Plate | Side length (m) | Depth of center of plate from surface (m) | Thickness (m) | Conductivity (S/m) |
|-------|-----------------|---|---------------|--------------------|
| P1 | 200 | 0 | 0 | 10 |
| P2 | 200 | 300 | 20 | 0.3 |

magnetic field decay response of the layered structure to a square transmitter loop of side length of 100 m, 1 turn and 5 A current is shown in plots in log-log scale in Fig 3.2. The figure shows two plots where one (black) corresponds to the response of the model in the absence of conductive target P2 while the other plot (red) corresponds to the response in the presence of plate P2.

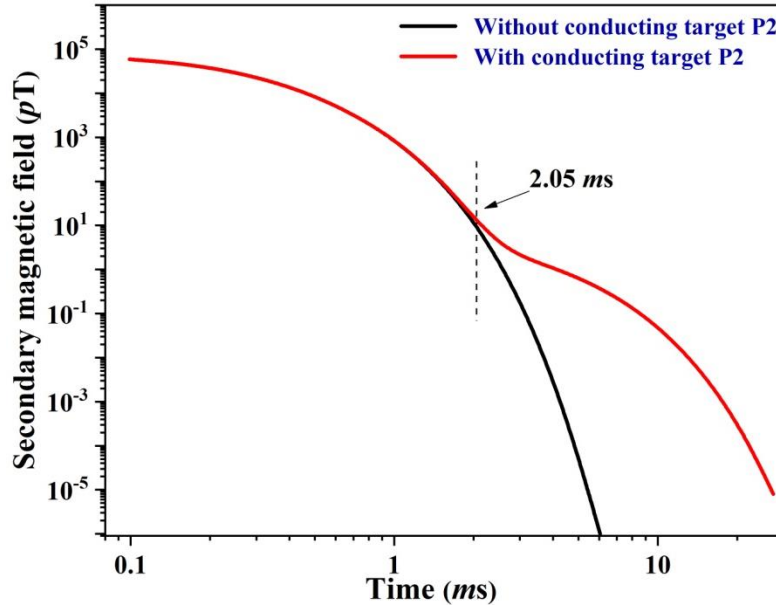


Fig 3.2 Plots in log-log scale showing vertical magnetic field response of a layered model with a square transmitter loop of side length of 100 m and current of 5 A.

The second one show a variation of the secondary magnetic field at a decay time of 2.05 ms and the decay slows down which corresponds to the second conductive layer (P2). This earliest time at which a buried target response is visible (called Time of Response or ToR hereafter) is of great importance to the geophysical exploration survey and the advantage of using a magnetic field sensor to achieve earlier ToR has been discussed elsewhere [91].

In order to understand the changes of ToR, simulations were further performed using the same thin plate model with increasing the parameter values such as N , I and A of the transmitter loop and the secondary magnetic field have been obtained by B-field sensor.

3.2.1. Effect of increasing transmitter current

In the first set of simulations, a square transmitter loop of side length of 100 m was used and the current in the loop was varied to visualize the effect on the vertical component of

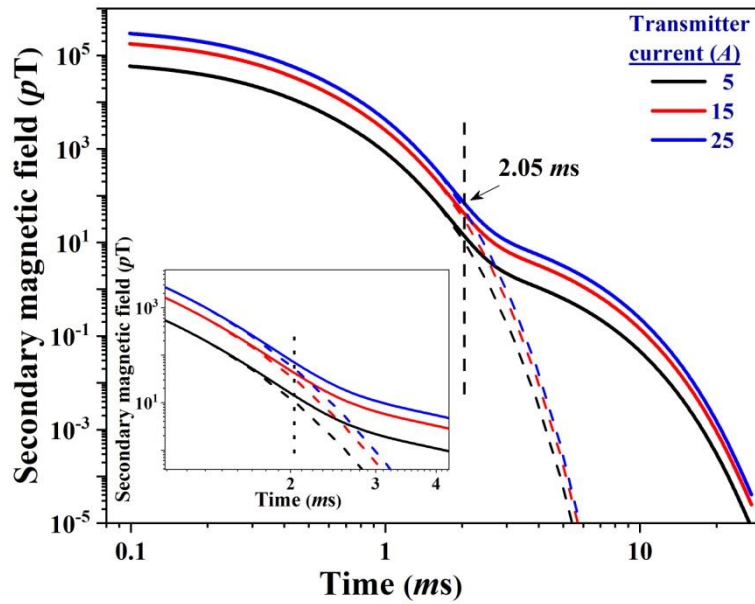


Fig 3.3 Simulated log-log plots showing decay of vertical component of secondary magnetic field over a layered model for different Tx currents using one turn square transmitter loop of side length of 100 m.

the secondary magnetic field. The decay of the vertical component of secondary magnetic field obtained at the center of the loop is presented in a log-log scale in Fig 3.3. For the sake of clarity, the plots have been zoomed around the ToR and presented in the inset. As the Tx current increases, the primary magnetic field increases (Fig 3.4) throughout the vertical section of the layered model from the surface to deeper layers and this results in overall increase in the secondary magnetic field induced at each depth. However, the ToR of the conductive layer is constant (2.05 ms in

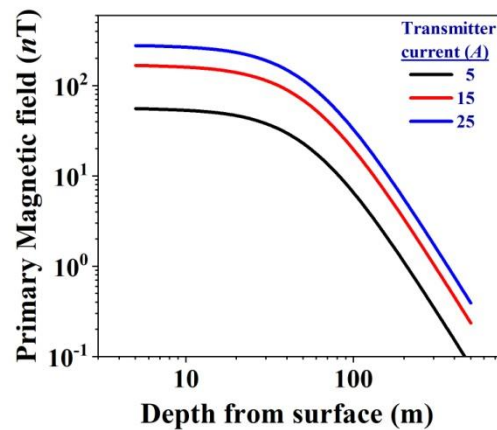


Fig 3.4 Primary magnetic field versus depth for different transmitter currents.

this case) for different currents. Since increasing current results in increase of the central magnetic field on the surface where the magnetic field sensor would be located which may affect the sensor parameter such as slew rate (T/s) of the SQUID.

3.2.2. Effect of increasing number of turns of the transmitter loop

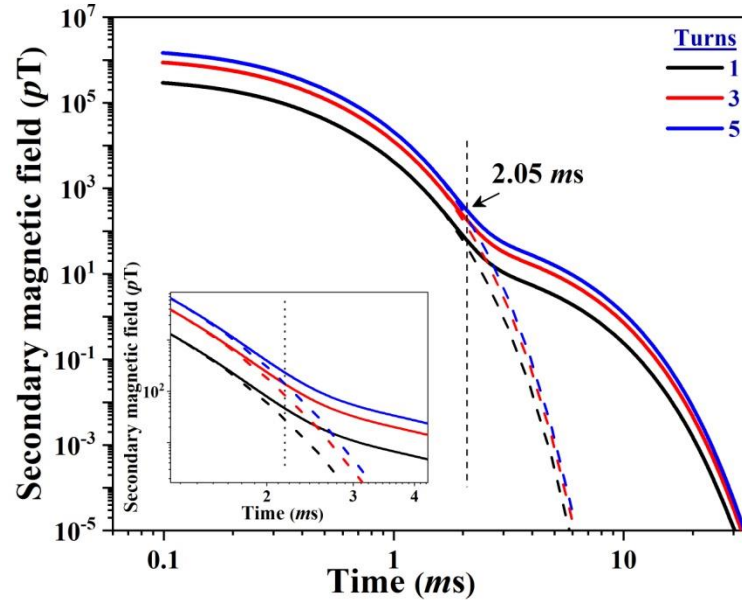


Fig 3.5 Simulated plots in log-log scale showing decay of vertical component of secondary magnetic field over a layered model for different turns of Tx loop with 25 A current transmitted using the loop of side 100 m.

The increase in the number of turns of the Tx loop shows results similar to that of increasing current in the loop. The number of turns is varied from 1 through 5. The decay of the secondary magnetic field obtained at the center of the loop corresponding to 1, 3 and 5 turns of Tx loop is presented in log-log scale in Fig 3.5. For the sake of clarity, the plots have been zoomed around the ToR and presented in the inset. With the increase of number of turns, there is a proportional increase in

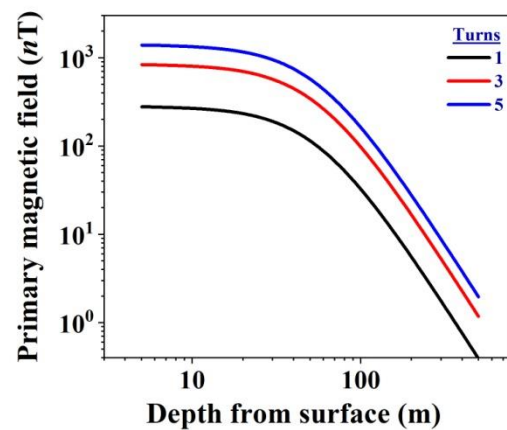


Fig 3.6 Variation of magnetic field with depth below the surface with different Tx turns.

the vertical component of the primary magnetic field (Fig 3.6) and the secondary field response also increases proportionally. However, the ToR is same that is 2.05 ms for different turns of the transmitter loop.

3.2.3. Effect of increasing the area of the transmitter loop

In the third set of simulations, the current in the transmitter loop and the number of turns are maintained at 25 A and one respectively and the area of the transmitter loop has been varied. The side lengths and the corresponding areas of the transmitter loops are 100 m, 200 m and 400 m and 10^4 m^2 , $4 \times 10^4 \text{ m}^2$ and $16 \times 10^4 \text{ m}^2$ respectively. Fig 3.7 shows the results of the decay plots obtained at the center of the loop for transmitter with different loop areas. Fig 3.8 shows the variation of vertical component of primary magnetic field for

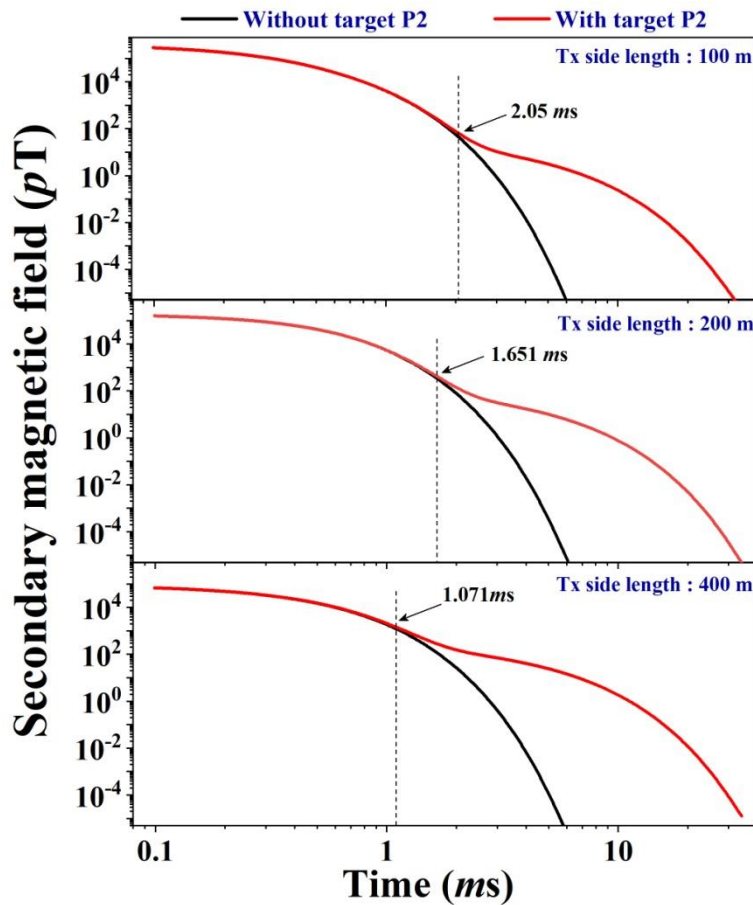


Fig 3.7 Simulated log-log plots showing decay of vertical component of secondary magnetic for Tx loops of different sizes with transmitter current of 25 A.

the three different loop sizes. Unlike the previous cases, here, increasing the loop area resulted in a reduction in the magnetic field at the center of the loop while the magnetic field at depth is relatively higher for the loop with larger area. This results in an increase in the strength of the induced

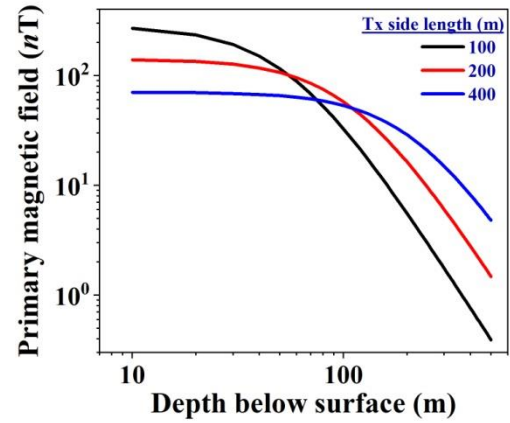


Fig 3.8 Variation of primary magnetic field versus depth with transmitters of different sizes.

magnetic field in a conductive target at depth for transmitter loops with larger area. As a result, the buried plate can be seen at an earlier time (1.071 ms) while using Tx loop of side 400 m compared to the use of Tx loop of side 100 m (2.05 ms). Therefore, while using magnetic field sensors for deeper investigation, it is essential to increase the magnetic moment by using Tx loops with larger area. This increases the magnetic field strength at depth which, in turn, increases the signal strength at the target thus enhancing the ToR. Further, since the central magnetic field is relatively less for larger Tx loops, the magnetic field sensors, such as the SQUID can be used with higher FLL gain at the center of the loop.

3.3. Central loop sounding test at Kalpakkam (Site 1)

Before performing actual field survey using the SQUID magnetometer, the system was tested in a relatively noisy environment at a site located in Kalpakkam, Tamil Nadu, India (Site 1) near the laboratory using a square transmitter loop of side 100 m. The stratigraphy of this site is unknown and therefore an apparent conductivity-depth inversion is also performed for the data obtained at this site.

3.3.1. Experimental details and results

Central loop TDEM measurements have been performed using a square transmitter loop of side length of 100 m at a test site located about 250 m away from shore of the Bay of



Fig 3.9 Satellite image showing coordinates of the corners of square transmitter loop of side 100 m and the of loop where the SQUID magnetometer is placed during measurement at Site 1.

Bengal (Site 1) at Kalpakkam, India. A satellite image showing the coordinates of the transmitter loop and the location of the receiver (SQUID) at Site 1 is shown in Fig 3.9. The details of the Tx loop size, current, etc. are presented in Table 3.2. A trapezoidal current pulse of 25 A with different base frequencies was passed through this loop resulting in 283 nT of central magnetic field and the equivalent transmitter moment is $2.5 \times 10^5 \text{ Am}^2$. The SQUID sensor was placed at the center of the loop and the raw data corresponding to the vertical component of magnetic field was recorded over a large number of stacks and further processed to obtain the final decay of the secondary magnetic field with time.

The recorded values of the secondary magnetic field obtained from the central loop measurements with SQUID at different base frequencies are shown in Fig 3.10 in log-log scale. The slow decay at early stages can be attributed to conductive upper layer. The

asymptotic decay at intermediate stage slows down at 0.863 ms showing the possible presence of a conductive layer.

Table 3.2 Details of TDEM survey parameters set for central loop sounding measurements at Site 1.

| Side length of the Transmitter loop (m) | Transmitter current (A) | Transmitter moment (Am^2) | Central field (nT) |
|---|-------------------------|--------------------------------------|--------------------|
| 100 | 25 | 2.5×10^5 | 283 |

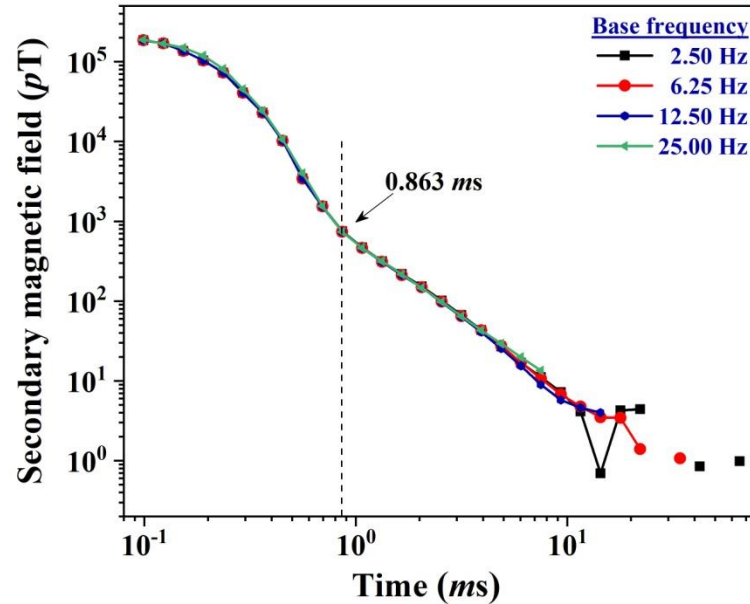


Fig 3.10 Transients showing decay of vertical component of secondary magnetic field recorded at Site 1 using SQUID sensor for transmitter currents of different base frequencies.

3.4. Central loop TDEM survey at Tumallapalle (Site 2)

After successful TDEM tests at Site 1, the central loop sounding measurements using the SQUID sensor were performed near Tumullapalle Uranium mine, Andhra Pradesh. The experiments were also performed using the home-built induction coil and the commercial fluxgate magnetometer. The experimental results obtained by using different sensors were analyzed and compared.

3.4.1. Details of terrain

The Tummallapalle uranium mine is located in the YSR Kadapa district of Andhra Pradesh, in the southern part of India. Geologically, Tummallapalle is in the south western part of the Kadapa basin. Dolostone hosted uranium mineralization occurs in the Vempalle

formation of Kadapa basin intermittently over a strike length of 160 km from Reddypalle in NW to Maddimadugu in the SE [92].

Lithologically, this Vempalle formation consists of massive limestone, purple shale, intraformational conglomerate, dolostone (uraniferous), shale and cherty limestone.

The impersistent conglomerate and purple shale band occurring immediately below and above the mineralized rock respectively, serve as the marker horizons [93]. The stratigraphy of the terrain where the SQUID based TDEM central loop sounding has been performed is shown in Fig 3.11. It consists of a layer of overburden, followed by thick layer of cherty limestone (~ 200 to 250 m) which is highly resistive in nature. The shale layer located just below the limestone is thin (15 to 20 m) and conductive. As far as TDEM measurements are concerned, the layers of the earth have been considered as upper

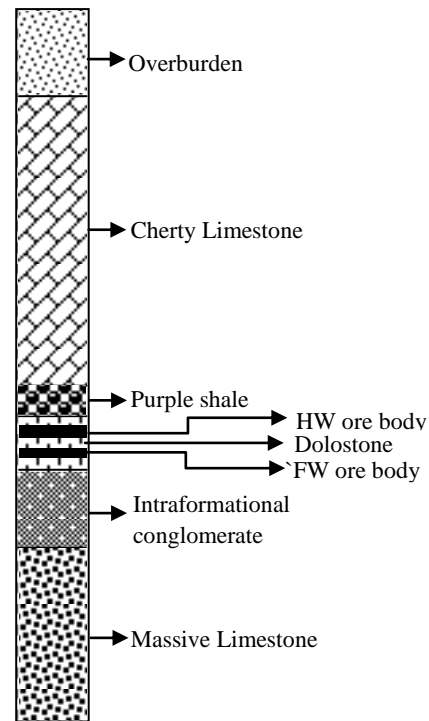


Fig 3.11 The stratigraphy of the terrain

conductive weathered, resistive overburden (cherty limestone), thin conducting layer (shale) and the remaining layers are resistive. The results obtained from TDEM survey using SQUID show better target resolution for the conductive shale layer as compared to other sensors.

3.4.2. Experimental details

The Site 2 was chosen based on prior information regarding the lithological structure of the region as discussed in section 3.4.1. During this study, SQUID based TDEM central loop sounding measurements have been carried out with transmitter loops of different

sizes and with different currents. The TDEM survey parameters set in the measurements are listed in Table 3.3. These measurements were also performed with different base frequencies (2.5 Hz, 6.25 Hz, 12.5 Hz and 25 Hz) and with different stacks (16 to 2048).

Table 3.3 Details of TDEM survey parameters set for central loop sounding measurements at Site 2.

| Side length of the Transmitter loop (m) | Transmitter current (A) | Transmitter moment (Am^2) | Central field ($n\text{T}$) |
|---|-------------------------|--------------------------------------|-------------------------------|
| 100 | 25 | 2.5×10^5 | 283 |
| 400 | 27 | 4.32×10^6 | 81 |

At the center of the transmitter loop, the cryostat containing the SQUID probe has been partially buried in the ground in order to arrest the wind-generated mechanical vibrations. Similarly, the TDEM sounding measurements were repeated by replacing the SQUID with the induction coil and the fluxgate magnetometer in order to compare the performance of the SQUID. The photograph of the experimental site along with the coordinates of the square transmitter loop of side length 400 m and the experimental setup has been shown in Fig 3.12.

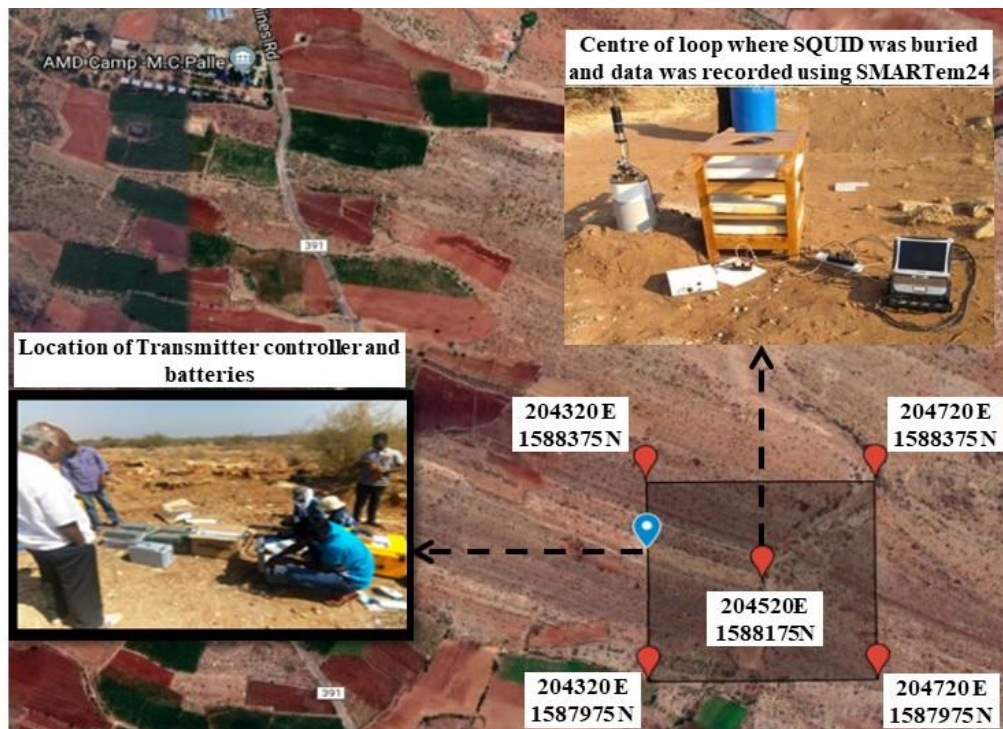


Fig 3.12 Satellite image showing coordinates of the transmitter loop with side length of 400 m along with photographs showing the data acquisition system and the partially buried SQUID at center of the loop and location of transmitter and batteries.

3.4.3. Results and discussion

The decay of the secondary magnetic field recorded with base frequency of 6.25 Hz and with transmitter loop size of 100 m x 100 m and 400 m x 400 m using induction coil is shown in Fig 3.13 (a) and (b) respectively. Similarly, the decay of the secondary magnetic field recorded using the SQUID sensor for the loop of side length of 100 m and 400 m are shown in Fig 3.13 (c) and (d) respectively. Here, the data has been shown for different stacks starting from 64 to 1024.

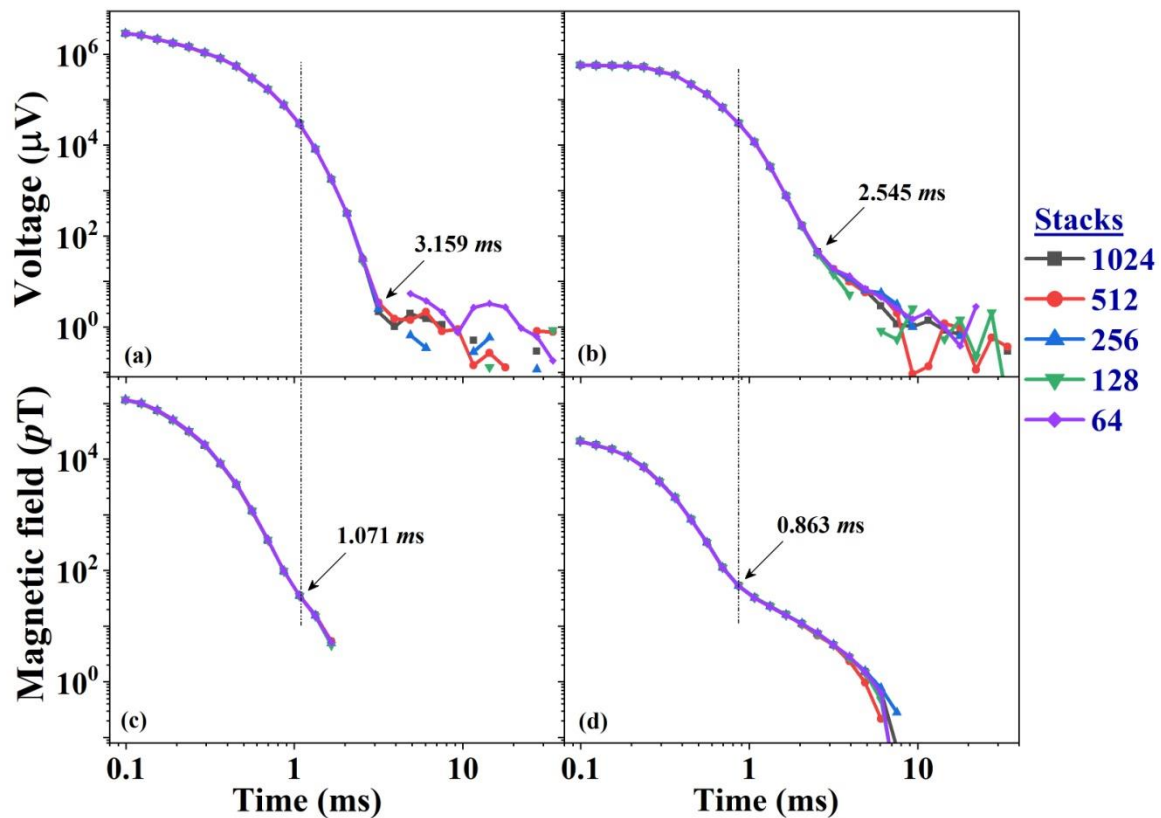


Fig 3.13 Plots in log-log scale showing decay of the vertical component of the secondary magnetic field recorded with base frequency of 6.25 Hz using induction coil with transmitter loop size of (a) 100 m x 100 m, and (b) 400 m x 400 m. Similarly, (c) and (d) correspond to decay of the secondary magnetic field recorded using SQUID with transmitter loop size of 100 m x 100 m and 400 m x 400 m respectively with the same base frequency.

With the transmitter loop size of 100 m x 100 m, the decay of the secondary magnetic field recorded with induction coil has not shown any signature for the presence of thin conducting target. The induced secondary magnetic field decays monotonically up to

3.159 ms and subsequently reaches its noise floor. For the same transmitter moment, the decay of the secondary magnetic field due to the thin conducting target is merely visible with SQUID sensor at a time of 1.071 ms after switching off the transmitter current and further the decay goes to negative values which could not be shown in the log-log scale.

To increase the depth of investigation, the transmitter loop size is increased from 100 m x 100 m to 400 m x 400 m and the applied transmitter current has been maintained at a value of 27 A resulting in central magnetic field strength of 81 nT and transmitter moment of $4.32 \times 10^6 \text{ Am}^2$. The decaying secondary magnetic field recorded using induction coil (Fig 3.13 (b)) shows the signature of the thin conducting layer after 2.545 ms but the signal is still noisy even with 1024 stacks. This is because the signal for the conducting target appears at later time where the rate of change of secondary magnetic field is very

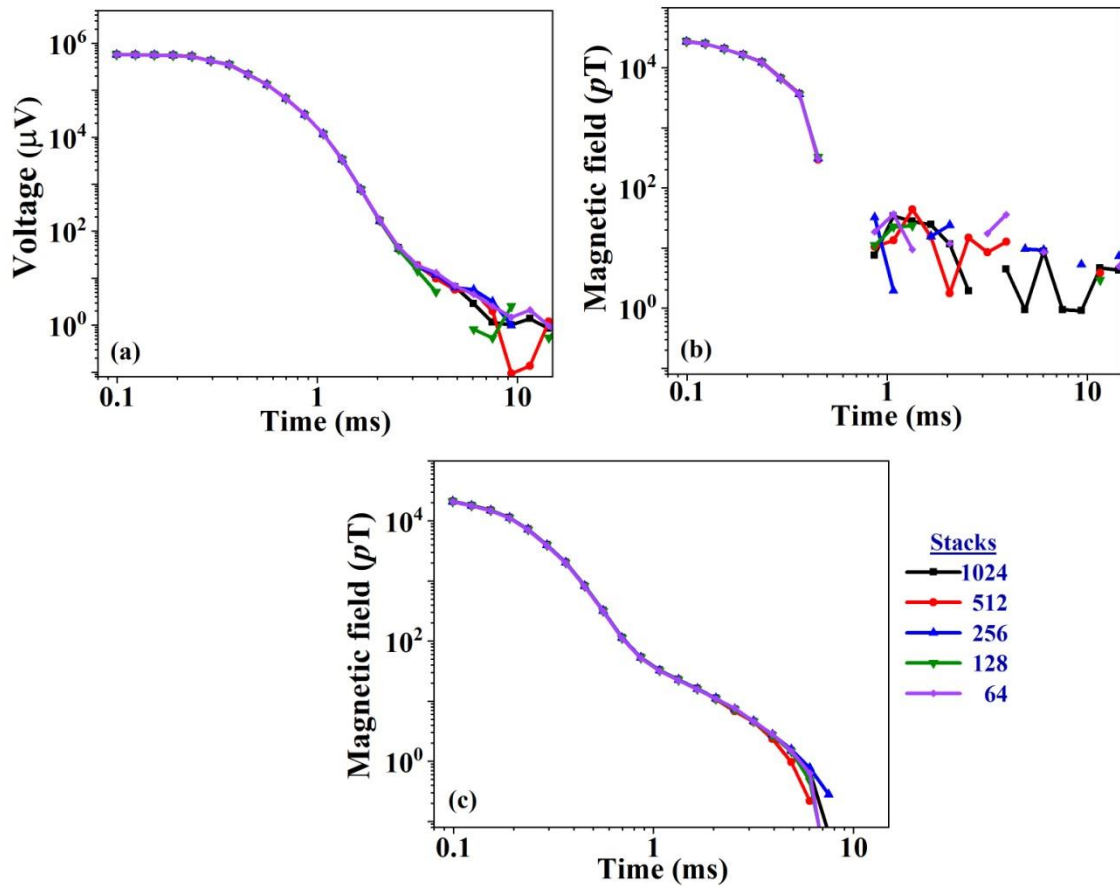


Fig 3.14 Decay of the vertical component of the secondary magnetic field recorded with base frequency of 6.25 Hz and with transmitter loop size of 400 m x 400 m using (a) induction coil, (b) fluxgate, and (c) SQUID.

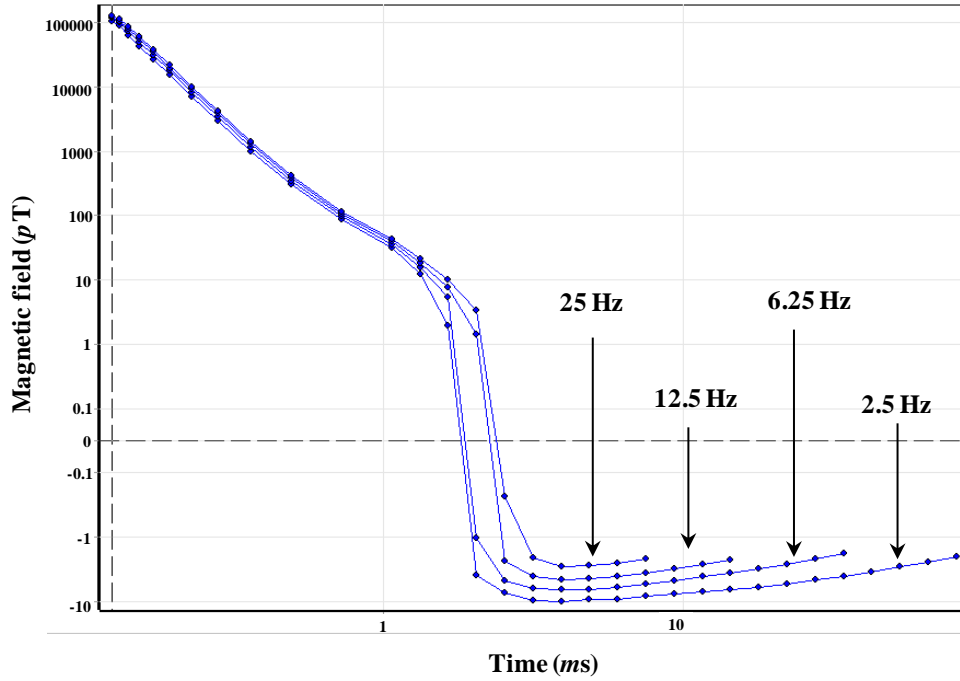
small. The data recorded with the SQUID shows the signature of the conducting layer at 0.863 ms with excellent signal strength and continues to decay slowly up to 7 ms and further tends to decay faster which corresponds to the second resistive layer. In addition to this, the performance of the SQUID is almost independent of number of stacks. The target resolution has been drastically improved by increasing the transmitter moment with the use of larger transmitter loop and compact transmitter (current of 30 A).

The vertical component of the decaying secondary magnetic field recorded with an induction coil, fluxgate and SQUID using the transmitter loop of side length of 400 m, are shown in Fig 3.14 (a), (b), and (c) respectively. Compared to the decays recorded using the induction coil and the SQUID, the results from data recorded using fluxgate shows unusual response as the magnetic field reaches negative values at intermediate times due to its dual behavior. This means that the fluxgate sensor behaves like an induction coil at early time (high frequency region) and magnetic field sensor at later time (low frequency region). Such dual behavior of the fluxgate sensor in transient magnetic field measurements in geophysical applications is described in detail in the subsequent chapter. Comparing the target responses recorded by the SQUID and fluxgate, it is clear that the target gives its response at a time of 0.863 ms. However, the fluxgate reaches its noise floor at this time due to its poor sensitivity and at the same time, the SQUID senses such low secondary magnetic field.

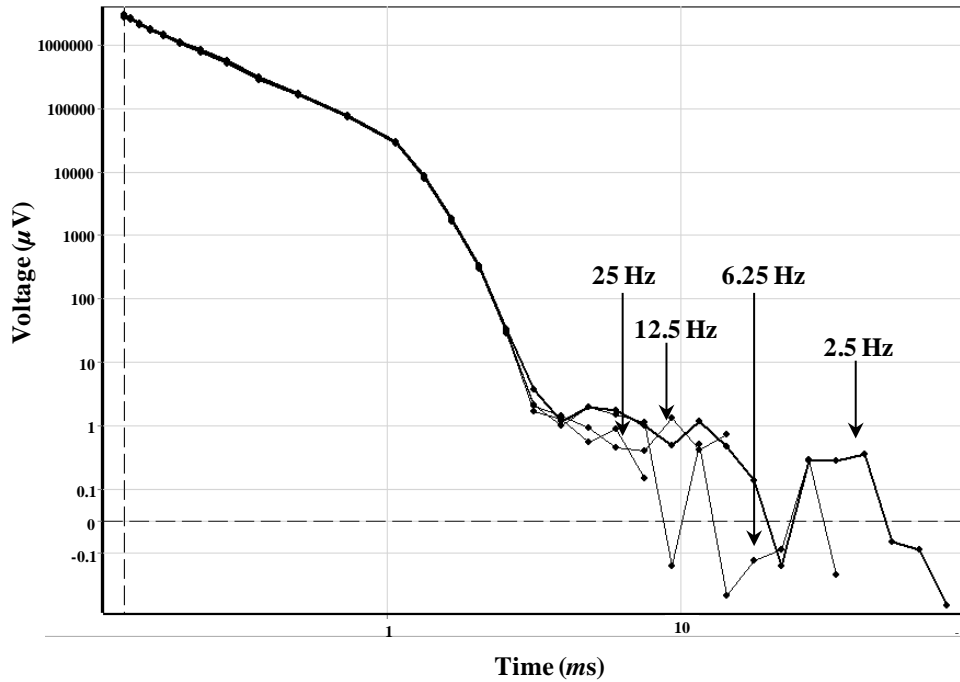
Overall, the central loop sounding measurements with SQUID shows the decay of the secondary magnetic field for all layers such as weathered, resistive (limestone), conductive (shale) and second resistive (limestone) with better resolution as compared to the other sensors.

The sounding measurements have been repeated with different base frequencies from 2.5 Hz to 25 Hz. The decay of the secondary magnetic field recorded using the SQUID and

induction coil with different base frequencies for the transmitter loop size of 100 m x 100 m are shown in Fig 3.15 (a) and (b) respectively. These log-log plots are screenshots as recorded by the SMARTem24 data acquisition system. The recorded response of the SQUID shows the frequency dependence of the applied base frequency of the transmitter



(a)



(b)

Fig 3.15 The decay of the secondary magnetic field (log-log scale) recorded by (a) SQUID and (b) induction coil with different base frequencies for transmitter loop of side length 100 m with applied current of 25 A.

current and zero cross over at later times of the decay of the second resistive layer. Similar zero crossover effects and frequency dependence TDEM transient responses have been observed and discussed elsewhere [94,95]. By mathematical analysis, it has been shown that the sign reversals may appear in magnetometric vertical-component in-loop TDEM

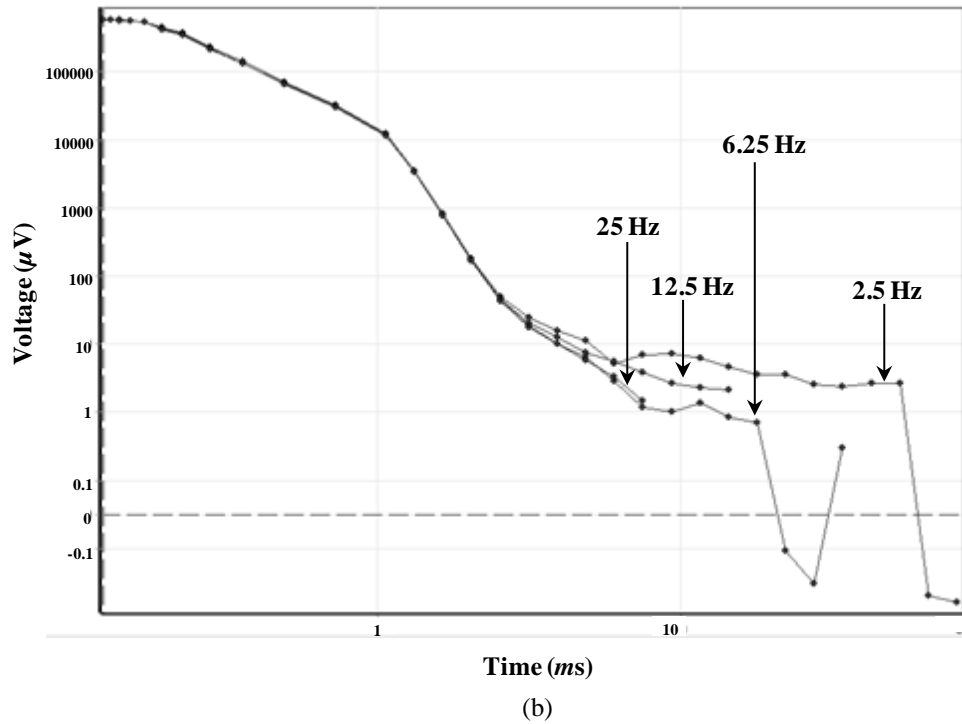
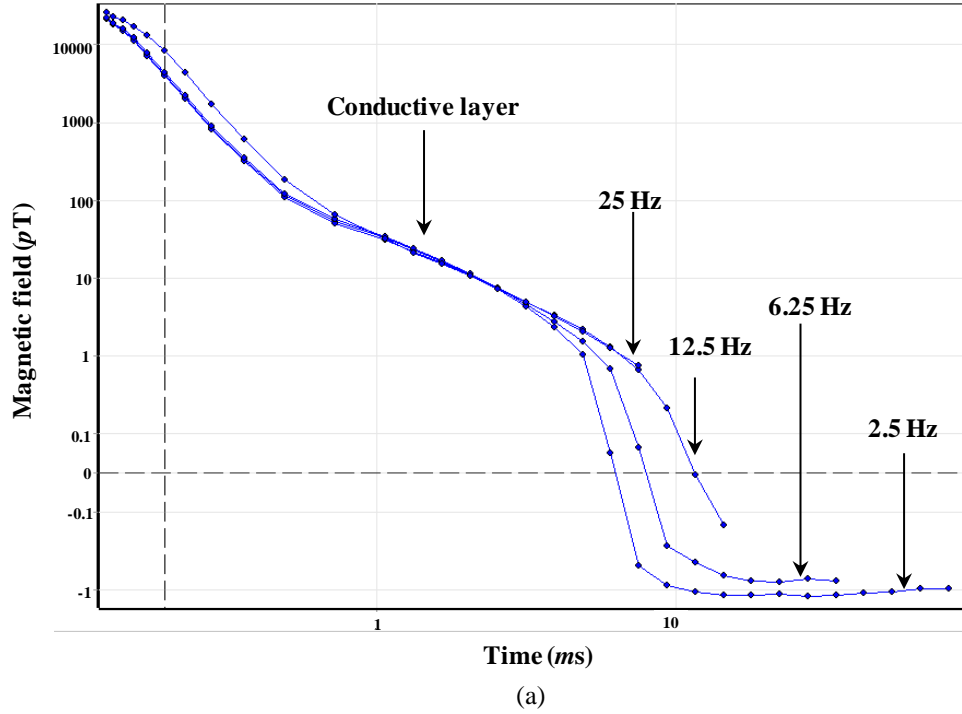


Fig 3.16 The decay of the secondary magnetic field (log-log scale) recorded by (a) SQUID and (b) induction coil with different base frequencies for transmitter loop of side length 400 m with applied current of 27 A.

measurements for such kind of resistive targets followed by a conductive basement. In case of [94], the response signal recorded by the SQUID magnetometer decays more rapidly for higher frequencies of the transmitter current. But, in the present study, it is entirely opposite, that is, the response signal decays more rapidly for lower frequencies of the transmitter current. Nevertheless, while analyzing the raw data, substantial instrumental drift from higher value towards a lower value was observed. Hence, it is likely predicted that the zero crossover effects may be due to the long drift which is reflecting in the TDEM measurements with respect to the base frequency of the transmitter current (high base frequency corresponds to short recording time for the fixed number of stacks).

Similarly, the decay of the secondary magnetic field recorded by the SQUID and induction coil with different base frequencies for the transmitter loop size of 400 m x 400 m are shown in Fig 3.16 (a) and (b) respectively. In case of Fig 3.16 (a), the response of the ground recorded by the SQUID with transmitter loop size of 400 m x 400 m and with transmitter current of 27 A show excellent resolution of the conductive layer as compared to the transmitter loop size of 100 m x 100 m with transmitter current of 25 A. Similarly, the resolution of the conductive target with an induction coil is also improved as compared to the smaller size of the transmitter loop but overall the performance of the induction coil is poor as compared to the SQUID. Therefore, the experimental results showed that the depth resolution of the conductive target mainly depends on the sensitivity of the receiver and the transmitter moment.

3.4.4. Modeling and estimation of the depth of conducting layer

An approximate depth of conductive layer has been estimated by using a Maxwell plate model whose response to the applied magnetic field matches with the response obtained from experimental data. A conductive thin plate (P1) is used to simulate the overburden

response at early times while another conductive plate (P2) was used to simulate the response due to buried conductive target (refer Fig 3.17).

Assuming the buried conducting target to be the shale layer mentioned in literature that describe the stratigraphy of the terrain, the depth of the center of the corresponding plate P2 was kept constant at 300 m

while the other parameters were varied by a trial-and-error method to find values that were needed in order

to reach a reasonable fit to the experimental data. The decay response from both simulated and experimental data is shown in Fig 3.18. The best fit was obtained for the plate P2 with

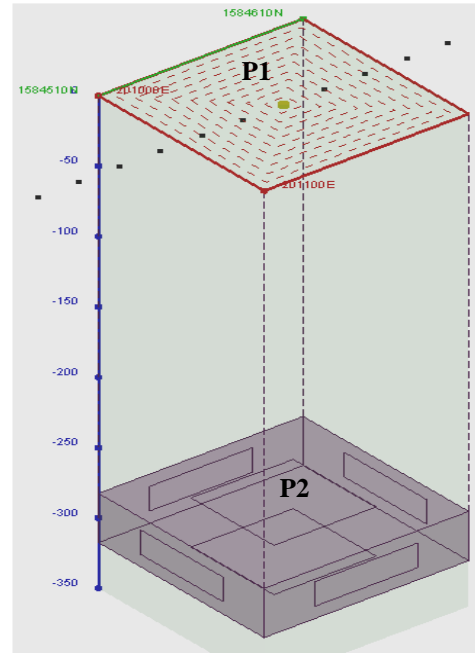


Fig 3.17 Layered model showing top plate P1 (conductive overburden) and bottom plate P2 (buried target layer) at depth of 285m.

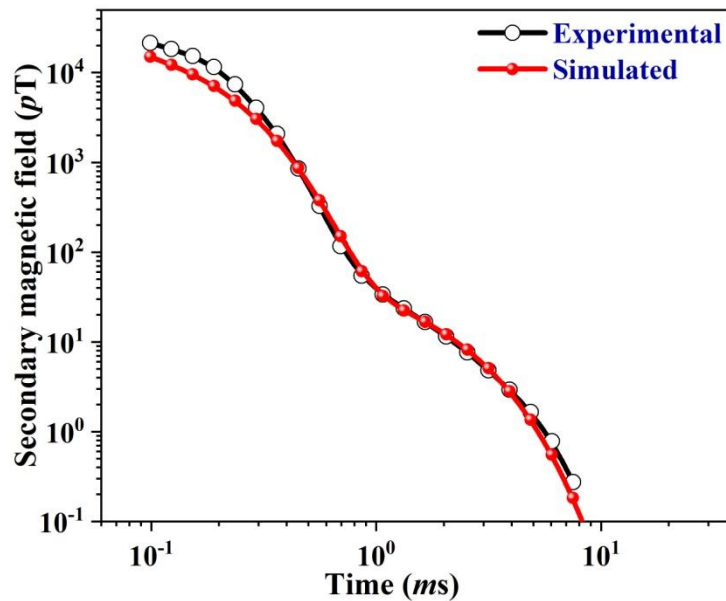


Fig 3.18 Vertical magnetic field decay response showing in log-log scales for simulated and experimental data.

thickness of 35 m and conductivity ~ 170 mS/m. The conductivity of shale ranges from 33 mS/m to 200 mS/m [96]. Therefore, it can be concluded that this layer of shale could be successfully detected using the SQUID sensor in central loop TDEM configuration.

3.5. Conclusion

Detection of thin conducting layer in a region with thick high conductivity overburden is highly challenging using TDEM central loop sounding measurements with an induction coil as receiver. Similarly, detection of thin conducting layer covered with a thick and highly resistive surface is equally challenging due to the induction of weak eddy currents in the resistive layer. Larger transmitter moments and sensitive magnetometer such as SQUID are important to achieve greater depths of investigation. In view of this, a SQUID based TDEM system has been developed and utilized in a terrain where a thin conductive layer is buried under a thick resistive layer (resistive overburden). Initially, the system has been tested with smaller transmitter loop (2 m x 2 m) and aluminum plates as targets and the experimental results have been described in chapter 2. Subsequently, the system has been further tested at the same location (site 1 as mentioned in section 3.3) with a transmitter loop size of 100 m x 100 m and current of 25 A. Here, the measurements were performed at different base frequencies and the results showed possible presence of highly conductive layer at shallow depths.

Simulations using Maxwell electromagnetic imaging software have been performed in order to compare the effect of various transmitter parameter values on investigation depth of the target. The simulation results showed that increasing the area of the transmitter loop enhanced the time of response of the signature of a buried conductive target.

Finally, the SQUID based system has been used to perform central loop TDEM sounding measurements in such a terrain where a thin conducting layer is covered with thick resistive layer. The measurements were performed with transmitter loop sizes of 100 m x

100 m and 400 m x 400 m. The use of larger transmitter loop showed better resolution for the conducting target buried in deeper layers of the earth as compared to the smaller one. While repeating the measurements with an induction coil, it was observed that SQUID shows better target resolution as compared to the induction coil. Further, the fluxgate magnetometer showed that the decay transients reached negative values at earlier times. This anomalous behavior of the fluxgate was further studied in detail and presented in Chapter 4. Simulations with Maxwell forward models were also performed in order to verify the experimental results obtained using the SQUID based system and the presence of a thin conductive layer at a depth of about 300 m was confirmed.

The results obtained from the central loop TDEM measurements done with SQUID system showed that SQUID is the best magnetic eye to visualize the conducting object located far below the earth surface.

Chapter 4

DUAL BEHAVIOR OF THE FLUXGATE MAGNETOMETER IN TDEM GEOPHYSICAL MEASUREMENTS

This chapter provides (1) brief introduction to prototype tests of the TDEM system using different sensors; (2) a preliminary observation of dual behavior of fluxgate; (3) a comparison of experimental results obtained during TDEM tests using fluxgate and SQUID; (4) explanation for negative response of fluxgate in TDEM measurements; (5) details of TDEM measurements in field using larger transmitter loops; (6) details of laboratory simulation experiments to confirm dual behavior of fluxgate; and (7) results of the experiments showing additional voltage generation.

4.1. Introduction

It is well known that conventionally an induction coil whose output voltage is proportional to the rate of change of magnetic field and fluxgate magnetometer whose output voltage is proportional to magnetic field are used as receiver to sense the decay of the secondary magnetic field in geophysical transient electromagnetic measurements. In recent times, an extremely high sensitive superconductivity based magnetic field sensor SQUID is being used as receiver. Fluxgates have proven to be useful in TDEM measurements in highly conductive terrain such as those in copper-nickel mining areas as they show good lateral resolution at later times compared to induction coils [97]. However, comparative studies on both the fluxgate as well as SQUID have shown that advantage of utilizing a commercial fluxgate magnetometer for TDEM measurement is limited by its bandwidth and sensitivity [98].

As part of the SQUID based TDEM system developmental work, we have tested our system with an induction coil, fluxgate magnetometer and SQUID magnetometer. During

performance testing of TDEM central loop sounding measurements, the dual behavior (combination of an induction coil and magnetometer) of the fluxgate sensor has been accidentally observed. The dual behavior has only been observed at early decay time of the secondary magnetic field. At the same time, such dual behavior has not been observed to a considerable extent in transient eddy current NDE measurements. In NDE, since the applied excitation field is high and the targets are always metal plates, the expected response of the measurement occurs at later time. Moreover, the eddy current change in the conducting material with respect to time is small and hence the part of the voltage induced due to the behavior of an induction coil is negligible as compared to the voltage produced due to the behavior of the magnetometer. This chapter describes the observations of the dual behavior of the fluxgate magnetometer in TDEM geophysical measurements. The reasons for the behavior have been examined through the interpretation of the data recorded from the TDEM central loop sounding measurements and simulation experiments performed at our laboratory.

4.2. Preliminary observation of the dual behavior of the fluxgate magnetometer

Since the TDEM survey with low T_c SQUID system involves handling of liquid helium in a remote testing site located far away from our laboratory and with no prior survey experience with larger transmitter loops, we decided to perform TDEM field survey measurements in order to familiarize with field survey experience. In view of this, we chose fluxgate magnetometer as a receiver and transmitter loop in the form of square with side length of 100 m. It was noticed that the decay of magnetic field unexpectedly reached negative value even at the earlier time windows. We have chosen a site for this test survey with its known lithological structure (like conductivity of the Earth as a function of depth) near Kotala village, Andhra Pradesh (AP). This is the same location where we have

performed SQUID based TDEM measurements later. The nature of the terrain is a thin conducting layer (10 to 15 m) covered with a thick resistive layer (300 to 350 m) and the detailed structure of the terrain has been described in chapter 3. In this work, trapezoidal current pulse of 25 A with base frequency of 2.5 Hz was passed through the transmitter loop (100 x 100 m) using the transmitter. The output of the fluxgate was connected to the SMARTem24 data acquisition system which was accurately synchronized with the transmitter through the transmitter controller. The recorded secondary magnetic field was processed to display the decay transients. During these measurements, it was found that the secondary magnetic field always decays very fast at earlier time and sometimes it reaches negative values (Fig 4.1), and it was inferred that this was due to induced polarization effect (IP). But it is well known that the IP effect occurs at later time. Hence, it was suspected that the fluxgate behaves like an induction coil at early times (high frequency region) and magnetometer at later time (low frequency region).

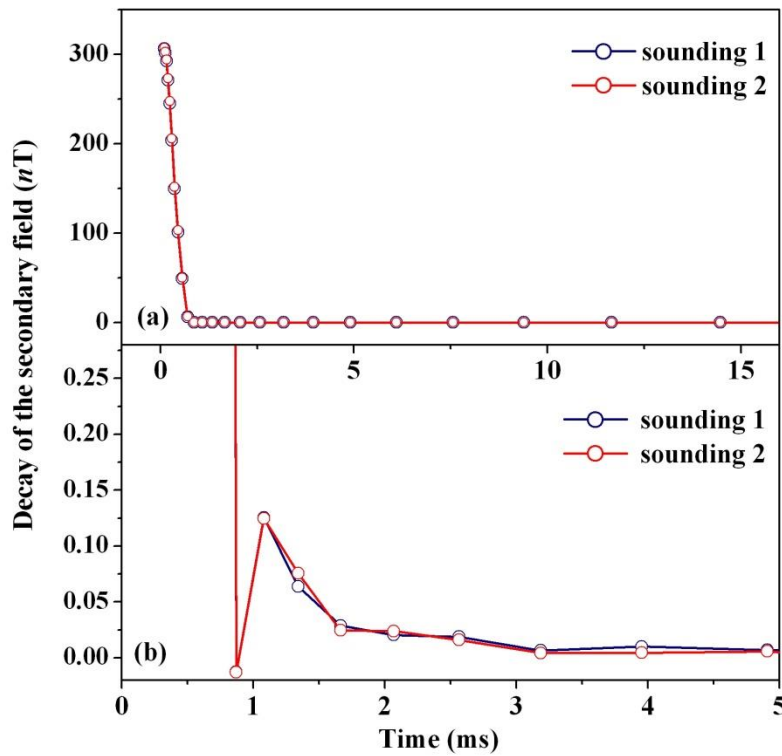


Fig 4.1 (a) Decay of the secondary magnetic field for the central loop sounding measurements with fluxgate as a receiver (b) Enlarged view at the earlier time.

It is also known that the bandwidth of the fluxgate sensor is about 3 kHz at 3 dB. If this was due to the bandwidth limitation, the initial amplitude just after the decay of the secondary magnetic field may come down but it should never reach negative. In view of this, TDEM measurements have been repeated with fluxgate as receiver and by maintaining the experimental configuration same as done in the past for testing and characterizing the SQUID system using the same aluminum plates as targets. The experimental results obtained with fluxgate as receiver have been compared with the results obtained with SQUID as receiver. The experimental setup with portable transmitter

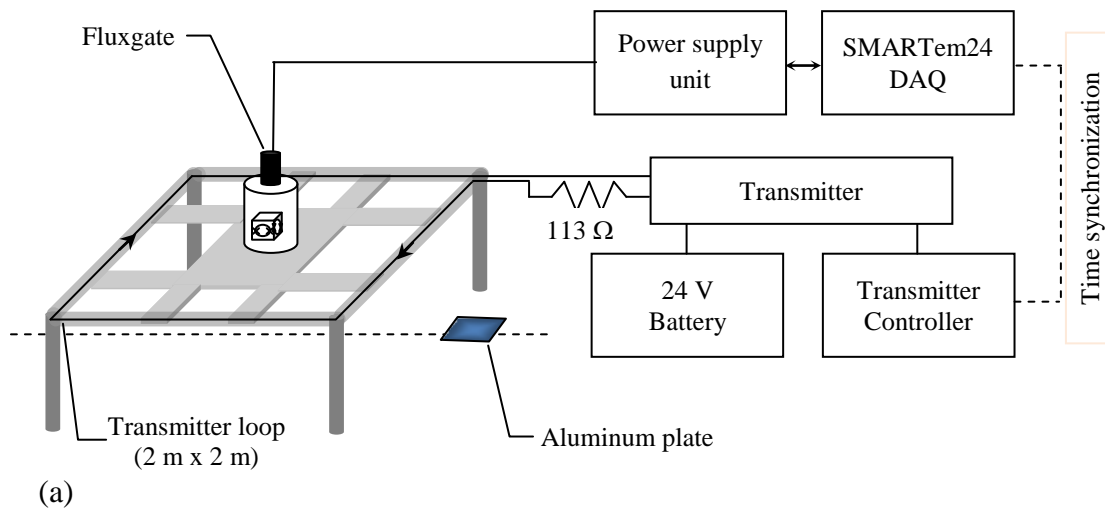


Fig 4.2 (a) Schematic diagram of the TDEM system with fluxgate receiver and transmitter loop of 2 m x 2 m and (b) Photograph of the TDEM system with fluxgate.

loop in the form of square with side length of 2 m and the experimental procedures have been described in detail in Chapter 2. For the sake of completeness, the schematic diagram and photograph of the TDEM system with fluxgate and a transmitter loop of 2 m x 2 m is shown in Fig 4.2. In the following section, the experimental results and their analysis have been presented in order to show the dual behavior of the fluxgate; that is, the combination of magnetic field sensor and induction coil at earlier decay times and magnetic field sensor only at later decay times.

An aluminum plate of size 300 mm x 200 mm x 2 mm was scanned under the fluxgate at a depth of 0.5 m below the transmitter loop with a scanning length and step size of 4 m and 50 mm respectively. The raw data was recorded at every location for a period of 51.2 seconds (128 stacks) and number of decay profiles were stacked and averaged to display the final decay plots. The TDEM measurements were also repeated for plate thicknesses of 4 mm and 6 mm by maintaining the same length and breadth of the aluminum plate.

4.3. Comparison of TDEM experimental results performed with portable transmitter by using fluxgate and SQUID as receivers

The experimental data recorded earlier using SQUID has been presented here for comparison with the data recorded using the fluxgate. Fig 4.3 shows the decay of the vertical component of secondary magnetic field recorded by the SMARTem24 with SQUID as a receiver as the aluminum plates approach SQUID system. Fig 4.3 (a), (b), and (c) are the entire decay profiles for the plate thicknesses of 2 mm, 4 mm and 6 mm respectively and (d), (e), and (f) are the corresponding enlarged view of the decay profile where the variation in signal strength is larger. Here, the initial value of the secondary magnetic field recorded by the SQUID system just after switching off the current in the transmitter loop is almost same and is equal to the calculated value of the magnetic field at the center of square loop. From Fig 4.3 (d), it is clear that the strength of the induced eddy

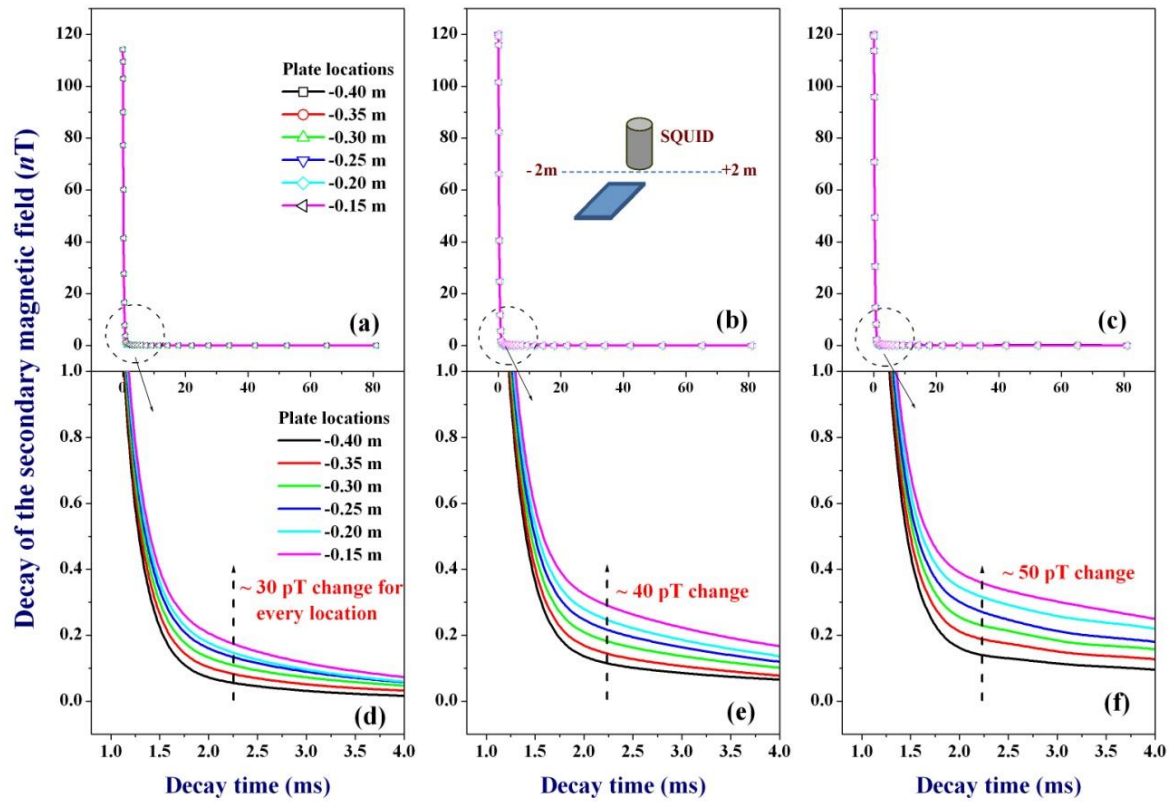


Fig 4.3 The decay of the secondary magnetic field recorded by the SMARTem24 with SQUID as a receiver when the aluminum plate approaches SQUID system. (a), (b) and (c) are the entire decay profiles for the plate thicknesses of 2 mm, 4 mm and 6 mm respectively and (d), (e) and (f) are the corresponding enlarged view of the decay profile where the signal change occurred at larger value.

current in the plate increases and it takes longer time to decay as it approaches the SQUID system. In the same way, the strength of the induced eddy current increases with the increase of plate thickness and are shown in Fig 4.3 (e) and (f). Similarly, the change of the secondary magnetic field with positional scan coordinates for the aluminum plates with thickness of 2 mm, 4 mm, and 6 mm at different time gates is shown in Fig 4.4 (a), (b) and (c) respectively. In the decay profile recorded at each location or in the entire profile data, the output of the SQUID sensor never reached negative values except the noise fluctuations occurring at later times.

The decay of the secondary magnetic field recorded by the SMARTem24 with fluxgate as a receiver as the aluminum plates approach the fluxgate is shown in Fig 4.5. Fig 4.5 (a),

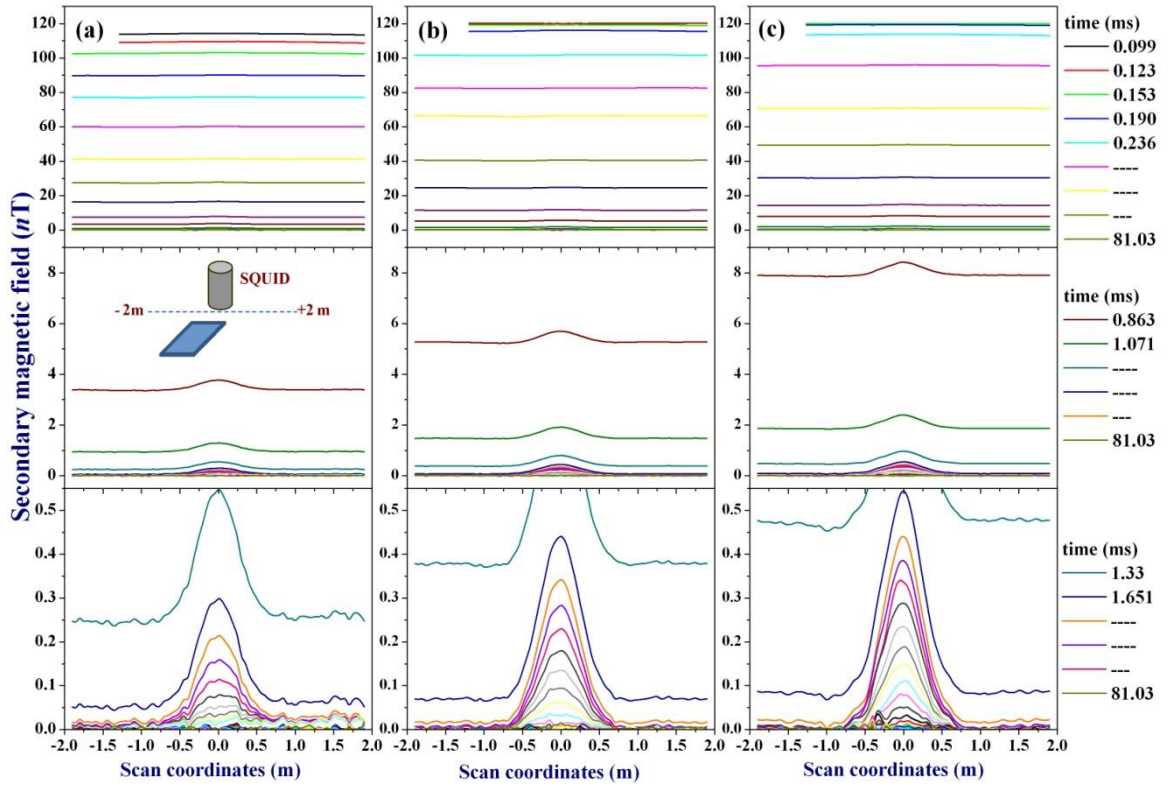


Fig 4.4 Change of the secondary magnetic field recorded by the SQUID with positional scan coordinates for the aluminum plates with a thickness of (a) 2 mm, (b) 4 mm and (c) 6 mm at different time gates (From top to bottom - early, intermediate and late time gates).

(b) and (c) are the entire decay profiles for the plate thicknesses of 2 mm, 4 mm, and 6 mm respectively and (d), (e) and (f) are the corresponding enlarged view of the decay profile where variation in signal strength is larger. Therein, the initial value of the secondary magnetic field recorded by the fluxgate just after switching off the current in the transmitter loop is about 38 nT which is almost one third of the calculated value of the magnetic field at the center of square loop. The subsequent decay of the secondary magnetic field reaches negative value, again increasing to positive and further decaying to zero. Initially, it was assumed that the decay of the secondary magnetic field at earlier time consists of high frequency components and the bandwidth of the fluxgate was insufficient to track. At the same time, the decay of the secondary magnetic field reaches negative value, which is not due to bandwidth limitation of the fluxgate. Further, TDEM

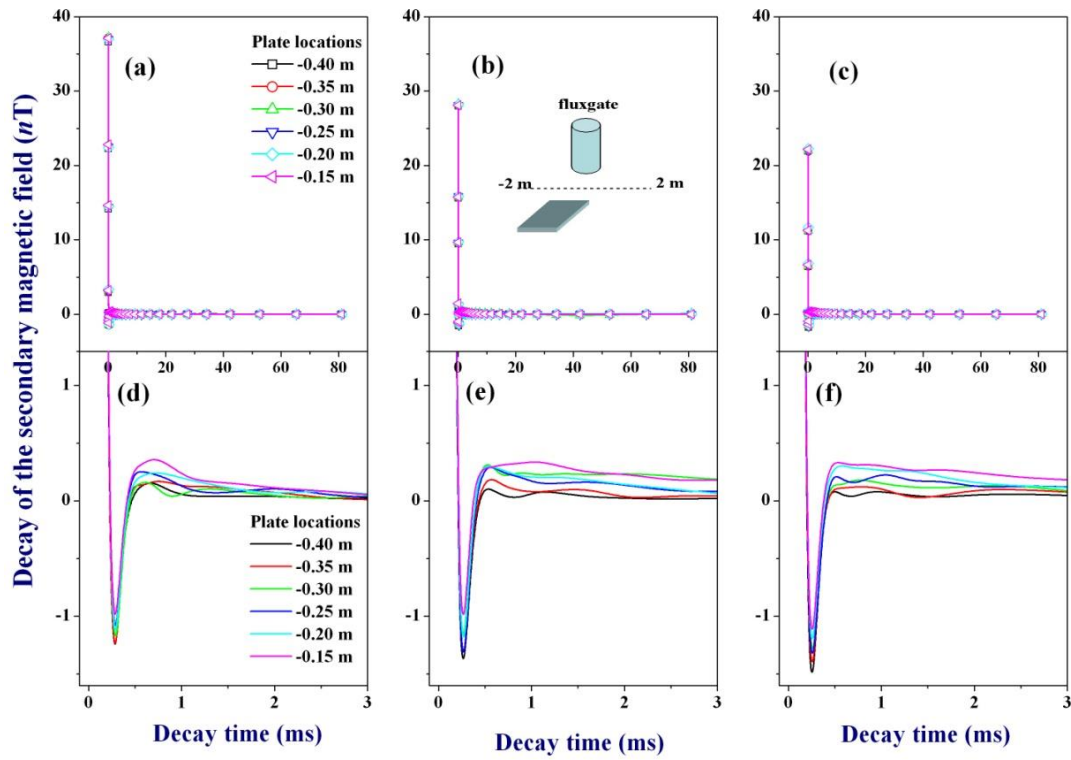


Fig 4.5 The decay of the secondary magnetic field recorded by the SMARTem24 with fluxgate as a receiver when the aluminum plate approaches fluxgate. (a), (b) and (c) are the entire decay profiles for the plate thicknesses of 2 mm, 4 mm and 6 mm respectively and (d), (e) and (f) are the corresponding enlarged view of the decay profile where the signal change occurred at larger value.

measurements with plate thicknesses of 4 mm and 6 mm confirmed that the decay of the secondary magnetic field recorded by the fluxgate is due to change of $(\partial B/\partial t)$ at earlier time and change of B at later time. At earlier time, the change of the secondary magnetic field is smaller as the thickness of plate increases to 4 mm and 6 mm (conductivity increase) and the corresponding output voltages are reduced to values of 28 nT and 21 nT, respectively. Similarly, the change of the secondary magnetic field recorded by the fluxgate with positional scan coordinates for the aluminum plates with thickness of 2 mm, 4 mm and 6 mm at different time gates is shown in Fig 4.6 (a), (b) and (c) respectively. The changes of the secondary field decreases at earlier time gates and reaches negative value and it increases at later time gates in spite of the poor sensitivity of the fluxgate sensor.

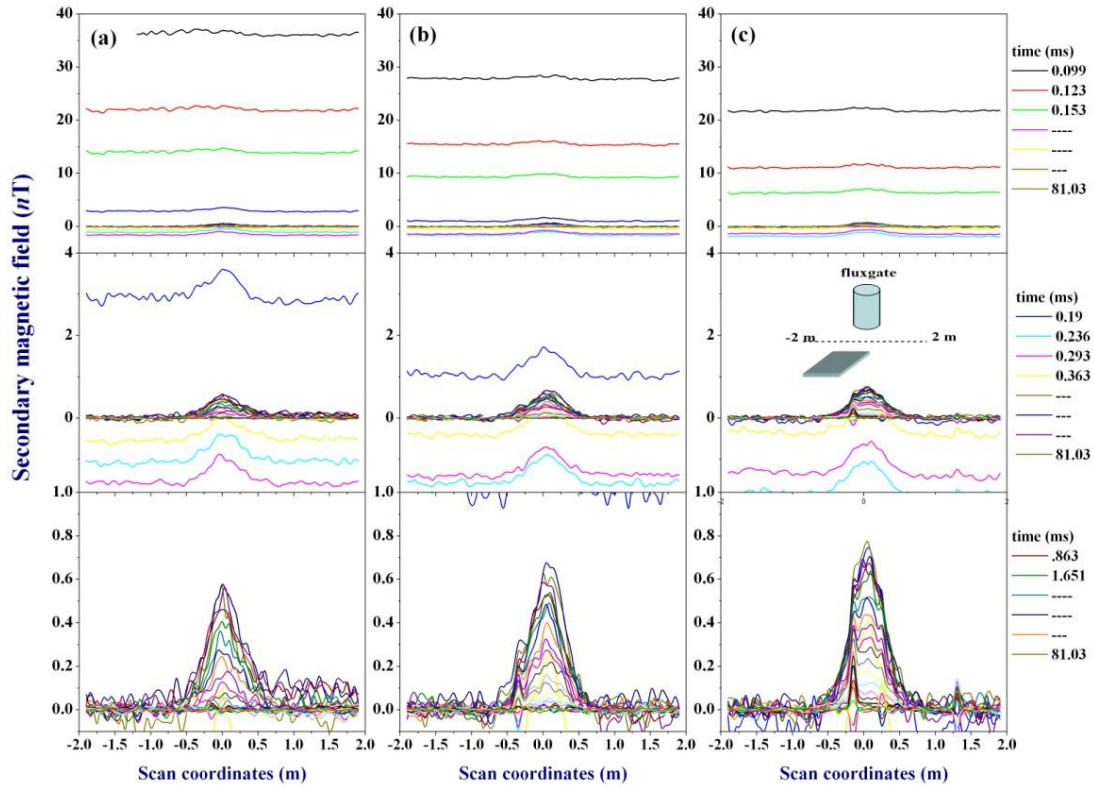


Fig 4.6 Change of the secondary magnetic field recorded by the fluxgate with positional scan coordinates for the aluminum plates with a thickness of (a) 2 mm, (b) 4 mm and (c) 6 mm at different time gates (From top to bottom - early, intermediate and late time gates).

The TDEM measurements were further extended by increasing the current transmitted through the transmitter loop from 0.212 mA to 2 A. Here, the strength of the induced eddy current increases with better signal to noise ratio as compared to the lower transmitter current. At the same time the decay of the secondary field reaches negative value extending to the later time gates as compared to the lower transmitter current and shown in Fig 4.7.

The experimental results have clearly shown that the SQUID magnetometer behaves as a pure magnetic field sensor from earlier time gates to late time gates. To the contrary, the fluxgate magnetometer works as an induction coil at early time gates and as magnetometer at later time gates.

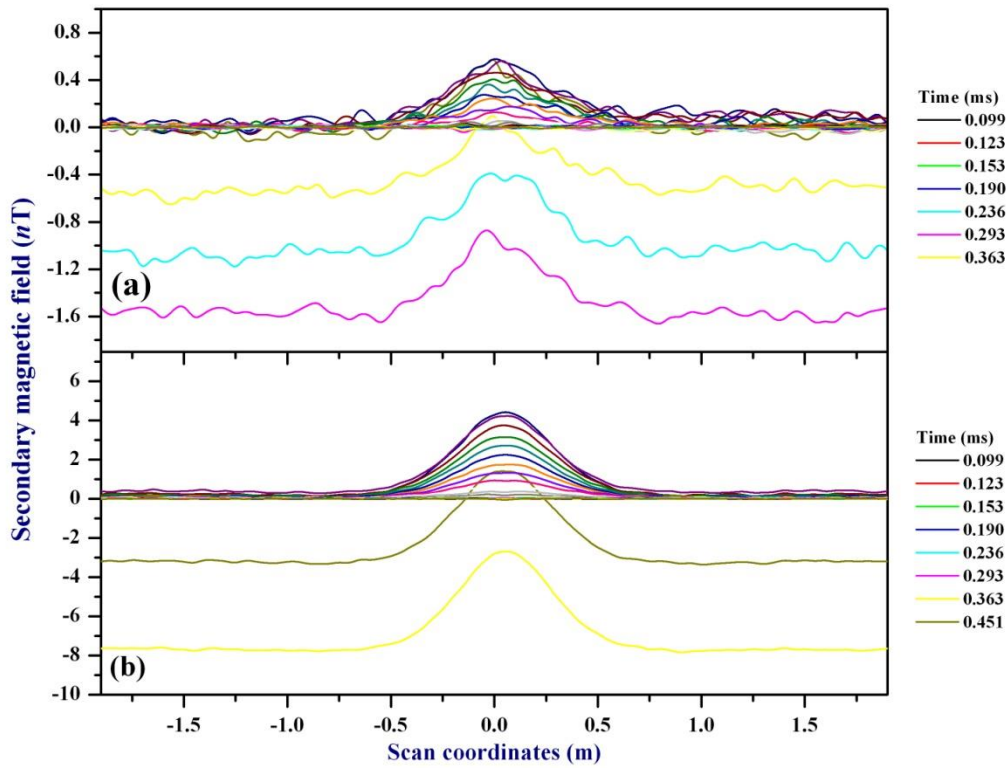


Fig 4.7 Change of the secondary magnetic field recorded by the fluxgate with positional scan coordinates for the aluminum plates with a thickness of 2 mm and transmitter current of (a) 0.212 A (b) 2 A at different time gates.

4.4. Explanation for the negative response of the fluxgate in TDEM measurements with typical TDEM output waveforms for an induction coil and magnetometer

The reason for the decay of the secondary magnetic field reaching negative values at early time can be explained by using TDEM output waveforms recorded with magnetometer and an induction coil. It is well known that the working principle of the TDEM technique is the induction of eddy currents in the ground with suitable transmitter and detection of the decay of the induced eddy current with respect to time with a suitable receiver. The working principle of the TDEM technique has been described in detail in Chapter 2. In addition, the dual behavior of the fluxgate magnetometer, the working principle of the TDEM technique and its data processing have also been briefly explained

here along with its output responses measured by magnetometer and an induction coil for a given input transmitter waveform.

The current in the form of trapezoidal pulses is applied to the transmitter loop and the response of the ground is measured by the magnetometer and/or induction coil as shown systematically in Fig 4.8. The recorded raw data with time is further processed in order to obtain the decay profile. The typical central loop configuration and the current pulse applied to the transmitter loop are shown in Fig 4.8 (a). In general, TDEM measurement is made continuously and the data recorded during OFF time is extracted for further processing because of the absence of the primary magnetic field during OFF time. In order to eliminate the noise due to the electrical power line (power line frequency of 50 Hz) and

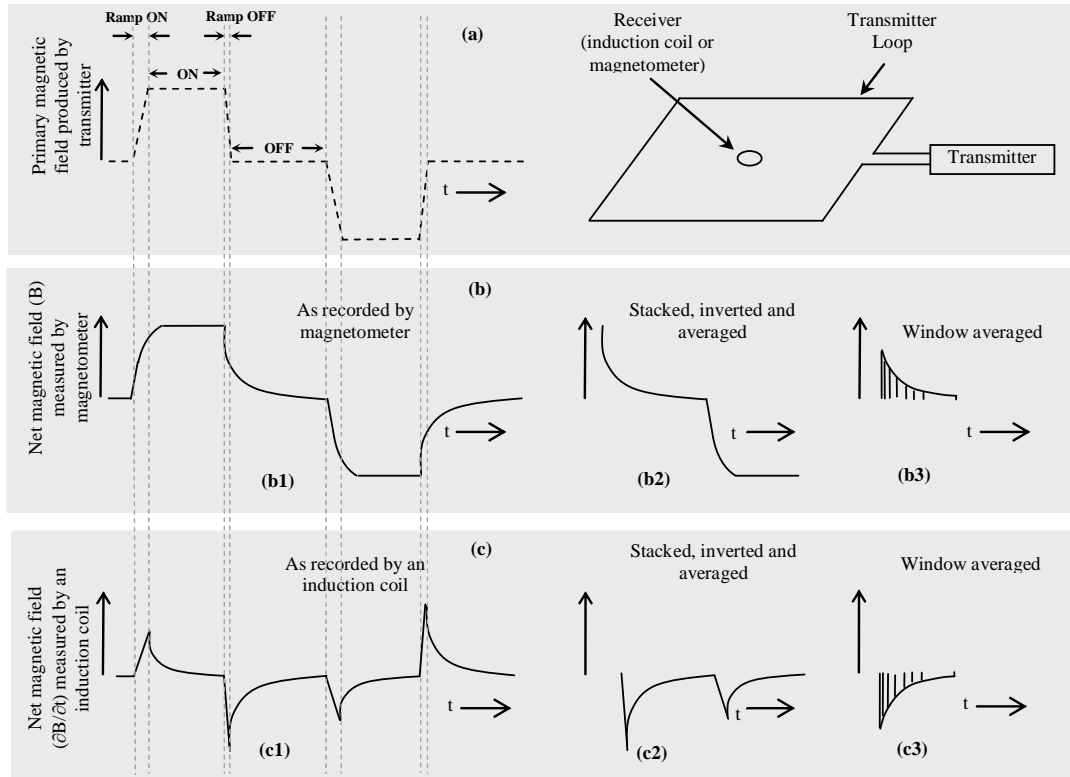


Fig 4.8 Schematic view of the TDEM waveforms (a) Typical shape of the current pulse applied to the transmitter loop (left) and typical TDEM central loop configuration, (b) Net magnetic field measured by the magnetometer and data processing [(b1) raw data , (b2) stacked and averaged with suitable inversion and (b3) final window averaged)] and (c) Net magnetic field measured by an induction coil and data processing [(c1) raw data , (c2) stacked and averaged with suitable inversion and (c3) final window averaged)].

to reduce the instrumental drift, the applied current to the transmitter loop is also reversed.

In addition to this, to suppress the uncorrelated background noise the data has to be stacked over a long period of time and averaged. The raw data recorded for one cycle is shown in Fig 4.8 (b1). The electrical power line noise can be suppressed by inverting the data recorded during OFF time of the negative half cycle and averaging with the data recorded during OFF time of the positive half cycles (Fig 4.8 (b2)).

In a similar manner, the recorded and processed TDEM waveforms with an induction coil are shown in Fig 4.8 (c). The raw data recorded using an induction coil, averaged after

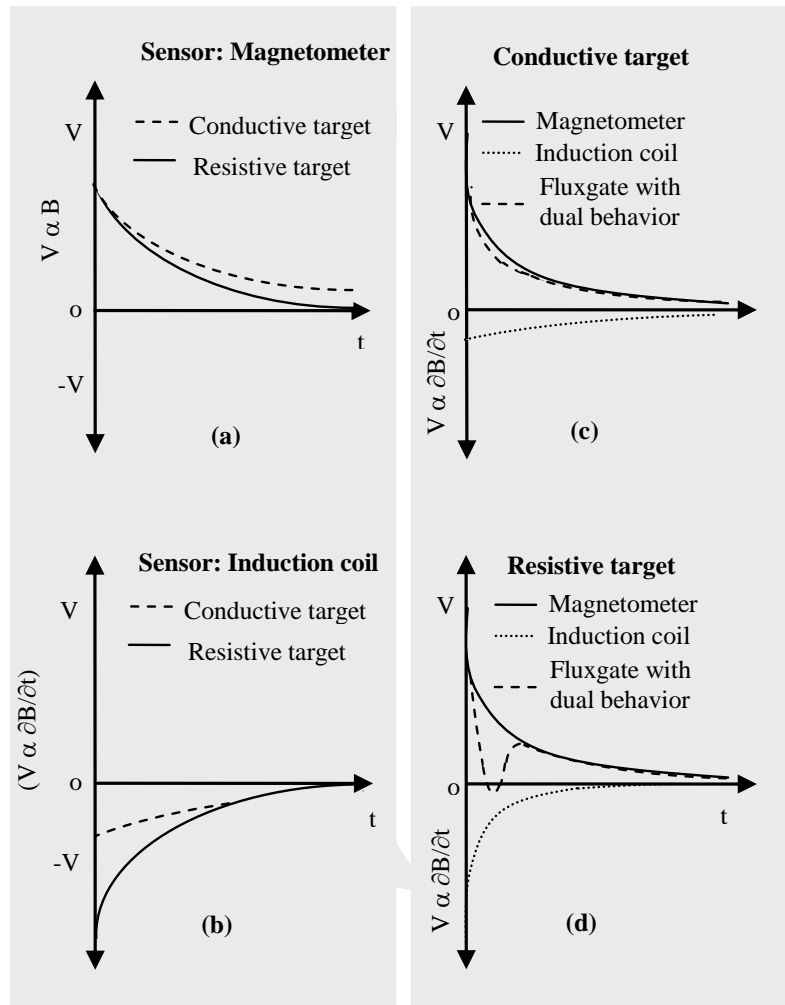


Fig 4.9 The schematic representation of the decay profiles for different targets with different sensors (magnetometer and an induction coil) in TDEM measurements. (a) and (b) are the decay profiles of the conductive and resistive targets measured with magnetometer and induction coil respectively and (c) and (d) are the decay profiles measured with the fluxgate sensor which behaves like a combination of both magnetometer and an induction coil for the conductive and resistive targets respectively.

stacking and window averaging are shown in Fig 4.8 (c1), (c2) and (c3) respectively. In practice, for interpretation of the geophysical TDEM data recorded using the induction coil, the decay plots can be inverted or the polarity of the current leads of the transmitter loop can be changed.

The decay of the secondary magnetic field at earlier time has high frequency components and vice versa. Here, we propose that fluxgate magnetometer behaves like an induction coil during the decay of the secondary magnetic field in a short interval, particularly at earlier time. Therefore, the decay of the secondary magnetic field goes to a negative value in TDEM central loop sounding measurements. In addition to this, the effect of the dual behavior of the fluxgate strongly depends on the nature of the terrain. The schematic representation of the decay profiles for different targets with different sensors (magnetometer and an induction coil) in TDEM measurements have been shown in Fig 4.9 in order to indicate the dual behavior of the fluxgate in different targets. The induced eddy current in the resistive target and its associated secondary magnetic field decays rapidly and the corresponding output voltage recorded by the magnetometer and induction coil are shown in Fig 4.9 (a) and (b) (solid lines). Similarly, the persistence of the eddy current due to the conducting target results in slow decay which reflects in the magnetometer and the induction coil sensors (dashed line in Fig 4.9 (a) and (b)). It is obvious that, if the fluxgate sensor behaves like a combination of an induction coil and magnetometer, then the net output voltage of the fluxgate magnetometer is the summation of the two components (voltage is proportional to the magnetic field and rate of change of magnetic field) and is strongly dependent on the nature of the target. Therefore, with fluxgate measurements, the response of the induction coil behavior is negligibly small for the conductive target as compared to the resistive target. The schematic view of decay profiles with the use of fluxgate sensor for the conductive and resistive target is shown in Fig 4.9 (c) and (d)

respectively. In addition to this, the dual behavior of the fluxgate is observed only at earlier time and the reasons for the same have been explained in detail in later sections.

4.5. TDEM measurements in the field with larger transmitter loops

TDEM central loop sounding measurements have been carried out in the field with larger transmitter moments. Experiments have been carried out using both magnetometers (fluxgate and SQUID) and the remaining experimental configurations are identical. The location of the terrain is same where we have performed TDEM measurements with fluxgate earlier. The nature of the terrain is layered structured where a conducting layer is covered with thick highly resistive overburden. The performance of the

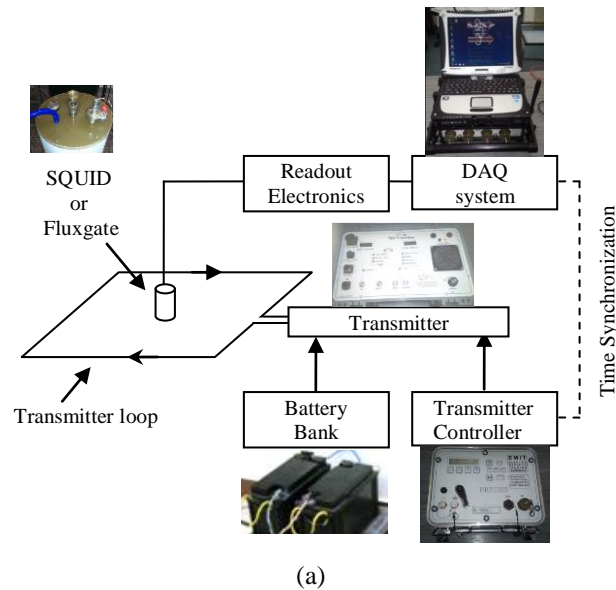


Fig 4.10 (a) Schematic diagram of the TDEM system. (b) Photograph of the setup with SQUID and (c) fluxgate in the field.

fluxgate has been compared with the central loop sounding measurements carried out by using SQUID sensor. The experimental results have also shown that at earlier times, the decay of the secondary magnetic field recorded by the fluxgate magnetometer behave like that recorded by an induction coil but the same has not been observed with SQUID magnetometer.

Table 4.1 Transmitter loop parameters in TDEM measurements

| Transmitter loop | Transmitter loop size (m) | Transmitter current (A) | Central magnetic field (nT) |
|------------------|---------------------------|-------------------------|-----------------------------|
| Loop A | 100 x 100 | 25 | 283 |
| Loop B | 400 x 400 | 27 | 81 |

In this region, central loop TDEM sounding measurements have been carried out with fluxgate sensor and transmitter loop sizes of 100 m x 100 m (loop A) and 400 m x 400 m (loop B). The sounding measurements have been repeated with SQUID sensor and the other parameters such as transmitter current, base frequency, etc., are maintained at same values. The transmitter loop parameters are listed in Table 4.1. The schematic diagram of the experimental setup and the photograph with SQUID and fluxgate are shown in Fig 4.10. Measurements have also been performed with different transmitter base frequencies and different number of stacking. Since the objective of this work is related to the dual behavior of the fluxgate sensor, the discussion has been limited to the data recorded for the transmitter base frequency of 25 Hz with the number of stacks of 1024.

The decay of the secondary magnetic field has been recorded by the fluxgate and SQUID with different transmitter loops and transmitter currents. Fig 4.11 (a) shows the decay profile recorded by the fluxgate with transmitter loop sizes of 100 m x 100 m (loop A) and 400 m x 400 m (loop B) and the transmitter currents of 25 A and 27 A respectively. The sounding measurements have been repeated with the same transmitter loops and currents using SQUID sensor and their decay profiles are shown in Fig 4.11 (b). The

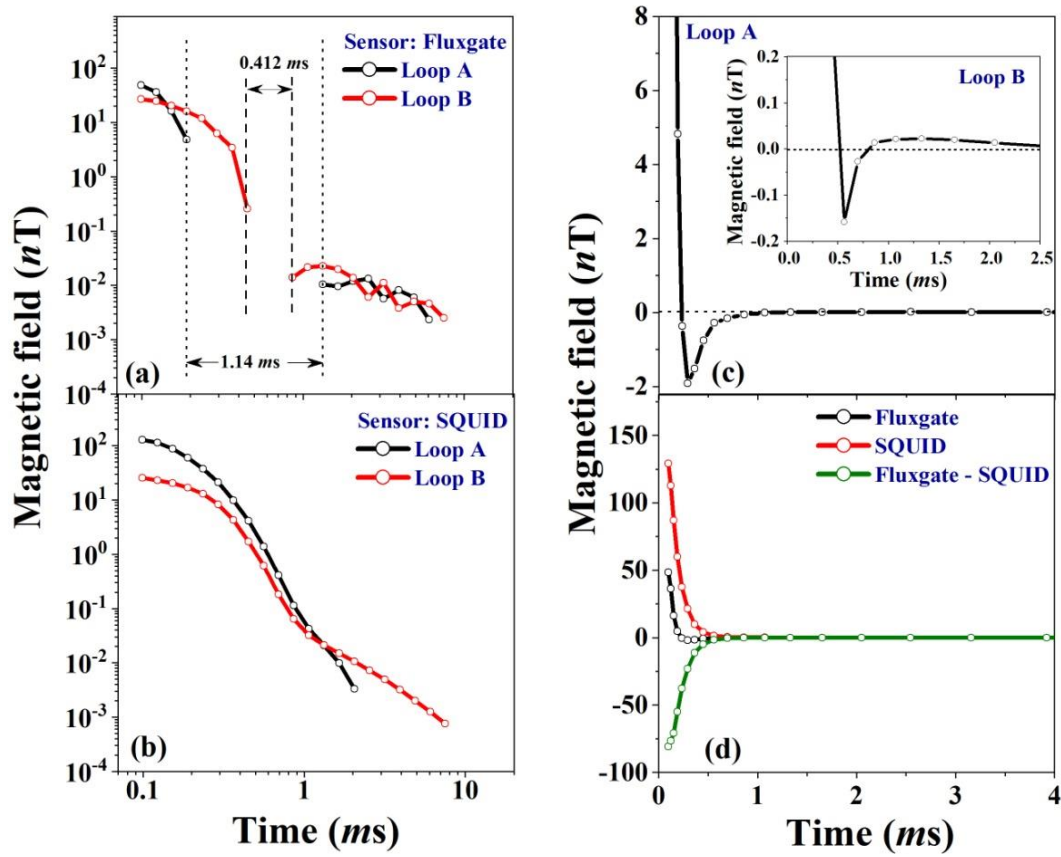


Fig 4.11 Decay profile recorded by the fluxgate and SQUID with different sizes of the transmitter loop and transmitter currents, (a) and (b) are log-log plots of the decay profile recorded by the Fluxgate and SQUID respectively, (c) and the inset of (c) are semi log plots of the decay profile (the region where the output of the fluxgate reaches to a negative value) recorded by the fluxgate with transmitter loop size of 100 m x 100 m and 400 m x 400 m respectively, (d) difference between field recorded using SQUID and fluxgate.

regions where the fluxgate output reaches negative values for the transmitter loops A and

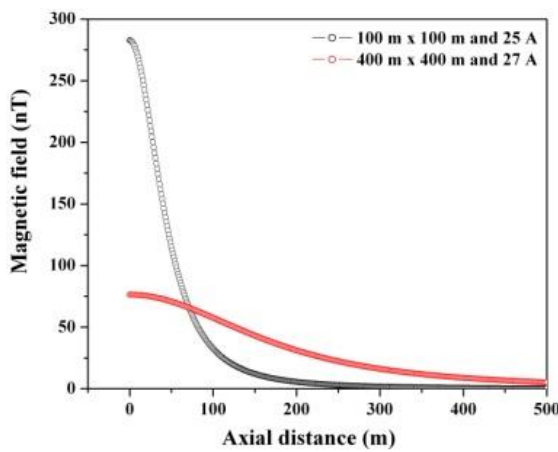


Fig 4.12 Primary magnetic field produced by the transmitter loop A and B along its axis.

B are also shown in Fig 4.11 (c).

The secondary magnetic field measured by the fluxgate with transmitter loop A reached negative values with a time window of 1.037 ms, whereas the same is 0.467 ms for the transmitter loop B. Similarly, the secondary magnetic field

reaches a negative value much earlier (0.293 ms) with a transmitter loop A as compared to the transmitter loop B (0.863 ms). In the present experiment, the central magnetic field produced by the transmitter loop A is 283 nT with the applied current of 25 A and the same is 81 nT with the applied current of 27 A for the transmitter loop B. The primary magnetic field produced by the transmitter loops A and B along their axes are shown in Fig 4.12. In loop A, the applied magnetic field is high and concentrated in the upper surface of the ground as compared to the transmitter loop B. Accordingly, the induced secondary magnetic field decays with time after the transmitter current is abruptly switched off and so does its associated voltage induced in the fluxgate (due to the induction coil behavior). In addition to this, in Fig 4.11 (d) the difference between the secondary magnetic field recorded by the SQUID and fluxgate clearly indicates the dual behavior of the fluxgate in TDEM measurements. The secondary magnetic field measured by the SQUID has not reached a negative value like the fluxgate and the presence of the conducting layer is clearly visible with larger transmitter loop (Fig 4.11 (b)) due to larger transmitter moment (moment of the transmitter loop B is $IA = 4.32 \times 10^6 \text{ Am}^2$) as compared to the smaller transmitter loop (moment of the transmitter loop A is $IA = 2.5 \times 10^5 \text{ Am}^2$).

4.6. Laboratory simulation experiments with fluxgate sensor for the confirmation of its dual behavior in TDEM measurements

Laboratory simulation experiments have been performed in order to identify the reason for the fluxgate's dual behavior when it is used for TDEM measurements. The fluxgate response has been recorded by applying sinusoidal input magnetic field with constant amplitude and changing the frequency range from DC to several kHz. The oscilloscope

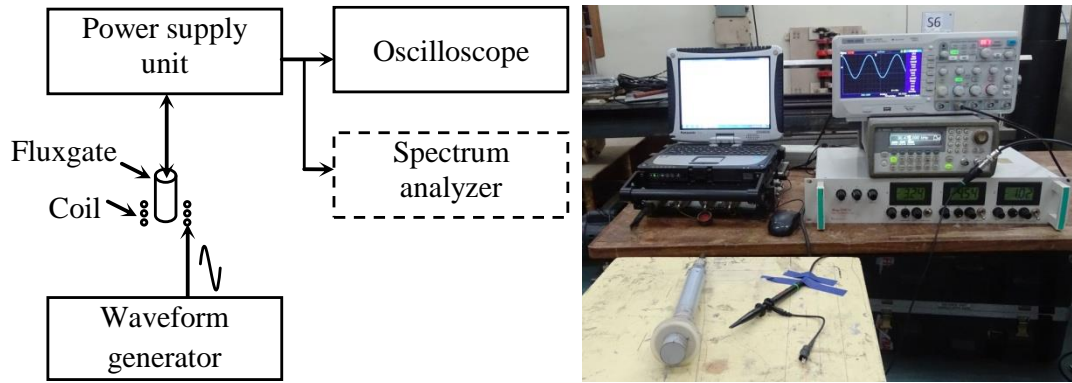


Fig 4.13 Schematic diagram and photograph of the experimental setup with fluxgate.

displays the output of the fluxgate and the peak to peak voltages have been measured. The schematic diagram and photograph of the experimental setup has been shown in Fig 4.13.

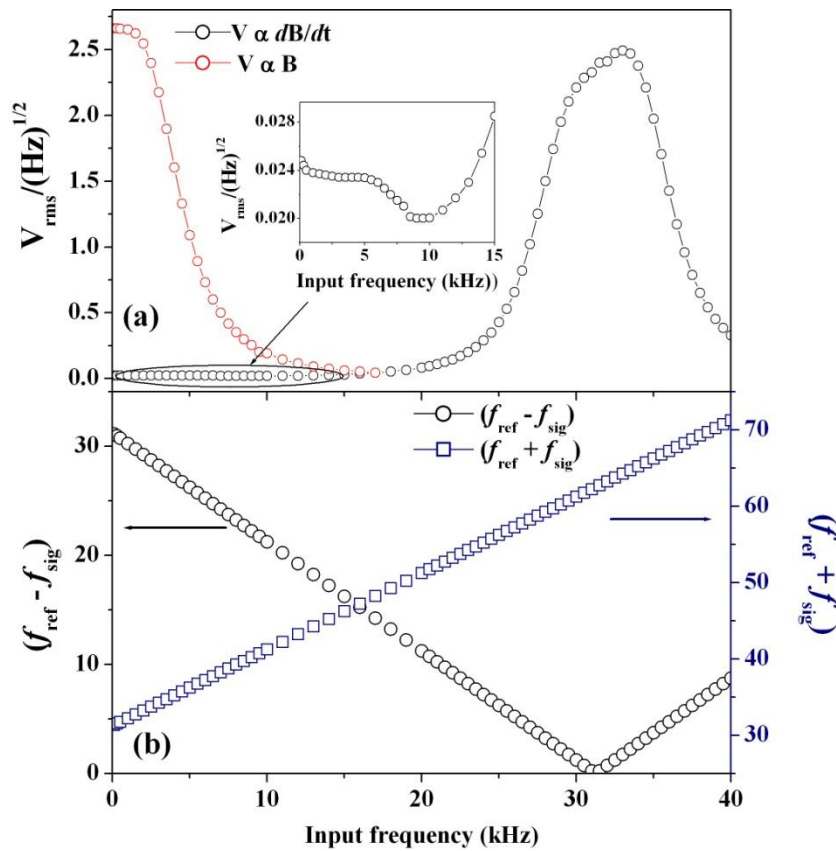


Fig 4.14 The predominant peak voltages and the corresponding frequencies measured at the output of the fluxgate for the input magnetic field with different frequencies. (a) The frequency of the voltage at the output of the fluxgate which is proportional to the input magnetic field is same as the input frequency of the magnetic field where as the frequency of the output voltage which is proportional to the rate of change of magnetic field is different from the input frequency. (b) The frequencies of the fluxgate output voltage ($f_{ref} - f_{sig}$) and ($f_{ref} + f_{sig}$) for the given input magnetic field at different frequencies.

Since the bandwidth of the fluxgate is 3 kHz at 3 dB, the amplitude of the fluxgate output is almost constant up to 0.8 kHz and its amplitude gradually decreases as we increase the input signal frequency further. From 10 to 15 kHz, there was no noticeable amplitude change but some sort of modulation signal has been observed. Above 15 kHz, the output amplitude gradually increased and reached maximum value at a frequency of 31.472 kHz and again decreased for further increase in input signal frequency. During this measurement, more importantly, we noticed that above 15 kHz the output voltage frequency of the fluxgate was not same as that of input signal frequency and the output voltage frequency was very low as compared to the input signal frequency. Subsequently, we repeated the same experiment by connecting a spectrum analyzer at the output of the fluxgate and the predominant peak voltage values and the corresponding frequencies have been recorded. The predominant voltage peaks and the corresponding frequencies measured at the output of the fluxgate for different input frequencies ranging from 0.1 kHz to 40 kHz are plotted and the same is shown in Fig 4.14 (a). We have observed a high frequency output signal with small amplitude along with the applied low frequency input signal. As we increased the input signal frequency, we found a systematic variation of output frequency and the fluxgate output voltage reached maximum value at the input frequency of 31.472 kHz. This is the reference frequency of the demodulator in the readout electronics of the fluxgate sensor which is exactly equal to twice the drive frequency used for permeability modulation in the fluxgate operation. Subsequently, we analyzed the operation of the fluxgate including its readout electronics and found the reason for the generation of the output voltage with different frequency along with the input signal frequency. Hence, it is essential to include the working principle of the fluxgate to understand the problem.

4.7. Additional voltage generation with different frequency at the output of the fluxgate

The working principle of the fluxgate sensor is based on the detection of second harmonics of the driving signal. The schematic diagram of the fluxgate with its readout electronics are shown in Fig 4.15. Fluxgate comprises of a driving coil wound over the core in the form of differential configuration, a pick-up coil and a feedback coil. Here, the core permeability is modulated by applying high frequency alternating magnetic field to the driving coil whose amplitude is just above the saturation of the core. The external magnetic field which is to be measured makes a shift in the B-H curve of the core and the corresponding voltage induced in the pickup loop will have a second harmonic of the

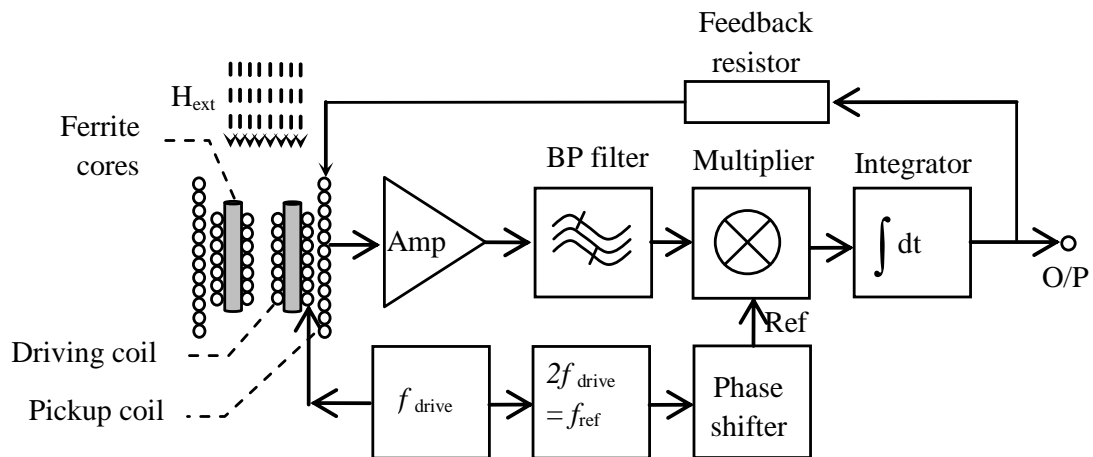


Fig 4.15 Schematic diagram of the fluxgate with its readout electronics

driving frequency whose amplitude is proportional to the strength of the external magnetic field [74,75,99]. The amplitude of the second harmonic signal is phase sensitively detected (PSD), integrated and fed back to the sensing coil to nullify the input field. Finally, the voltage developed at the output of the integrator is proportional to the externally applied magnetic field.

Here, it may be noted that external magnetic field is also directly coupled to the pickup coil producing a voltage (with the same frequency) in addition to the voltage due to the

permeability modulation of the core for the same external magnetic field. In order to eliminate the voltage induced in the pickup coil due to the direct coupling, a band pass filter is introduced between the amplifier and multiplier with the central frequency equivalent to twice the driving frequency. In general, the cutoff frequency of the band pass filter is $(2f_{\text{drive}} \pm f_{\text{BW}})$, where f_{drive} is the driving frequency and f_{BW} is the bandwidth of the system. In our case, the driving frequency is 15.736 kHz and the bandwidth of the system set by the integrator is about 3 kHz at 3 dB point.

When we apply the signal frequency from DC to higher value (up to 40 kHz) by keeping the signal amplitude constant, one can observe three peaks, one is the actual signal frequency, the second is $(f_{\text{ref}} - f_{\text{sig}})$ and the third is $(f_{\text{ref}} + f_{\text{sig}})$. The applied magnetic field with frequency of f_{sig} is modulated by the driving signal and the net permeability modulated signal, with the frequency of $(2f_{\text{drive}} \pm f_{\text{sig}})$, is multiplied by the reference frequency ($f_{\text{ref}} = 2f_{\text{drive}}$) by the multiplier. The output of the integrator contains genuine signal (f_{sig} , with the same applied signal frequency) and is fed back to the feedback coil. The next one is the applied magnetic field which is directly coupled to the pickup coil (without permeability modulation of the ferrite core) and the voltage developed in the pickup coil contains only signal frequency (f_{sig}). This voltage is also multiplied by the multiplier with the same reference frequency and the output contains voltages with frequencies $(f_{\text{ref}} - f_{\text{sig}})$ and $(f_{\text{ref}} + f_{\text{sig}})$. Since the bandwidth of the system set by the integrator is 3 kHz, the output voltage with frequency $(f_{\text{ref}} + f_{\text{sig}})$ will simply be rejected.

For example, if the frequency of the applied magnetic field is as low as 1 kHz, the voltage appearing at the output of the integrator is a genuine 1 kHz which is proportional to the input magnetic field ($V \propto B$). If any voltage traces with the same frequency is available at the input of the multiplier due to direct coupling ($V \propto \partial B / \partial t$), the integrator may reject the voltages with frequencies of 30.472 kHz and 32.472 kHz. Nevertheless, if

any voltages with high frequencies is available at the output of the integrator, they may interrupt the low frequency genuine signal (refer the inset of Fig 4.14 (a)).

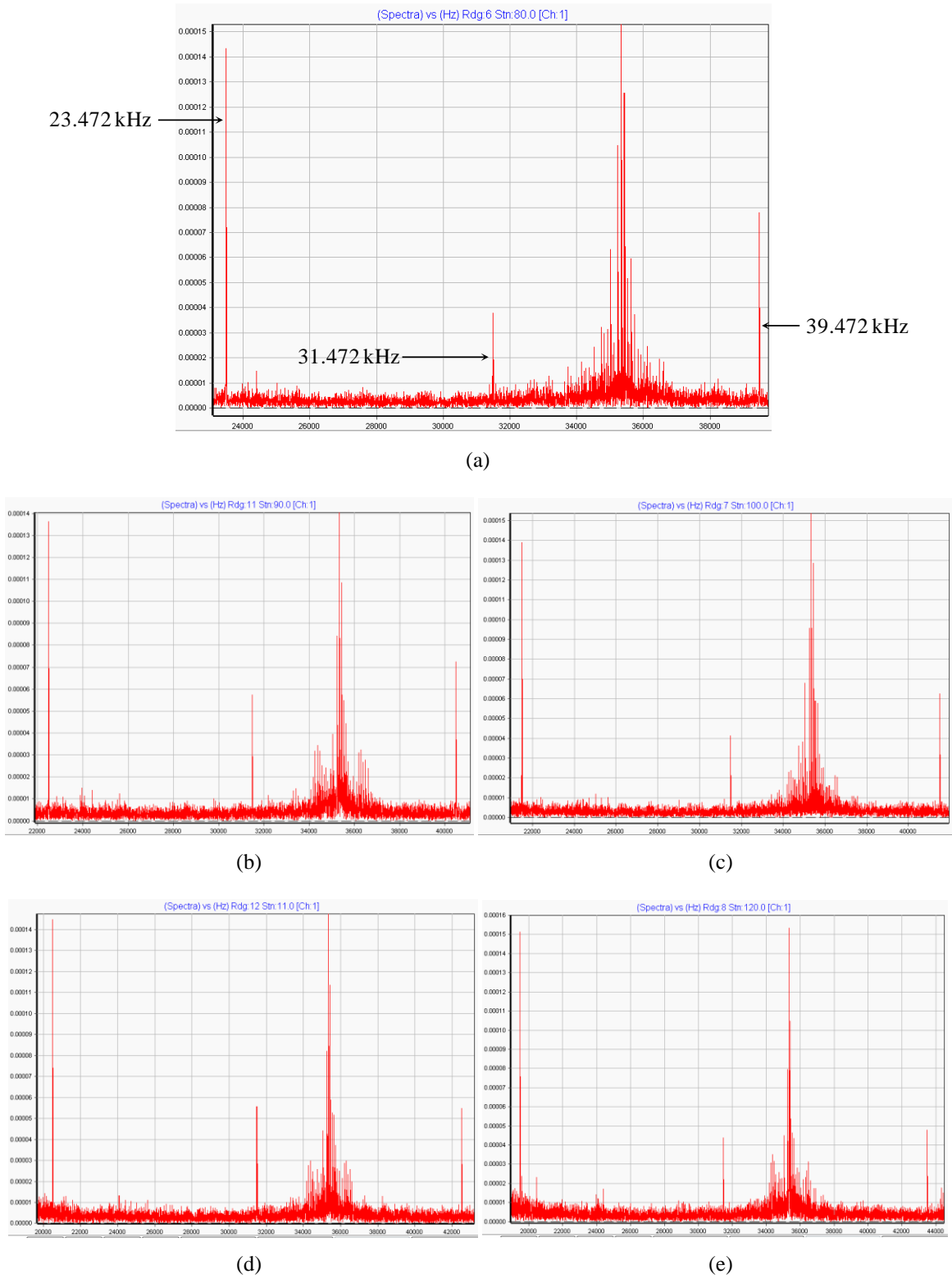


Fig 4.16 Spectrum showing signals for f_{ref} , $(f_{\text{ref}} - f_{\text{sig}})$ and $(f_{\text{ref}} + f_{\text{sig}})$ for (a) $f_{\text{sig}} = 8$ kHz, (b) $f_{\text{sig}} = 9$ kHz and (c) $f_{\text{sig}} = 10$ kHz, (d) $f_{\text{sig}} = 11$ kHz, (e) $f_{\text{sig}} = 12$ kHz

However, the case is different with input signal of high frequency. When the external magnetic field with high frequency comparable to the driving frequency is coupled to the pickup coil, the corresponding voltage should be multiplied with reference signal and the output of the multiplier should have low frequency ($f_{\text{ref}} - f_{\text{sig}}$) which is available at the output of the integrator. For example, if the frequency of the applied magnetic field is 8 kHz, the pickup coil does not contain output voltage of sufficient magnitude due to permeability modulation. At the same time, the voltage induced in the pickup coil is high due to direct coupling of high frequency signal and this voltage is available at the input of the multiplier without attenuation. The multiplier output has the voltages with frequencies of 23.472 kHz and 39.472 kHz. Although, none of these high frequency signals should be available at the output of the integrator, it has been experimentally verified that both of these are present in the fluxgate output and the spectrum showing the same is presented in Fig 4.16 (a). Similar examples of experimental observations for input frequencies of 9 kHz, 10 kHz, 11 kHz and 12 kHz are presented in Fig 4.16 (b), (c), (d) and (e) respectively. In these figures, the two frequencies ($f_{\text{ref}} - f_{\text{sig}}$) and ($f_{\text{ref}} + f_{\text{sig}}$) are clearly visible along with the driving frequency 31.472 kHz.

In general, as an end user when we use a fluxgate magnetometer with a bandwidth of 3 kHz for transient electromagnetic measurements we expect that the high frequency signals may attenuate (due to the cut off frequency of the integrator) but in reality, it is different. Instead, the early signal with high frequency components may reach negative values due to the dual behavior. The strength of the direct coupling is entirely dependent on the nature of the terrain as well as the magnitude of the primary magnetic field used to induce eddy currents in the ground.

4.8. Conclusion

As part of the development of SQUID based TDEM system for geophysical applications, experiments have been conducted in the field to familiarize with field survey techniques. In this survey, a room temperature magnetic field sensor, fluxgate, has been used to sense the decay of the secondary magnetic field. During this survey, it was noticed that the output of the fluxgate reached negative values when we perform TDEM central loop sounding measurements. Subsequently, additional measurements have been carried out in the laboratory with a portable transmitter loop and its results were compared with the TDEM measurements performed with SQUID sensor. For further confirmation, TDEM central loop sounding measurements have been carried out with both the magnetometers such as fluxgate and SQUID in a layered earth where a conducting layer is covered with thick highly resistive overburden. The results obtained in these measurements have been analyzed and compared. The decay of the secondary magnetic field measured by the SQUID never reached negative value at earlier time whereas the same measured by the fluxgate reached negative values. The width of the time window reaching negative values is also dependent upon the size of the transmitter loops. The reason for this negative decay at earlier time has been explained with sufficient experiments performed at laboratory. It is proved that the SQUID based magnetometer behaves as a pure magnetic field sensor throughout the decay. On the flip side, the fluxgate magnetometer works as an induction coil at early time and as magnetometer at later time.

Chapter 5

DEVELOPMENT OF TRANSIENT EDDY CURRENT NDE SYSTEM FOR DETECTION OF DEFECTS IN CONDUCTING MATERIALS

This chapter provides (1) brief introduction to the non-destructive evaluation (NDE) techniques for defect detection; (2) principle of operation of transient eddy current NDE technique; (3) the advantages of a transient eddy current NDE technique using magnetometers; (4) advantages of using a double “D” excitation coil; (5) development of a fluxgate magnetometer based transient eddy current NDE system using double “D” excitation; (6) detection of subsurface defects in stacks of Aluminum plates and correlation of defect depth with diffusion time of eddy current induced in the conducting material.

5.1. Introduction

Non-destructive evaluation refers to testing and monitoring the health of a material in order to ensure its quality and functionality without altering or invading the material properties [42]. This is important so that both time and effort can be saved during the manufacturing process. Various NDE techniques are used by industries during the quality assurance process to detect defects and flaws in a material. The defects may arise due to improper manufacturing of the parts, flaws in raw material used for manufacturing the parts or due to post-manufacturing processes such as transportation and storage [100]. Usage of parts with defects in them may lead to unwanted accidents and loss of money in adverse cases. Few NDE techniques can be listed as ultrasonic, eddy current, radiography etc. In general, an NDE system to detect defects consists of an excitation unit which sends a signal to excite the test specimen, a sensor or receiver unit to sense the response from the test specimen and a data acquisition system to record the response received by the sensor.

Such an NDE technique is called active NDE technique. In contrast, passive techniques record response of objects without excitation.

Eddy current NDE technique is a popular technique to detect defects and loss of conducting thickness due to corrosion in thick conductive material parts used in aerospace, automobile as well as other manufacturing and processing industries [41,43,101,102]. Eddy current NDE technique works on the principles of Faraday's law of electromagnetic induction and Lenz's law; whenever a conductor experiences a time varying magnetic field, an eddy current is induced in the conductor in such a way that it produces a secondary magnetic field which opposes its cause, that is the primary magnetic field. Eddy current NDE is broadly classified into two categories such as conventional frequency domain electromagnetic (FDEM) and transient eddy current or time domain electromagnetic (TDEM) based on the nature of excitation of eddy currents and its detection.

In the case of frequency domain eddy current NDE, eddy currents are induced in the specimen by applying a time varying magnetic field of fixed excitation frequency f . The induced eddy currents produce secondary magnetic fields which oppose the change of primary magnetic field. The net magnetic field is either measured by the pickup coil ($V \propto dB/dt$) or with B-field sensor like SQUID ($V \propto B$). The voltage which is proportional to the net magnetic field produced at the sensor output is phase sensitively detected by a using a lock-in amplifier. The size and depth of the defect can be evaluated with the phase and amplitude of the lock-in amplifier output.

The physical basis for the eddy current induction in conducting material is contained in the Faraday's law

$$\vec{\nabla} \times \vec{J} = -\mu\sigma \frac{\partial \vec{H}}{\partial t} \quad (5.1)$$

Here μ is the magnetic permeability and σ is the electrical conductivity of the material. The time varying applied magnetic field $\partial \vec{H}/\partial t$ will induce a current in the material in accordance with the equation (5.1) and these currents are referred to eddy currents. In general, the time varying applied magnetic field is sinusoidal, $H = H_0 e^{i\omega t}$, where ω - the angular frequency $= 2\pi f$. So, equation (5.1) becomes

$$\vec{\nabla} \times \vec{J} = -i\mu\sigma\omega\vec{H} \quad (5.2)$$

Qualitatively, the curl of the induced eddy currents is out of phase with the applied time varying magnetic field and proportional to the frequency of the applied magnetic field and electrical conductivity of the material. The strength of the induced eddy currents in the material decreases exponentially with the thickness d of the specimen as $J = J_0 e^{-d/\delta}$, where J_0 is the eddy current at the surface and δ is the skin depth or magnetic penetration depth of the material which is defined as

$$\delta = \left(\frac{1}{\pi\sigma\mu f} \right)^{1/2} \quad (5.3)$$

Hence, the skin depth strongly depends on the excitation frequency for given electrical conductivity and magnetic permeability of the material.

According to the equation (5.2), for defect or flaw detection in the conducting materials, the strength of the eddy current can be increased by increasing the frequency of the applied excitation magnetic field. However, this limits the depth of the defect detection due to the skin depth limitation. At the same time, the use of low excitation frequency to enhance the depth of investigation reduces the signal strength and the sensor may often reach the noise floor. The strength of the signal could be enhanced by increasing the number of turns of the pickup coil (in case pickup coil is used as a sensor) which again leads to poor spatial resolution due to the size of the pickup coil. Otherwise, the SQUID whose sensitivity is extremely high for magnetic field detection even operating at low

frequency has to be used for detecting the subsurface defects in conducting materials [80]. In addition to this, the SQUID based NDE system uses superconducting pickup loop in the form of either first order gradiometer or second order gradiometer and one can make the superconducting loop with a single turn and small in size to couple the magnetic field changes occurred in the vicinity of the specimen due to the defect. Again the SQUIDs are superconductivity based sensor which operates in either liquid nitrogen (high T_c SQUIDs) or liquid helium (low T_c SQUIDs) and is highly expensive.

In addition to this, it is well known that the amplitude of the induced eddy currents at a given depth from the surface reaches a maximum value at an optimum excitation frequency. The defects located at different depths for a given specimen thickness cannot be detected with the use of single excitation frequency and hence the experiments have to be repeated with different frequency (multi-frequency excitation) in order to probe the entire depth of the specimen and this method is time consuming. All these drawbacks could be overcome with use of pulsed eddy current NDE or transient eddy current NDE.

In pulsed eddy current NDE, the eddy currents in the specimen are induced using pulsed excitation and the decay of the eddy current is measured with time. The decay of the eddy current consists of continuum of frequencies and hence the entire thickness of the conducting material could be investigated in a single shot. The use of single pulsed excitation is highly advantageous in probing defects located at different depths from near surface to deeper layers of the conducting specimen [44,103,104]. When measurements are made in time domain, the signal variations due to the presence of defects or flaws near the surface can be seen at earlier time whereas the same located deeper can be seen at later time. In this method, the strength of the eddy currents induced in the specimen depends on the switch off time of the current applied to the excitation coil. The switch off time depends on the resistance and inductance of the excitation coil. When the switch off time

is shorter, strong EMF is induced which drives more eddy current in the material. The induced eddy currents decay with time and its decay rate is dependent on the conductivity of the specimen. The induced eddy currents in conducting material migrate downward and expand outwards in the form of “smoke rings” and decay. The time, t , at which the decay of eddy current is maximum and the corresponding depth is known as diffusion depth, d

$$d = \left(\frac{2t}{\sigma\mu} \right)^{1/2} \quad (5.4)$$

which is analogous to the skin depth in frequency domain. Fig 5.1 shows schematic illustration of the eddy currents in both the frequency and time domains.

Pulsed eddy current NDE technique has found application in detection of loss of wall

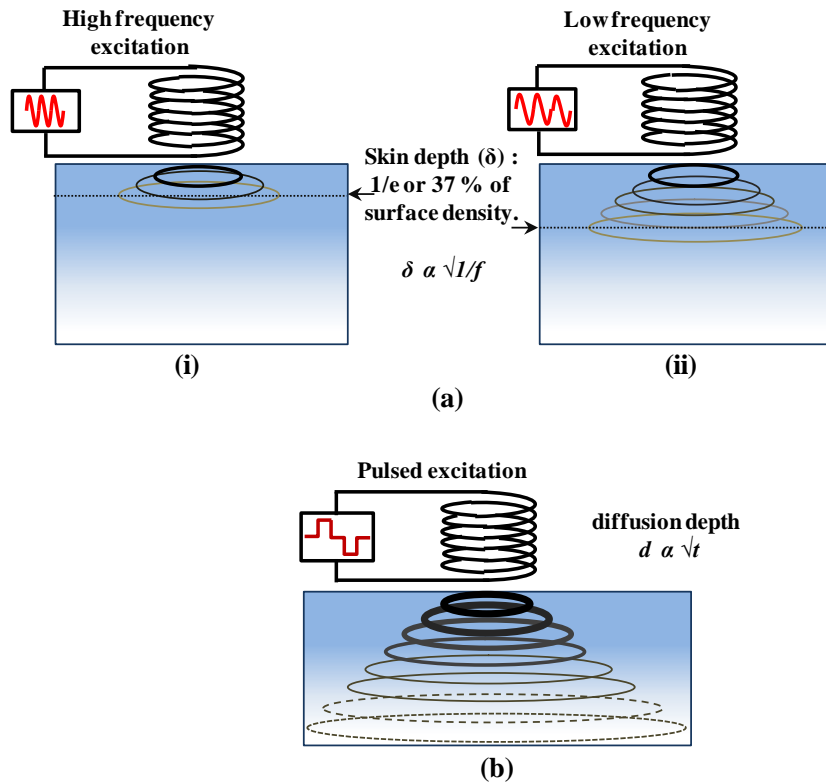


Fig 5.1 Illustration of the eddy current NDE system showing eddy currents in conducting specimen in (a) frequency domain using sinusoidal excitation signal of (i) higher frequency and (ii) relatively lower frequency. For given conductivity and permeability, skin depth is inversely proportional to frequency and thus, depth of investigation is limited by excitation frequency. However, (b) pulsed excitation used in time-domain consists of continuum of frequencies; each diffusion depth corresponds to a transient time and thus, different depths can be investigated using same excitation. Here, strength of the current is proportional to line thickness of the eddy current loops.

thickness due to corrosion [105–108] and detection of flaws in multilayered structures [109–114]. In studies related to detection of surface and subsurface defects by using pulsed eddy current NDE, various features have been used to estimate the depth of defect. Conventionally, a reference signal is recorded over a specimen without defect and it is subtracted from a measurement signal over a specimen with similar characteristics but with a defect. The presence of defects results in non-zero difference between the reference response and the measurement response. Peak amplitude and zero crossing time of the differential signal are the most important features used to classify defect properties [53]. Such studies have shown that a deeper defect results in reduced peak amplitude and increased zero crossing times [115]. There is another feature called rising time that has been used to separate surface and deeper defects in pulsed eddy current NDE with use of Hall sensor. The time until which the difference between both the responses (reference signal and signal with defect) is zero is called the rising time [116].

The present work describes the development of fluxgate magnetometer based transient eddy current NDE system and utilization of this system for detecting defects in stacked aluminum plates up to a depth of 20 mm. In this system, the excitation coil has been used in the form of double “D” which eliminates the necessity of recording reference signal and increases the dynamic range of the system. In this system, the instruments for eddy current excitation in the metal target and the data acquisition system to record the response of the target which is sensed by the fluxgate sensor are the ones used for geophysical applications. The built-in software available in the data acquisition system processes the acquired data and displays in the form of decay curves (decay of the secondary magnetic field versus time for a particular position) and profile data (secondary magnetic field versus position for different decay times) and the same can be stored for further analysis. From this work, the experimental data has been analyzed and a new feature "diffusion

time", t_m has been introduced. This feature directly provides the information about the depth of the defect. It has also been verified that the square root of the diffusion time ($\sqrt{t_m}$) is proportional to the depth of the defect.

5.2. Principle of operation of transient eddy current NDE technique

A schematic view of the waveforms used for excitation and the response of the target with fluxgate are shown in fig 5.1. In this system, the current in the form of trapezoidal

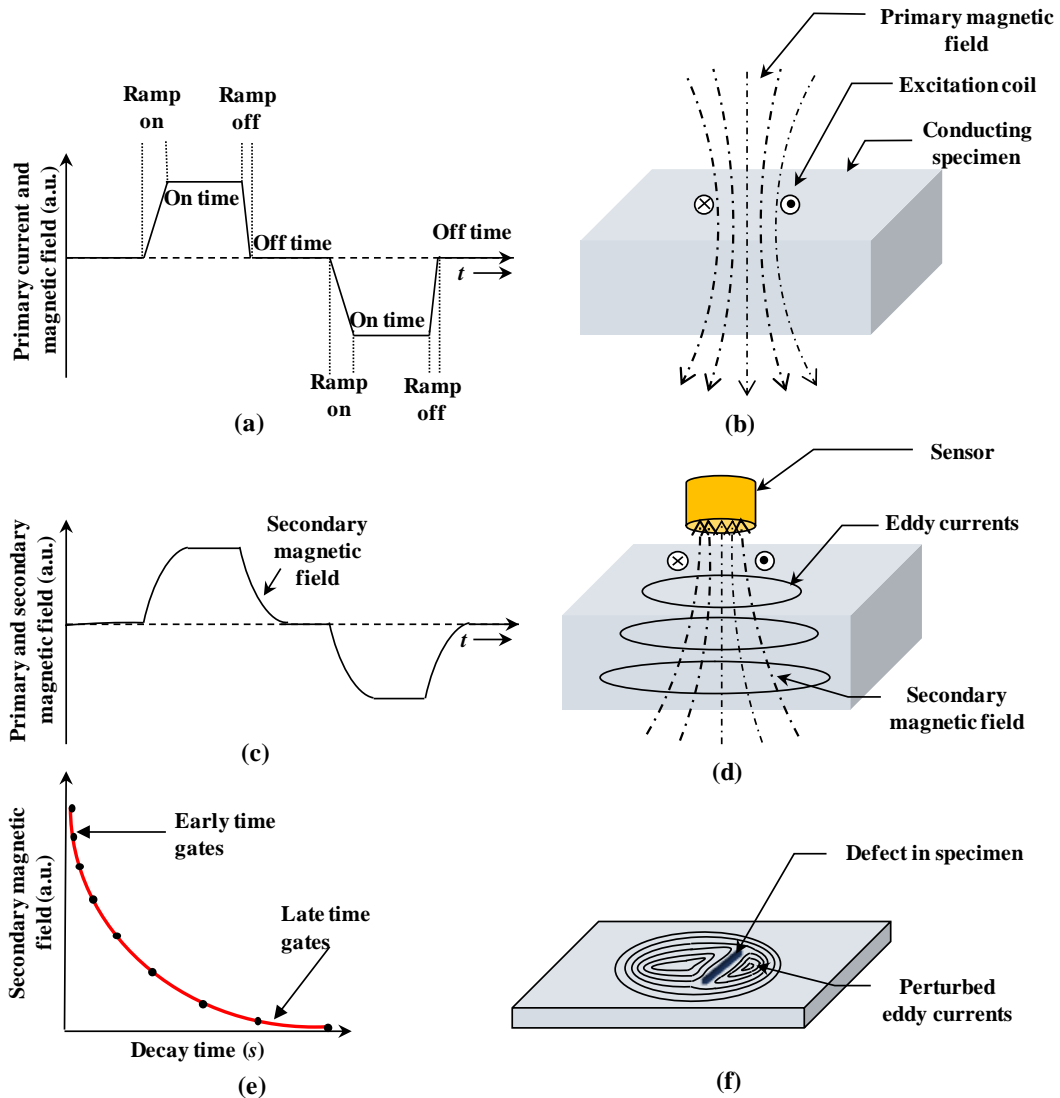


Fig 5.2 (a) Excitation current in the form of trapezoidal pulses applied to the excitation coil, (b) primary magnetic field generated as a result of the excitation current, (c) resultant field measured by magnetic field sensor, (d) generation of eddy current and its associated secondary magnetic field in conducting specimen, (e) decay of secondary field after processing and (f) perturbation of eddy currents due to the presence of defect in conducting specimen.

pulses is passed through an excitation coil to generate the primary magnetic field as shown in Fig 5.2 (a) and (b). Electromotive force is induced in nearby conducting specimen when the excitation current is suddenly switched on or off and this, in turn, generates eddy currents. The eddy currents and its associated secondary magnetic field are shown in Fig 5.2 (d) while Fig 5.2 (c) shows the primary and secondary magnetic field sensed by a magnetic field sensor. This eddy current, which is proportional to the conductivity of the object, starts decaying at a rate that depends on the resistivity of the specimen through which it flows. The presence of flaws or defects in the object perturbs the decay of the induced eddy current as shown in Fig 5.2 (f). The rate of decay of the eddy currents along with the strength of perturbations due to defect can be obtained by measuring the voltage induced in the induction coil sensor or by measuring the associated secondary magnetic field using a magnetometer. The decay profile is divided into a number of time windows as shown in Fig 5.2 (e). The earlier time windows provide information about the decay of the eddy current near the surface of the object whereas the later time windows provide information about the decay of eddy currents at greater depths.

5.3. Advantages of magnetometer over an induction coil

The response of the eddy current change due to the presence of the defect and its associated secondary magnetic field can be recorded by using either magnetometer or with an induction coil. The magnetometer directly measures the magnetic field and its output voltage is proportional to the changes of the secondary magnetic field ($V \propto B$) whereas the induction coil measures the time derivative of the magnetic field ($V \propto dB/dt$). When a circular excitation coil of radius ' a ' carrying current in the form of trapezoidal pulses of magnitude I is used to induce eddy currents in a conducting target with conductivity σ and permeability μ , the vertical component of secondary magnetic field recorded using a

magnetometer (B_z) and its time derivative recorded using an induction coil (V_z) are respectively given by the following late time asymptotically approximate equations [59]

$$B_z = \frac{Ia^2 \sigma^{3/2} \mu_0^{3/2}}{30 \sqrt{\pi}} t^{-3/2} \quad (5.5)$$

$$V_z = \frac{-Ia^2 \sigma^{3/2} \mu_0^{3/2}}{20 \sqrt{\pi}} t^{-5/2} \quad (5.6)$$

Thus, the voltage induced in the induction coil sensor decays faster than the decay of the magnetic field itself. It is therefore obvious that the voltage measured by the induction coil reaches noise floor earlier than the magnetic field. Thus, with the use of a magnetic field sensor or magnetometer to measure the magnetic field directly, a defect can be probed at greater depth as compared to that using an induction coil sensor. GMR (Giant Magnetoresistance), AMR (Anisotropic magnetoresistive) based magnetometer, Hall sensor, fluxgate and SQUID (Superconducting Quantum Interference Device) are some typical examples of magnetometers being used for NDE based defect detection [60–64,117].

5.4. Advantages of double “D” excitation Coil

Efficiency of the instrument used for the transient eddy current NDE measurements can be enhanced by modifying parameters such as the strength of the applied primary magnetic field, excitation coil size, switch-off time, etc. A stronger primary magnetic field or an excitation coil with larger number of turns or with larger area can mean an increase in the magnetic moment which can increase the strength of the induced eddy current even at larger depth. However, increasing the current also increases the primary magnetic field which may lead the sensor to saturation. Increasing the number of turns increases the inductance, which leads to longer switch-off time, thus reducing the strength of eddy currents induced. Using a circular excitation coil, a larger magnetic field cannot be produced when the sensor is saturation-limited. However, using a differential excitation coil such that the primary magnetic field measured by the sensor can be nullified prevents

the sensor from saturation while enhancing its the dynamic range. The excitation coil can be used in the planar or axial gradiometric forms.

Conventionally, in eddy current NDE systems for detection of defects, a reference signal is recorded at a place where there is no defect and later subtracted from the signal arising due to the defect in order to obtain the signal only due to the defect [118]. A planar differential coil such as one in the form of double “D” can be used to eliminate the need to record the reference signal. Since the secondary magnetic field, which is generated only during the off-time of the transient, gives information of the defect present in the material, the direct magnetic field generated by the excitation coil will be cancelled at the location of the sensor. At the same time, the target is exposed to the primary magnetic field and eddy currents induced in it. Hence, one can apply a large magnetic field in order to enhance the eddy current generation in the specimen using an excitation coil in the form of double “D”.

5.5. Fluxgate based transient eddy current NDE System

The fluxgate based transient eddy current NDE system comprises of a transmitter, transmitter controller, a double “D” differential excitation coil, a commercial three-axes fluxgate magnetometer and a fast data acquisition system, namely SMARTem24, to record the secondary magnetic field. The transmitter generates and supplies current to the excitation coil in the form of trapezoidal pulses in order to induce eddy currents in the conducting object. The frequency and duty cycle of the current pulses are controlled by the transmitter controller. The transmitter controller is accurately synchronized with the fast data acquisition system using a built-in crystal.

A set of aluminum plates fabricated with a length of 300 mm, width of 200 mm and with different thicknesses ranging between 2 mm and 20 mm in steps of 2 mm was used for this experiment. In addition to this, a 1.5 mm thick aluminum plate with an artificially

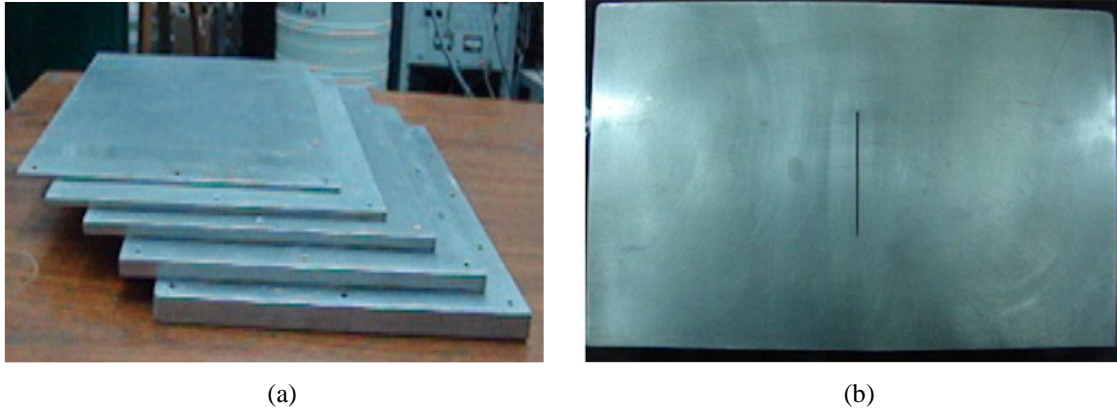


Fig 5.3 (a) Aluminum plates without defect; (b) 1.5 thick Aluminum plate with defect.

engineered defect of 70 mm length and 1 mm width was also fabricated. The defect in the aluminum plate was created using the spark erosion technique, which is also known as electrical discharge machining. The material is removed from the aluminum plate by a series of rapidly recurring current discharges between two electrodes (aluminum plate and electrode) separated by a dielectric liquid and subject to an electric voltage [80]. Fig 5.3 (a) and (b) show the photographs of the stack of aluminum plates without defect and the 1.5 mm thick plate with defect respectively. This plate with defect was used to simulate a localized loss of conducting volume in a stack of conducting plates. The length and width of the plate with the defect are identical to those of the plates without defect. The stack of aluminum plates was arranged for this experiment in such a way that the total thickness was always maintained at 21.5 mm. For example, to arrange for the defect to be located 4 mm below the top surface, a 4 mm thick flawless plate was placed above the 1.5 mm thick plate with defect. Below the defect plate, a 10 mm and a 6 mm thick flawless plate were both stacked together so that the total thickness was maintained at 21.5 mm. Likewise, the depth of the defect was shifted in steps of 2 mm up to 20 mm by rearranging the plates in the stack. The stack of aluminum plates with the defect plate was mounted over the non-magnetic sample holder of a XY scanner [79]. The XY scanner is driven using micro-

stepping drive-based stepper motors and its speed can be varied from 0.05 mm/sec to 50 mm/sec.

The double “D” excitation coil used for this test has been fabricated using suitable non-metallic and non-magnetic former with diameter of 20 mm and its each “D” carries 20 turns of copper wire of 0.2 mm diameter. The direction of the wire wound on the double “D” former is in such a way that the magnetic field produced at the center of the coil is

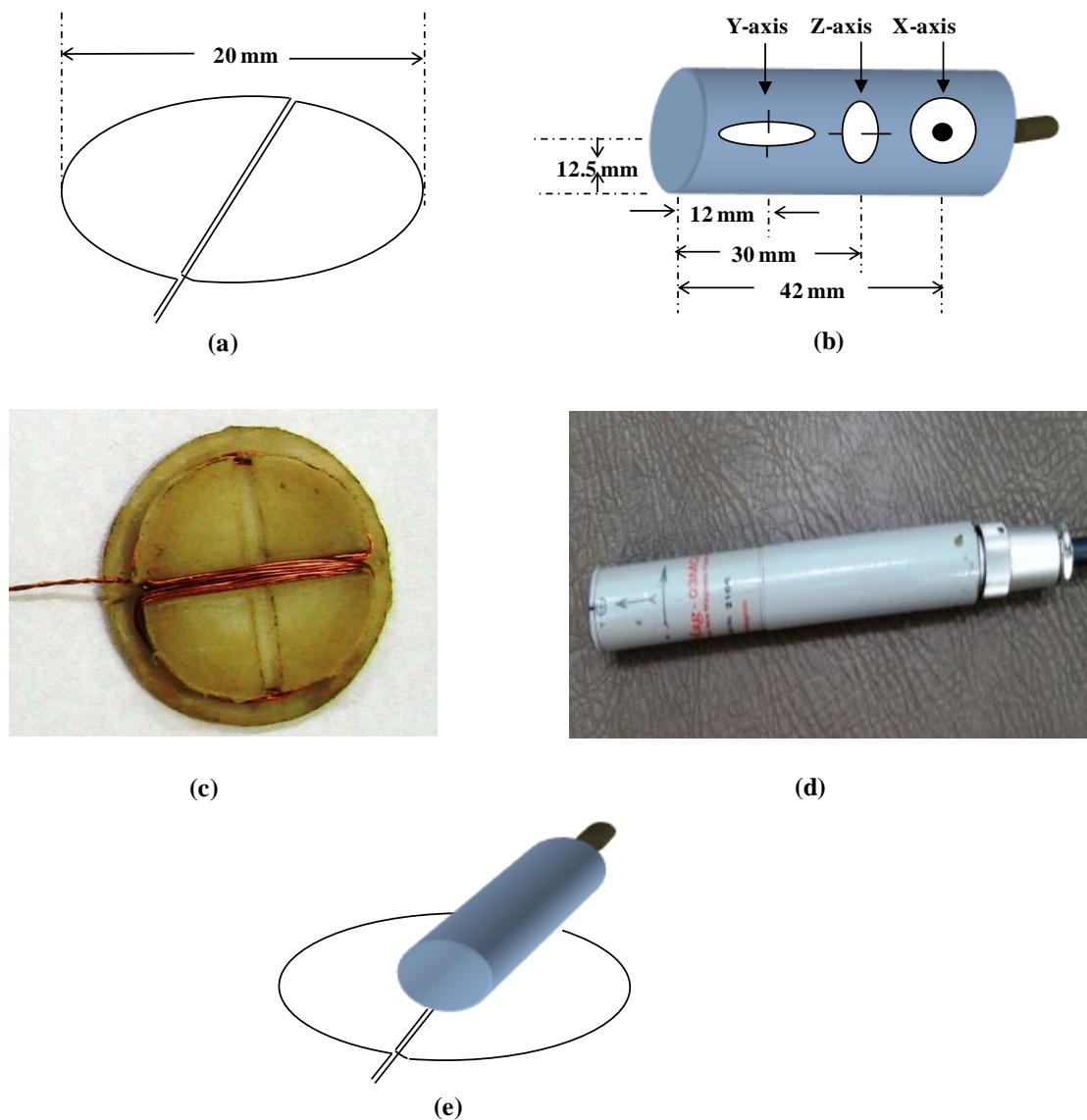


Fig 5.4 Schematic of the double “D” excitation coil, (b) three-axis fluxgate magnetometer, photographs of (c) double “D” excitation coil, (d) the fluxgate magnetometer and (e) schematic view of the orientation of the double “D” excitation coil and fluxgate magnetometer

minimum or zero. Fig 5.4 (a) shows the schematic of the double “D” excitation coil and Fig 5.4 (c) shows the photograph of the double “D” excitation coil wound over an FRP former. The transmitter supplies current to the double “D” excitation coil to induce eddy currents in the nearby conducting material and the output of the fluxgate magnetometer is connected to the input of the SMARTem24 receiver to record the decay of the secondary magnetic field generated in the stack of conducting plates containing the defect.

The fluxgate sensors are widely used in applications such as measurement in outer space and terrestrial as well as naval applications [75,119]. Fluxgate sensor measures the absolute magnetic field in a frequency range between DC and a few kHz with minimum magnetic field of about 0.5 to 1 nT in time domain and about 5 - 10 pT/ $\sqrt{\text{Hz}}$ at 1 Hz in frequency domain in a shielded environment. Fluxgate comprises of an excitation coil wound over a highly permeable soft iron core in the form of differential configuration, a pick-up coil and a feedback coil. Here, the core permeability is modulated by applying high frequency alternating magnetic field to the excitation coil where the amplitude of the magnetic field is just above the saturation of the core. The response field or secondary magnetic field is detected by the additional pickup coil. When there is no external field, the secondary field does not contain a second harmonic of the driving frequency. When an external field is applied to the sensor, the permeability of the core is modulated and a second harmonic signal is coupled to the pickup coil. This second harmonic signal is then multiplied with the reference frequency which is twice the driving frequency. The multiplier output is further integrated and fed back through a feedback resistor to nullify the input. Therefore, the output voltage of the integrator measured across the feedback resistor is proportional to the applied external magnetic field. In this work, we have used the MAG-03 CL100 three axes fluxgate magnetometer procured from Bartington, UK and its bandwidth is limited to less than 3 kHz. The maximum magnetic field measured using

the fluxgate is $\pm 100 \mu\text{T}$ corresponding to $\pm 10 \text{ V}$ at the read-out electronics [120]. The schematic view of the three axes fluxgate magnetometer MAG-03 CL100 is shown in Fig 5.4 (b) and its photograph is shown in Fig 5.4 (d). The y-axis magnetometer of the fluxgate has a standoff distance of 12.5 mm from outer surface of the fluxgate enclosure while the z-axis is at a standoff distance of 30 mm. So, in order to reduce the lift-off distance from conducting specimen to the magnetometer, the y-axis magnetometer is used in the present study to measure the vertical component of the magnetic field. Fig 5.4 (e) shows orientation of the fluxgate over the double “D” excitation coil.

5.6. Experimental details

The block diagram of the experimental setup of the fluxgate based TDEM system is shown in Fig 5.5 and the photograph of the system is shown in Fig 5.6. A trapezoidal current pulse of 1 A with pulse repetition at every 400 ms was transmitted through the

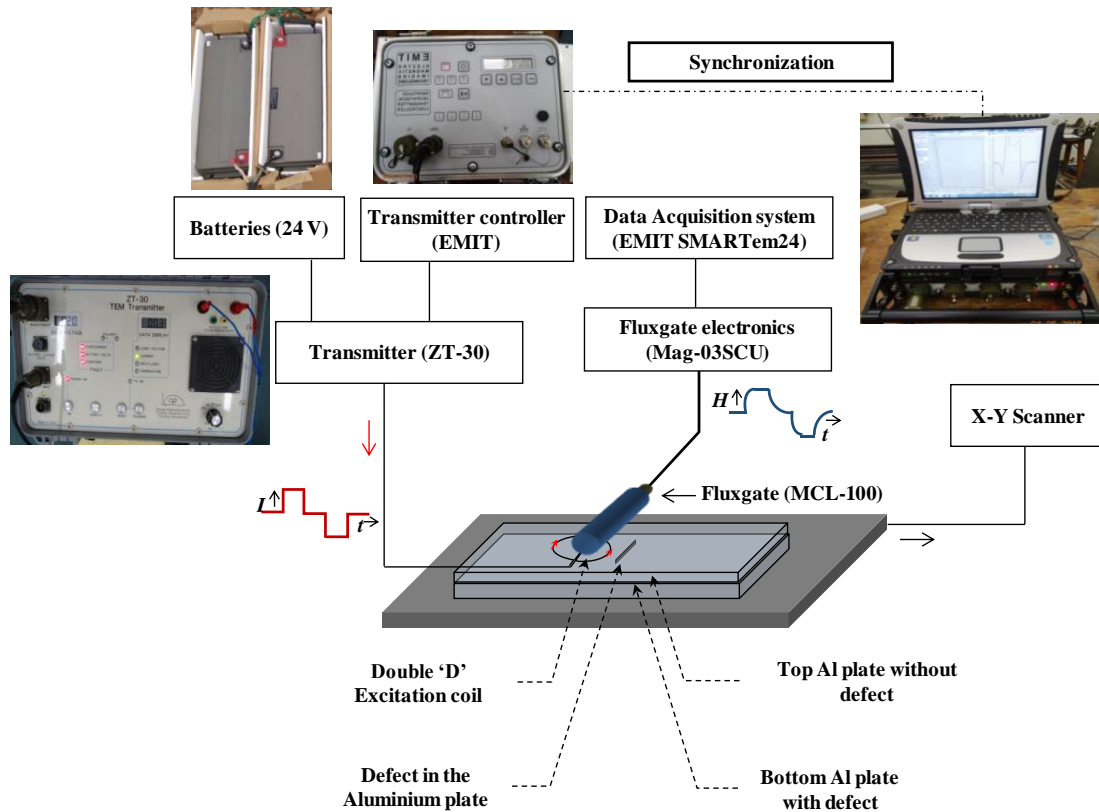


Fig 5.5 Block diagram of the fluxgate based TDEM NDE system

double “D” excitation coil using the transmitter and the transmitter controller. The stack of aluminum plates with the defect plate was scanned using XY scanner and the fluxgate output was recorded as a function of positional coordinates. The scanning speed was chosen to be 0.05 mm/s and the raw data was recorded for 25.6 s (128 stacks). The step size has been chosen to be 1.5 mm based on the scanning speed, initialization time of data acquisition system and time taken for 128 stacks. The decay of the secondary magnetic field recorded at each location was stacked and averaged to suppress uncorrelated noise. Each decay profile is divided into 32 time windows in which the earlier windows were averaged over a shorter interval due to larger signal strength and the later windows were averaged over a longer interval as the signal strength approaches floor noise of the sensor. The built-in software in the SMARTem24 data acquisition system displays the decay transient after averaging. The experiments were repeated at every 30 s in order to obtain the field profile at different locations in steps of 1.5 mm along a line perpendicular to the length of the defect.



Fig 5.6 Photograph of the fluxgate based TDEM NDE system

5.7. Results and discussion

Fig 5.7 (a) and (b) respectively show pictorial representation of circulating eddy currents around the defect location and the corresponding decay and profile plots for the defect below 4 mm and 6 mm. In order for the defect to cross the double “D” excitation coil symmetrically, the scanning direction was chosen to be perpendicular to the length of the defect. A dipolar signal could be obtained this way, provided that the length of the defect is sufficiently longer than the overall diameter of the double “D” excitation coil. The differential secondary magnetic field produced by the conducting object is minimum (signal due to misalignment, if any) or zero (perfect alignment) in the defect free region

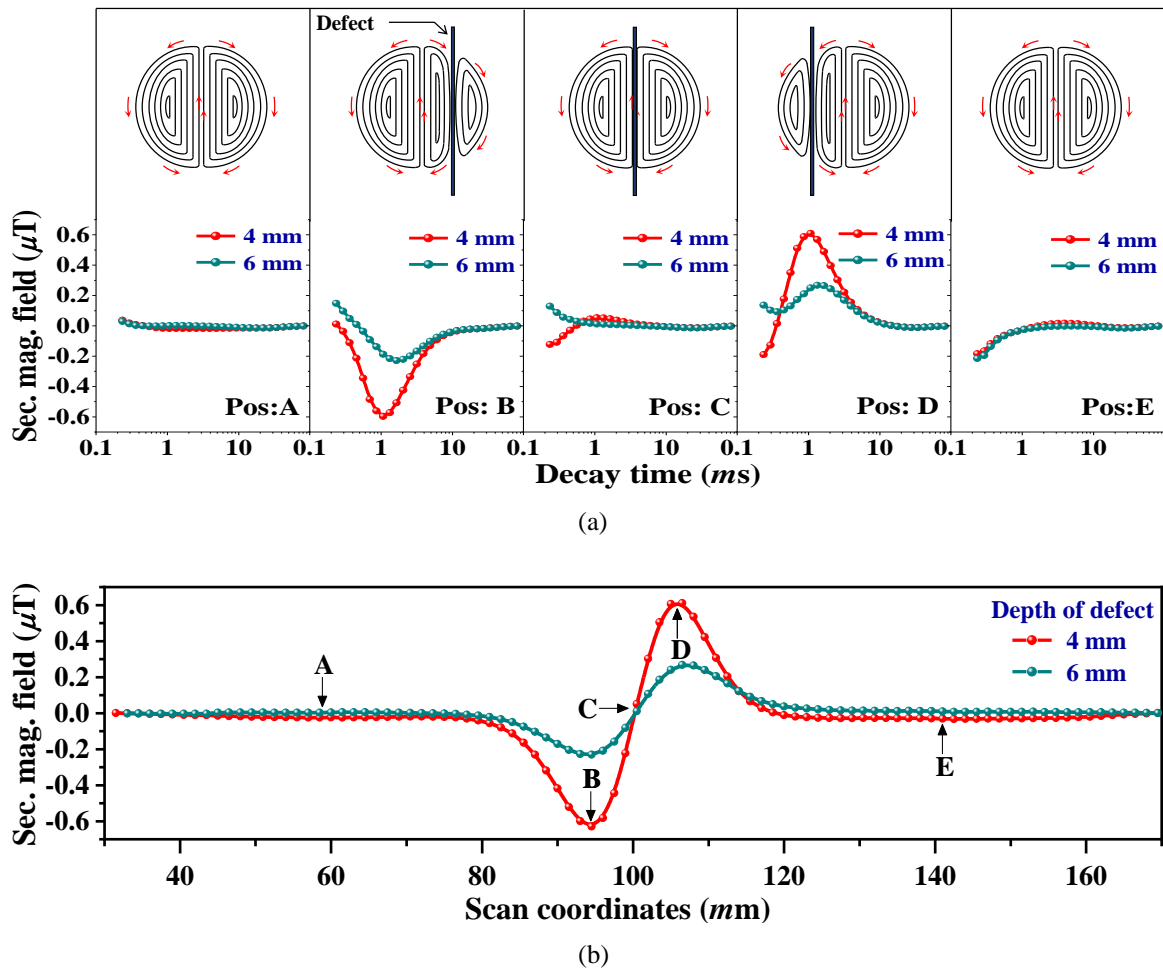


Fig 5.7 (a) Pictorial representation of the eddy current flow patterns due to the double ‘D’ excitation coil in the vicinity of a defect (from (A) to (E)) and corresponding decay transients for a defect at a depth of 4 mm and 6 mm below the surface. (b) Field profile derived from the decay transients recorded by scanning across the defect where the maximum eddy current perturbation occurs.

(refer positions A and E in Fig 5.7). At position C, the induced secondary field is equal in magnitude and opposite in direction on both sides of the defect and the differential field coupled to the sensor is minimum. At position B, the induced eddy current due to the right side of the double “D” experiences higher perturbation compared to that induced by the left side of the double “D” while the opposite happens for position D. Thus, a dipolar signal has been obtained as the defect passes through the double “D” excitation coil and fluxgate magnetometer. Fig 5.7 (b) shows profiles for the defects below 4 mm and 6 mm

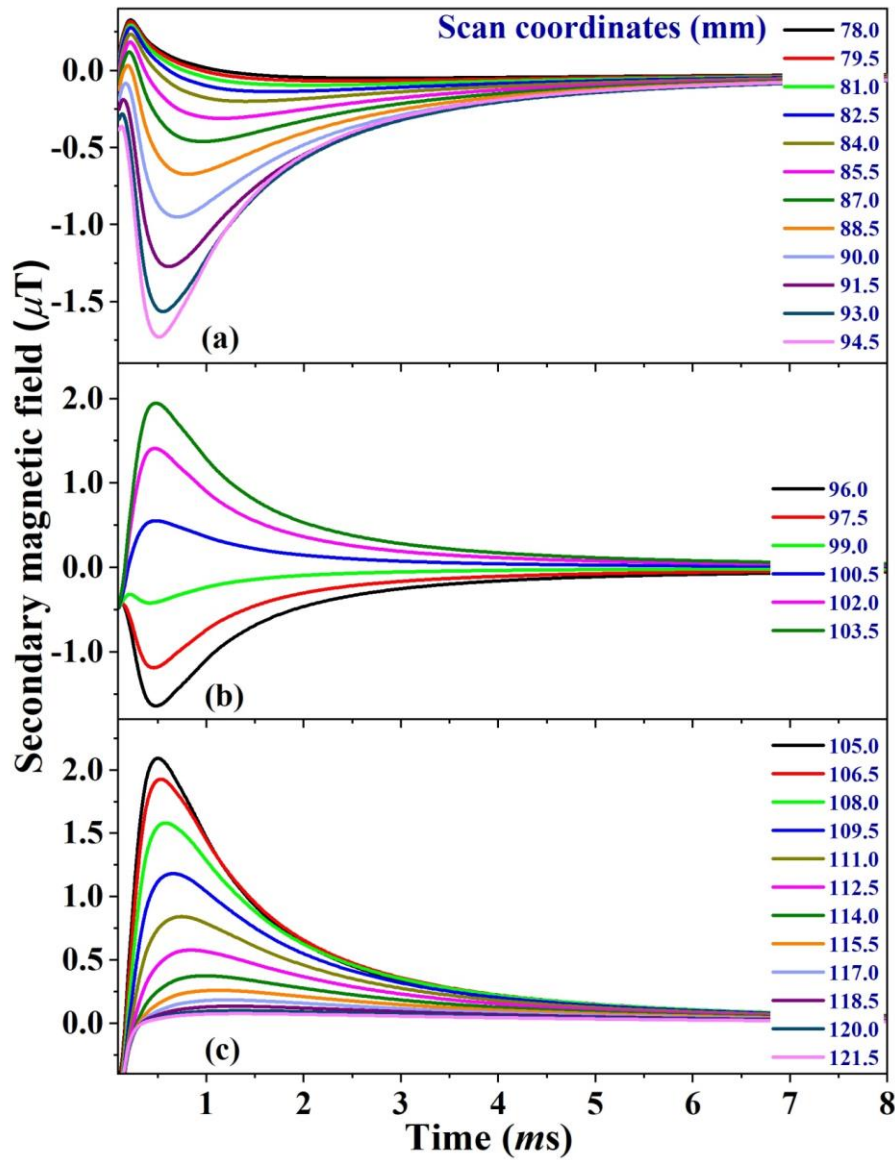


Fig 5.8 Decay of the differential secondary magnetic field at different positions for the defect located at a depth of 2 mm

and it can be seen that the change of amplitude of secondary magnetic field for a defect located at a depth of 4 mm is higher than that of a defect located at a depth of 6 mm below the surface (from positions B and D).

Plots corresponding to decay of secondary magnetic field in the vicinity of the defect located below 2 mm for different locations along the scanning line are given in Fig 5.8. From Fig 5.8 (a), it is clear that the secondary magnetic field due to the perturbations in eddy current increases as the defect approaches the sensor (positional coordinates from 78

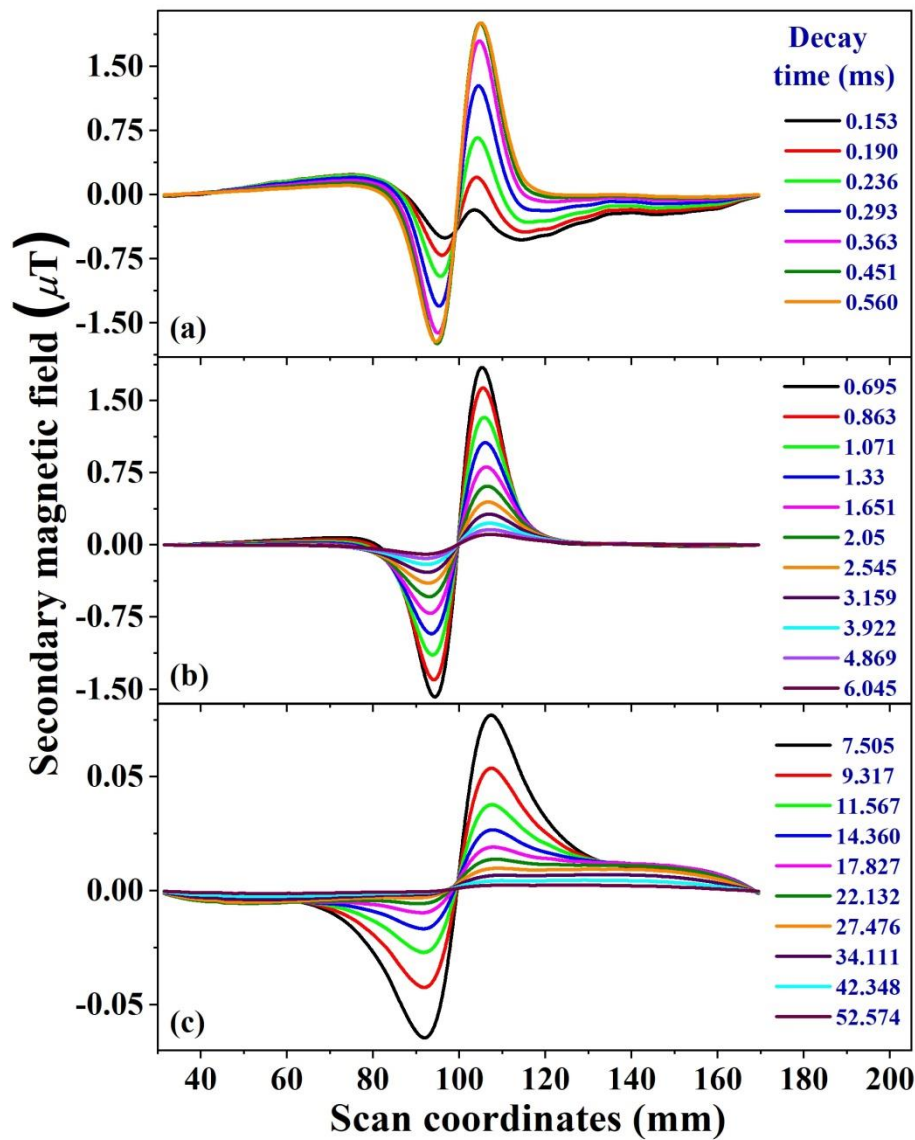


Fig 5.9 Profile plots showing decay of secondary magnetic fields for defect at a depth of 2 mm at (a) early, (b) intermediate and (c) late time windows

mm to 94.5 mm). Further, the perturbations reduce towards zero when both sides of the double “D” coil lie symmetrically on both sides of the defect (positional coordinates from 96 mm to 99 mm in Fig 5.8 (b)). After this, the secondary magnetic field due to eddy current perturbations is in opposite direction (positional coordinates from 100.5 mm to 103.5 mm in Fig 5.8 (b)) and increases with further movement of the defect away from the sensor (positional coordinates from 105 mm to 121.5 mm), as shown in Fig 5.8 (c).

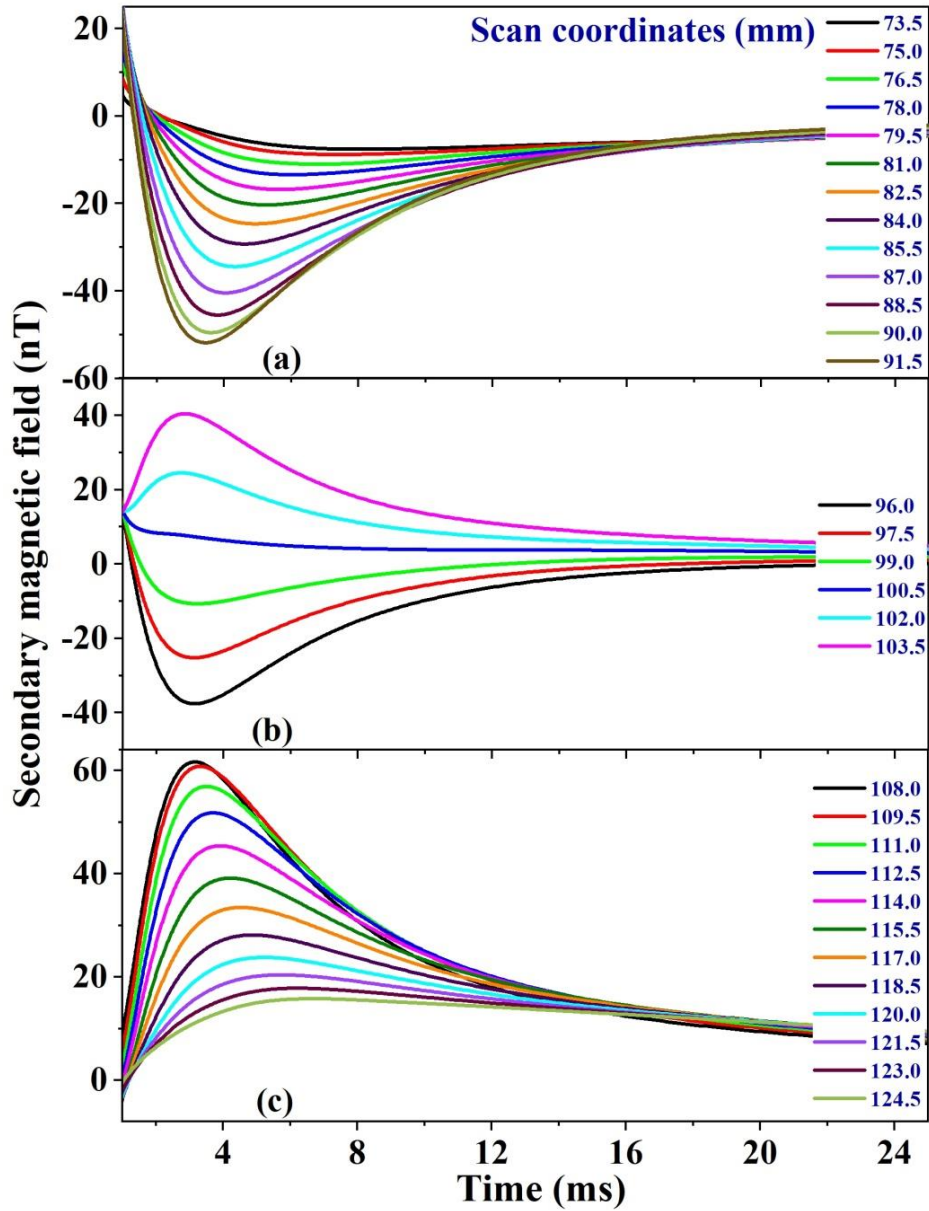


Fig 5.10 Decay of the differential secondary magnetic field at different positions for the defect located at a depth of 10 mm.

The decay of secondary magnetic field with respect to positional coordinates for defect below 2 mm depth are presented in profile plots in Fig 5.9. Fig 5.9 (a) shows the differential secondary magnetic field in early time windows when the signal strength increases with time and reaches maximum at 0.56 ms as the eddy currents diffuse downward from the surface towards the defect location. Fig 5.9 (b) presents the secondary magnetic field at intermediate times indicating a decrease in the secondary magnetic field as the eddy currents cross the defect and further diffuse downward resulting in further reduction of secondary magnetic field strength at late times as shown in Fig 5.9 (c).

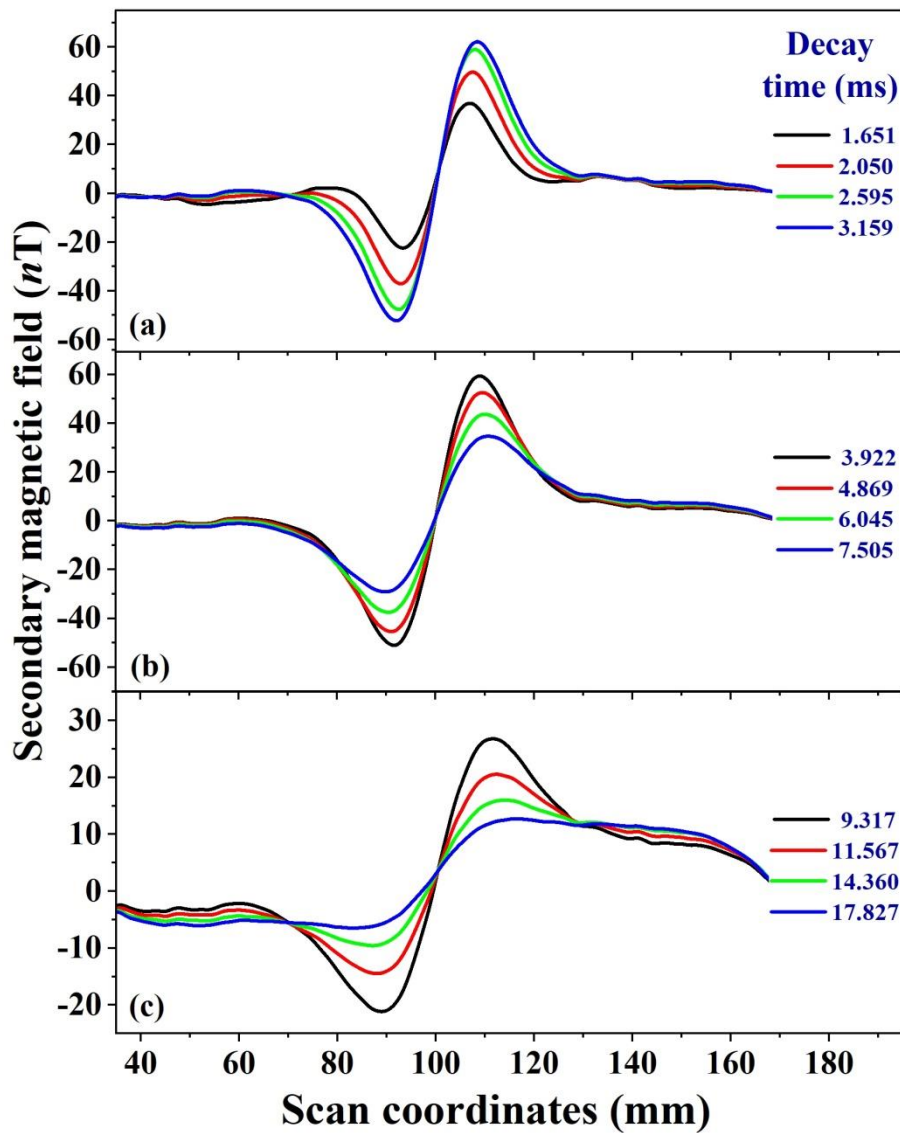


Fig 5.11 Profile plots showing decay of secondary magnetic fields for defect at a depth of 10 mm at (a) early, (b) intermediate and (c) late time windows.

Similarly, the decay and profile plots corresponding to perturbations in secondary magnetic field due to defect located at a depth of 10 mm are presented in Fig 5.10 and Fig 5.11 respectively. Here, the change of the secondary magnetic field gradually increases from earlier time windows, reaching maximum at 3.159 ms, and subsequently decreases. From this, it is clear that a diffusion time, t_m , of 3.159 ms (for defect at 10 mm depth) at which the changes of the eddy current due to the presence of the defect are maximum gives the information of the defect depth. Similar experiments were repeated for defect at different depths and corresponding decay and profile plots are obtained.

The decay and corresponding profile plots for defect at depth of 20 mm are shown in Fig 5.12 (a) and (b) respectively. From the figure, it can be inferred that the secondary magnetic field strength has reduced in magnitude and the maximum change of eddy

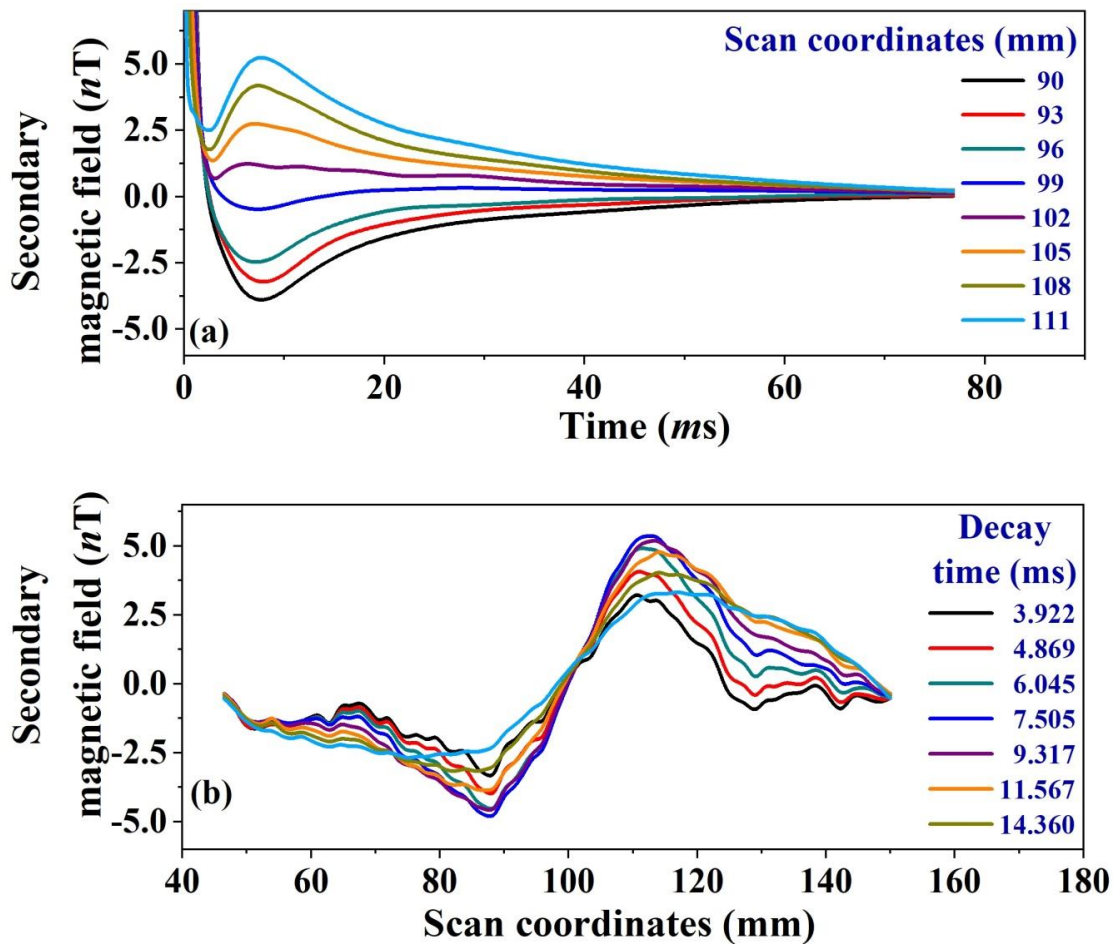


Fig 5.12 (a) Decay and (b) profile plots for changes of secondary magnetic field due to defect at depth of 20 mm.

current also occurs at late time of about 7.5 ms. From these experiments, the changes of the differential secondary magnetic field for the defects at different depths have been obtained and plotted against time, as shown in Fig 5.13. It can be observed that the maximum net differential secondary field for the defect located near the surface is higher as compared to that of the defect located deeper.

For the defect located at a depth of 2 mm, the induced eddy currents are perturbed in the vicinity of the defect at an earlier time and reach a maximum value and subsequently decay. Fig 5.13 (a) shows that the defect located below 2 mm show maximum

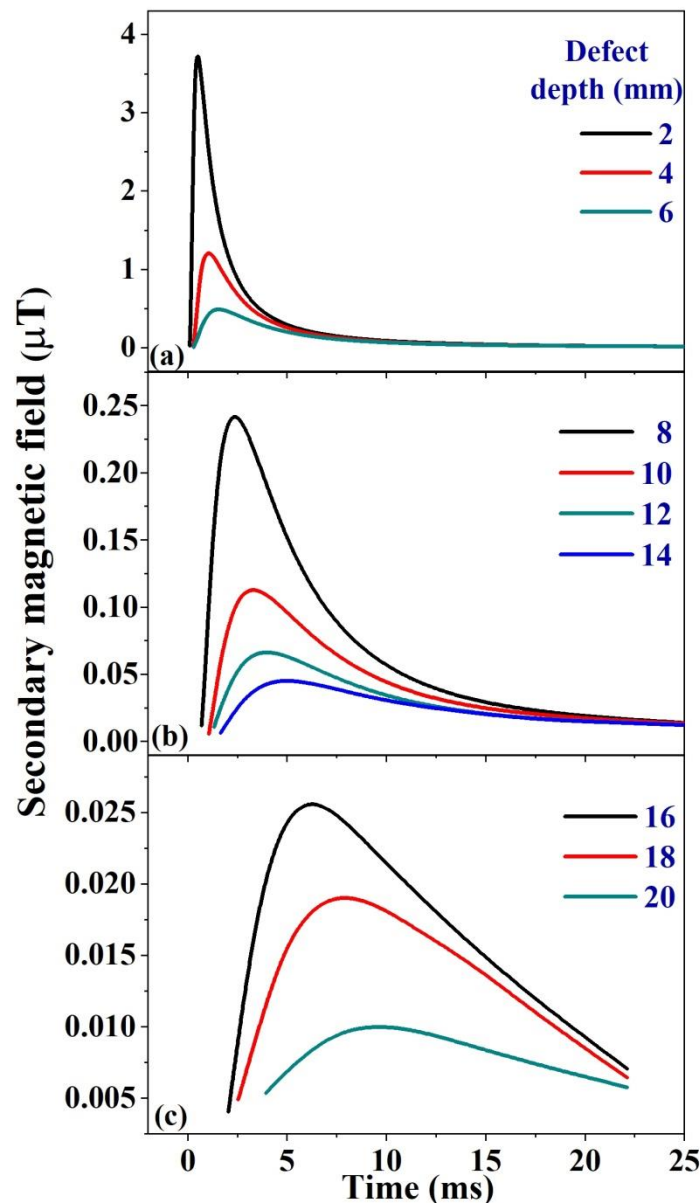


Fig 5.13 Changes of secondary magnetic field with decay times for defect at different depths

perturbations in eddy currents at early time gate of 0.56 ms while Fig 5.13 (b) and (c) show that the eddy current perturbations occurred at a later time for the deeper defects. For defect located at a depth of 20 mm, the maximum perturbations in eddy currents occur at about 9.40 ms. Therefore, the time at which the net change of the measured differential secondary magnetic field reaches a maximum value is taken to be the diffusion time, t_m , for the defect located at a particular depth and hence the parameter t_m provides the information of defect depth directly. The value of t_m is obtained from plots of the net change of secondary magnetic field shown in Fig 5.13. The values of $\sqrt{t_m}$ for defects at different depths are plotted in Fig 5.14 and it has been shown that the square root of the diffusion time ($\sqrt{t_m}$) is proportional to the depth of the defect. This is in accordance with eq. (5.4), which states the proportionality between depth of penetration and square root of time. The broadening of the differential secondary magnetic field with respect to decay time along with decreasing amplitude with increasing depth is also evident in Fig 5.13 showing that the eddy currents move downward and outward spatially with decrease in magnitude.

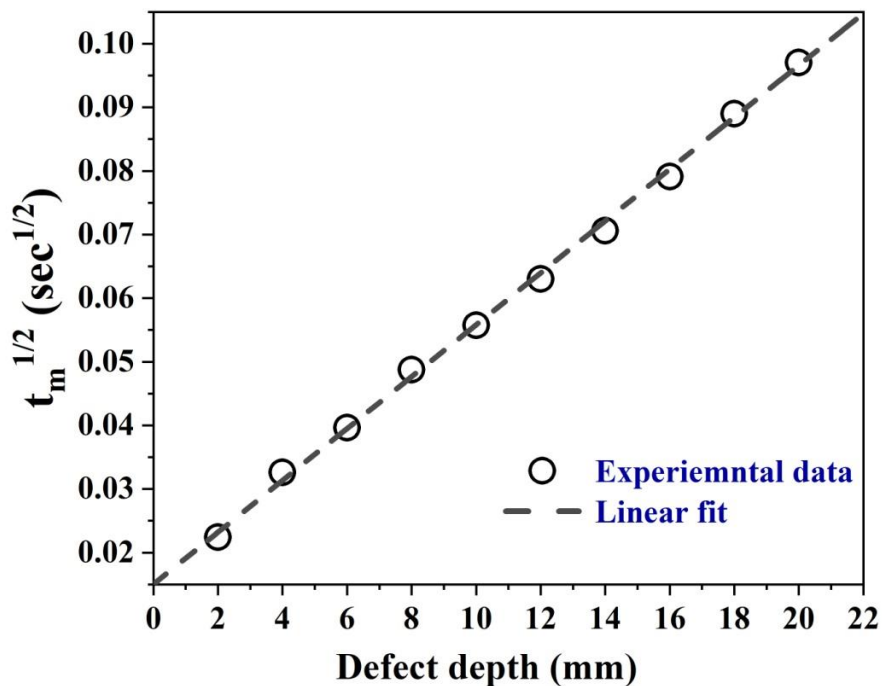


Fig 5.14 Square root of diffusion time (t_m) for defect located at various depths.

5.8. Conclusion

A transient eddy current NDE system has been developed with the combination of fluxgate and double “D” excitation coil. The use of double “D” excitation coil with fluxgate sensor gives larger depth of investigation due to the cancellation of the excitation field at the location of the fluxgate. At the same time, the target experiences larger excitation magnetic field and hence it induces larger eddy currents in the target. In addition to this, the use of fluxgate provides additional advantage of measuring the magnetic field directly instead of using a coil sensor which senses only the time derivative of the magnetic field. The system has been used for the detection of an artificially engineered defect in stacks of aluminum plates at various depths ranging from 2 mm to 20 mm. In this work, we have used fluxgate as a sensor and the other instruments such as transmitter, transmitter controller and data acquisition system used for this work are the same one used for TDEM based geophysical applications. It is found that the time at which the differential secondary magnetic field due to the presence of the defect reaches maximum, also referred as diffusion time, t_m , could be directly correlated to the defect depth. It has also been verified that the square root of the diffusion time ($\sqrt{t_m}$) is proportional to the depth of the defect. The feature diffusion time, t_m , used in this work is one of the parameter in the standard equation of diffusion depth, $\delta = (2t/\sigma\mu)^{1/2}$ which has been derived from the electromagnetic equations and is analogous to the skin depth of the material in frequency domain. Changes of the secondary magnetic field of the order of $0.005 \mu\text{T}$ could be measured using this system in the unshielded and relatively noisy environment.

References

1. Best, M.E. 11.15 - Mineral Resources. In; Schubert, G.B.T.-T. on G. (Second E., Ed.; Elsevier: Oxford, 2015; pp. 525–556 ISBN 978-0-444-53803-1.
2. Gabàs, A.; Macau, A.; Benjumea, B.; Bellmunt, F.; Figueras, S.; Vilà, M. Combination of Geophysical Methods to Support Urban Geological Mapping. *Surv. Geophys.* **2014**, *35*, 983–1002, doi:10.1007/s10712-013-9248-9.
3. Tinivella, U.; Giustiniani, M.; Cassiani, G. Geophysical Methods for Environmental Studies. *Int. J. Geophys.* **2013**, *2013*, 950353, doi:10.1155/2013/950353.
4. Khesin, B. Use of geophysical methods for the solution of environmental problems in Israel. *HAIT J. Sci. Eng. B Issues* **2005**, *2*, 95–124.
5. Zonge International Solve underground problem-geotechnical-environmental Available online: <http://zonge.com/solve-underground-problems/geotechnical-environmental/> (accessed on Mar 13, 2020).
6. Telford, W.M.; Geldart, L.P.; Sheriff, R.E. *Applied Geophysics*; 2nd ed.; Cambridge University Press: Cambridge, 1990; ISBN 9780521339384.
7. Kearey, P.; Brooks, M.; Hill, I.H. An introduction to geophysical exploration.; 1984.
8. Ford Keating, P., and Thomas, M.D., K. *Overview of geophysical signatures associated with Canadian ore deposits*; Geological Survey of Canada: Mineral Deposits Division (St. John's, NL, Canada), 2007;
9. Haldar, S.K. Chapter 6 - Exploration Geophysics. In; Haldar, S.K.B.T.-M.E. (Second E., Ed.; Elsevier, 2018; pp. 103–122 ISBN 978-0-12-814022-2.
10. Aminzadeh, F.; Dasgupta, S.N. Chapter 3 - Fundamentals of Petroleum Geophysics. In *Geophysics for Petroleum Engineers*; Aminzadeh, F., Dasgupta, S.N.B.T.-D. in P.S., Eds.; Elsevier, 2013; Vol. 60, pp. 37–92 ISBN 0376-7361.
11. Paterson, N.R.; Reeves, C. V Applications of gravity and magnetic surveys: The state-of-the-art in 1985. *GEOPHYSICS* **1985**, *50*, 2558–2594, doi:10.1190/1.1441884.
12. Metje, N.; Atkins, P.R.; Brennan, M.J.; Chapman, D.N.; Lim, H.M.; Machell, J.; Muggleton, J.M.; Pennock, S.; Ratcliffe, J.; Redfern, M.; et al. Mapping the

- Underworld - State-of-the-art review. *Tunn. Undergr. Sp. Technol.* **2007**, 22, 568–586, doi:10.1016/j.tust.2007.04.002.
13. Cook, S.E.; Corner, R.J.; Groves, P.R.; Grealish, G.J. Use of airborne gamma radiometric data for soil mapping. *Aust. J. Soil Res.* **1996**, 34, 183–194, doi:10.1071/SR9960183.
 14. Beamish, D.; White, J.C. Proceedings of the Geologists ' Association A radiometric airborne geophysical survey of the Isle of Wight. **2011**, 122, 787–799.
 15. Nabighian, M.N.; Grauch, V.J.S.; Hansen, R.O.; LaFehr, T.R.; Li, Y.; Peirce, J.W.; Phillips, J.D.; Ruder, M.E. The historical development of the magnetic method in exploration. *Geophysics* **2005**, 70, doi:10.1190/1.2133784.
 16. DC resistivity: measurements and data Available online: https://www.eoas.ubc.ca/ubcgif/iag/methods/meth_1/measurements.htm (accessed on Jan 25, 2021).
 17. Plank, Z.; Polgár, D. Application of the DC resistivity method in urban geological problems of karstic areas. *Near Surf. Geophys.* **2019**, 17, 547–561, doi:10.1002/nsg.12062.
 18. Georgsson, L.; Karlsdóttir, R. Resistivity methods - DC AND TEM with examples and Comparison from the Reykjanes Peninsula AND Oxarfjordur, Iceland.; 2014.
 19. Lkhagvasuren, S. Resistivity surveying in Geothermal Exploration with an application to the Eyjafjordur Low-temperature area , N-Iceland.; 2017.
 20. Spies, B.R. Depth of investigation in electromagnetic sounding methods. *GEOPHYSICS* **1989**, 54, 872–888, doi:10.1190/1.1442716.
 21. Lowe, S.; Chitolie, J.; Pearce, J.M.; Welsh, A. To Hydrocarbon Exploration. **2006**, 74.
 22. Moore, P.O.; Allgaier, M.W.; Cameron, R.E. *Visual Testing - Nondestructive Testing Handbook*; Moore, P.O., Ed.; 3rd ed.; American Society for Nondestructive Testing, 2010; Vol. 9; ISBN 9781571171863.
 23. Anastasopoulos, A.A.; Kourousis, D.A.; Cole, P.T. Acoustic emission inspection of spherical metallic pressure vessels. ... *Tech. Insp.* ... **2008**.
 24. Scruby, C.B. An introduction to acoustic emission. *J. Phys. E.* **1987**, 20, 946–953,

- doi:10.1088/0022-3735/20/8/001.
25. Moore, P.O.; Tracy, N.A. *Liquid Penetrant Testing - Nondestructive Testing Handbook*; Moore, P.O., Tracy, N.A., Eds.; 3rd ed.; American Society for Nondestructive Testing, 1999; Vol. 2; ISBN 9781571170286.
 26. Schmidt, J.T.; Skeie, K. *Magnetic Particle Testing - Nondestructive Testing Handbook*; Schmidt, J.T., Skeie, K., Eds.; 2nd ed.; American Society for Nondestructive Testing, 1989; Vol. 6; ISBN 9780471684220.
 27. Bossi, R.H.; Iddings, F.A.; Wheeler, G.C. *Nondestructive Testing Handbook, Volume 4 , Radiographic Testing*; Bossi, R.H., Iddings, F.A., Wheeler, G.C., Eds.; 3rd ed.; American Society for Nondestructive Testing, 2002; ISBN 1571170466.
 28. Qu, Z.; Jiang, P.; Zhang, W. Development and application of infrared thermography non-destructive testing techniques. *Sensors (Switzerland)* **2020**, *20*, 1–27, doi:10.3390/s20143851.
 29. Moore, P.O.; Workman, G.L.; Kishoni, D. *ASNT Ultrasonic.pdf*; 3rd ed.; American Society for Nondestructive Testing, 2007;
 30. Udpa, S.S.; Moore, P.O. *Principles of electromagnetic testing*; 3rd ed.; American Society for Nondestructive Testing, 2004; Vol. 5; ISBN 1571170464.
 31. Vozoff, K. 8. The Magnetotelluric Method. In *Electromagnetic Methods in Applied Geophysics: Volume 2, Application, Parts A and B*; Investigations in Geophysics; Society of Exploration Geophysicists, 1991; pp. 641–712 ISBN 978-1-56080-022-4.
 32. Vozoff, K. The Magnetotelluric method in the exploration of Sedimentary Basins. *GEOPHYSICS* **1972**, *37*, 98–141, doi:10.1190/1.1440255.
 33. Siemon, B. Electromagnetic methods – frequency domain BT - Groundwater Geophysics: A Tool for Hydrogeology. In; Kirsch, R., Ed.; Springer Berlin Heidelberg: Berlin, Heidelberg, 2009; pp. 155–178 ISBN 978-3-540-88405-7.
 34. Spies, B.R. Depth of investigation in 1989, *54*, 872–888.
 35. Bai, L.; Yun Tian, G.; Simm, A.; Tian, S.; Cheng, Y. Fast crack profile reconstruction using pulsed eddy current signals. *NDT E Int.* **2013**, *54*, 37–44, doi:https://doi.org/10.1016/j.ndteint.2012.11.003.

36. Sheard, S.N.; Ritchie, T.J.; Christopherson, K.R.; Brand, E. Mining, Environmental, Petroleum, and Engineering Industry Applications of Electromagnetic Techniques in Geophysics. *Surv. Geophys.* **2005**, *26*, 653–669, doi:10.1007/s10712-005-1760-0.
37. Smith, R. Electromagnetic Induction Methods in Mining Geophysics from 2008 to 2012. *Surv. Geophys.* **2014**, *35*, 123–156, doi:10.1007/s10712-013-9227-1.
38. Goldman, M.; Neubauer, F.M. Groundwater exploration using integrated geophysical techniques. *Surv. Geophys.* **1994**, *15*, 331–361, doi:10.1007/BF00665814.
39. Fitterman, D. V Mapping Saltwater Intrusion in the Biscayne Aquifer, Miami-Dade County, Florida using Transient Electromagnetic Sounding. *J. Environ. Eng. Geophys.* **2014**, *19*, 33–43, doi:10.2113/JEEG19.1.33.
40. Nabighian, M.N.; Macnae, J.C. 6. Time Domain Electromagnetic Prospecting Methods. In *Electromagnetic Methods in Applied Geophysics: Volume 2, Application, Parts A and B*; Investigations in Geophysics; Society of Exploration Geophysicists, 1991; pp. 427–520 ISBN 978-1-56080-022-4.
41. Sophian, A.; Tian, G.Y.; Taylor, D.; Rudlin, J. Electromagnetic and eddy current NDT: A review. *Insight Non-Destructive Test. Cond. Monit.* **2001**, *43*, 302–306.
42. Bray, D.E.; Stanley, R.K. *Nondestructive Evaluation—a Tool in Design, Manufacturing and Service.*; CRC Press Inc, 1997; ISBN 9781498711050.
43. Thollon, F.; Burais, N. Geometrical optimization of sensors for eddy currents. Non destructive testing and evaluation. *IEEE Trans. Magn.* **1995**, *31*, 2026–2031, doi:10.1109/20.376441.
44. Lebrun, B.; Jayet, Y.; Baboux, J.-C. Pulsed eddy current signal analysis: application to the experimental detection and characterization of deep flaws in highly conductive materials. *NDT E Int.* **1997**, *30*, 163–170, doi:https://doi.org/10.1016/S0963-8695(96)00072-2.
45. Mottl, Z. The quantitative relations between true and standard depth of penetration for air-cored probe coils in eddy current testing. *NDT Int.* **1990**, *23*, 11–18, doi:https://doi.org/10.1016/0308-9126(90)91444-X.
46. Blitz, J.; Peat, T.S. The application of multi-frequency eddy currents to testing ferromagnetic metals. *NDT Int.* **1981**, *14*, 15–17, doi:https://doi.org/10.1016/0308-

- 9126(81)90058-4.
47. Avanindra Multifrequency eddy current signal analysis, Iowa State University, 1997.
 48. Michniakova, M.; Janousek, L. The impact of various waveform shapes on the response signal in pulsed eddy current NDE. In Proceedings of the 2012 ELEKTRO; 2012; pp. 439–442.
 49. Li, J.; Wu, X.; Zhang, Q.; Sun, P. Pulsed eddy current testing of ferromagnetic specimen based on variable pulse width excitation. *NDT E Int.* **2015**, *69*, 28–34, doi:<https://doi.org/10.1016/j.ndteint.2014.09.004>.
 50. Li, Y.; Yan, B.; Li, D.; Jing, H.; Li, Y.; Chen, Z. Pulse-modulation eddy current inspection of subsurface corrosion in conductive structures. *NDT E Int.* **2016**, *79*, 142–149, doi:<https://doi.org/10.1016/j.ndteint.2016.02.001>.
 51. Blitz, J. Eddy current testing of metals. *Mater. Des.* **1987**, *8*, 340–345, doi:[https://doi.org/10.1016/0261-3069\(87\)90084-7](https://doi.org/10.1016/0261-3069(87)90084-7).
 52. Park, D.G.; Angani, C.S.; Cheong, Y.M. Differential Pulsed eddy current probe to detect the sub surface Cracks in a Stainless Steel Pipe. In Proceedings of the 18th World Conference on Nondestructive Testing; 2012; pp. 16–20.
 53. He, Y.; Luo, F.; Pan, M.; Weng, F.; Hu, X.; Gao, J.; Liu, B. Pulsed eddy current technique for defect detection in aircraft riveted structures. *NDT E Int.* **2010**, *43*, 176–181, doi:<https://doi.org/10.1016/j.ndteint.2009.10.010>.
 54. Yang, G.; Tamburrino, A.; Udpa, L.; Udpa, S.S.; Zeng, Z.; Deng, Y.; Que, P. Pulsed Eddy-Current Based Giant Magnetoresistive System for the Inspection of Aircraft Structures. *IEEE Trans. Magn.* **2010**, *46*, 910–917, doi:[10.1109/TMAG.2009.2032330](https://doi.org/10.1109/TMAG.2009.2032330).
 55. He, Y.; Luo, F.; Pan, M.; Hu, X.; Gao, J.; Liu, B. Defect classification based on rectangular pulsed eddy current sensor in different directions. *Sensors Actuators A Phys.* **2010**, *157*, 26–31, doi:<https://doi.org/10.1016/j.sna.2009.11.012>.
 56. Arjun, V.; Sasi, B.; Rao, B.P.C.; Mukhopadhyay, C.K.; Jayakumar, T. Optimisation of pulsed eddy current probe for detection of sub-surface defects in stainless steel plates. *Sensors Actuators A Phys.* **2015**, *226*, 69–75, doi:<https://doi.org/10.1016/j.sna.2015.02.018>.

57. Zhou, D.; Wang, J.; He, Y.; Chen, D.; Li, K. Influence of metallic shields on pulsed eddy current sensor for ferromagnetic materials defect detection. *Sensors Actuators A Phys.* **2016**, *248*, 162–172, doi:<https://doi.org/10.1016/j.sna.2016.07.029>.
58. Ripka, P.; Janosek, M. Advances in Magnetic Field Sensors. *IEEE Sens. J.* **2010**, *10*, 1108–1116, doi:[10.1109/JSEN.2010.2043429](https://doi.org/10.1109/JSEN.2010.2043429).
59. Ward, S.H.; Hohmann, G.W. 4. Electromagnetic Theory for Geophysical Applications. In *Electromagnetic Methods in Applied Geophysics: Volume 1, Theory*; Investigations in Geophysics; Society of Exploration Geophysicists, 1988; pp. 130–311 ISBN 978-0-931830-51-8.
60. Angani, C.S.; Park, D.G.; Kim, C.G.; Leela, P.; Kishore, M.; Cheong, Y.M. Pulsed eddy current differential probe to detect the defects in a stainless steel pipe. *J. Appl. Phys.* **2011**, *109*, 07D348, doi:[10.1063/1.3540409](https://doi.org/10.1063/1.3540409).
61. Kim, J.; Yang, G.; Udpa, L.; Udpa, S. Classification of pulsed eddy current GMR data on aircraft structures. *NDT E Int.* **2010**, *43*, 141–144, doi:<https://doi.org/10.1016/j.ndteint.2009.10.003>.
62. Cheng, W. Pulsed Eddy Current Testing of Carbon Steel Pipes' Wall-thinning Through Insulation and Cladding. *J. Nondestruct. Eval.* **2012**, *31*, 215–224, doi:[10.1007/s10921-012-0137-9](https://doi.org/10.1007/s10921-012-0137-9).
63. Li, Y.; Tian, G.Y.; Simm, A. Fast analytical modelling for pulsed eddy current evaluation. *NDT E Int.* **2008**, *41*, 477–483, doi:<https://doi.org/10.1016/j.ndteint.2008.02.001>.
64. Panaitov, G.; Krause, H.-J.; Zhang, Y. Pulsed eddy current transient technique with HTS SQUID magnetometer for non-destructive evaluation. *Phys. C Supercond.* **2002**, *372–376*, 278–281, doi:[https://doi.org/10.1016/S0921-4534\(02\)00696-2](https://doi.org/10.1016/S0921-4534(02)00696-2).
65. Ji, Y.; Du, S.; Xie, L.; Chang, K.; Liu, Y.; Zhang, Y.; Xie, X.; Wang, Y.; Lin, J.; Rong, L. TEM measurement in a low resistivity overburden performed by using low temperature SQUID. *J. Appl. Geophys.* **2016**, *135*, 243–248, doi:<https://doi.org/10.1016/j.jappgeo.2016.09.027>.
66. Bartington, G.; Chapman, C.E. A high-stability fluxgate magnetic gradiometer for shallow geophysical survey applications. *Archaeol. Prospect.* **2004**, *11*, 19–34, doi:[10.1002/arp.219](https://doi.org/10.1002/arp.219).

67. Nabighian, M.N. Quasi-static transient response of a conducting half-space— An approximate representation. *GEOPHYSICS* **1979**, *44*, 1700–1705, doi:10.1190/1.1440931.
68. Chen, C.; Liu, F.; Lin, J.; Zhu, K.; Wang, Y. An optimized air-core coil sensor with a magnetic flux compensation structure suitable to the helicopter TEM system. *Sensors (Switzerland)* **2016**, *16*, doi:10.3390/s16040508.
69. Dehmel, G. Magnetic Field Sensors: Induction Coil (Search Coil) Sensors. *Sensors Set* 1995, 205–253.
70. (ed), P.R. Magnetic Sensors and Magnetometers. *Meas. Sci. Technol.* **2002**, *13*, 645, doi:10.1088/0957-0233/13/4/707.
71. Cavoit, C. Closed loop applied to magnetic measurements in the range of 0.1–50MHz. *Rev. Sci. Instrum.* **2006**, *77*, 64703, doi:10.1063/1.2214693.
72. Tumanski, S. Induction coil sensors—a review. *Meas. Sci. Technol.* **2007**, *18*, R31–R46, doi:10.1088/0957-0233/18/3/r01.
73. Breiner, S. Magnetometers for Geophysical Applications. *SQUID Appl. to Geophys.* 1981, 0.
74. Primdahl, F. The Fluxgate Magnetometer. *J. Phys. E.* **2001**, *12*, 241, doi:10.1088/0022-3735/12/4/001.
75. Matsuoka, A.; Shinohara, M.; Tanaka, Y.-M.; Fujimoto, A.; Iguchi, K. Development of fluxgate magnetometers and applications to the space science missions. In *An Introduction to Space Instrumentation*; TERRAPUB, 2013; pp. 217–225.
76. Drung, D. High-Tc and low-Tc dc SQUID electronics. *Supercond. Sci. Technol.* **2003**, *16*, 1320–1336, doi:10.1088/0953-2048/16/12/002.
77. Lee, S.-Y. Multi-channel Scanning SQUID microscopy, University of Maryland, 2004.
78. Nagendran, R.; Thirumurugan, N.; Chinnasamy, N.; Janawadkar, M.P.; Sundar, C.S. Development of high field SQUID magnetometer for magnetization studies up to 7 T and temperatures in the range from 4.2 to 300 K. *Rev. Sci. Instrum.* **2011**, *82*, 15109, doi:10.1063/1.3519017.

79. Nagendran, R.; Janawadkar, M.P.; Pattabiraman, M.; Baisnab, D.K.; Jayapandian, J.; Baskaran, R.; Vaidhyanathan, L.S.; Hariharan, Y.; Nagesha, A.; Valsan, M.; et al. Development of SQUID-Based System for Nondestructive Evaluation. *IEEE Trans. Appl. Supercond.* **2007**, *17*, 3824–3829, doi:10.1109/TASC.2007.902112.
80. Nagendran, R.; Thirumurugan, N.; Chinnasamy, N.; Janawadkar, M.P.; Baskaran, R.; Vaidhyanathan, L.S.; Sundar, C.S. Optimum eddy current excitation frequency for subsurface defect detection in SQUID based non-destructive evaluation. *NDT E Int.* **2010**, *43*, 713–717, doi:https://doi.org/10.1016/j.ndteint.2010.08.003.
81. Fagaly, R.L. Superconducting quantum interference device instruments and applications. *Rev. Sci. Instrum.* **2006**, *77*, 1–45, doi:10.1063/1.2354545.
82. Trabesinger, A.H.; McDermott, R.; Lee, S.; Mück, M.; Clarke, J.; Pines, A. SQUID-Detected Liquid State NMR in Microtesla Fields. *J. Phys. Chem. A* **2004**, *108*, 957–963, doi:10.1021/jp035181g.
83. Drung, D.; Cantor, R.; Peters, M.; Scheer, H.J.; Koch, H. Low-noise high-speed dc superconducting quantum interference device magnetometer with simplified feedback electronics. *Appl. Phys. Lett.* **1990**, *57*, 406–408, doi:10.1063/1.103650.
84. MAGNICON, Available online: <http://www.magnicon.com/squid-sensors/magnetometers/> (accessed on Sep 30, 2020).
85. Zonge International Available online: <http://zonge.com/instruments-home/instruments/transmitters/> (accessed on Sep 25, 2020).
86. EMIT Available online: <https://www.electromag.com.au/#> (accessed on Sep 25, 2020).
87. Burger, H.R.; Burger, D.C. Exploration geophysics of the shallow subsurface 1992.
88. Grimm, R.E. A comparison of time domain electromagnetic and surface nuclear magnetic resonance sounding for subsurface water on Mars. *J. Geophys. Res. E Planets* **2003**, *108*, 1–10, doi:10.1029/2002je001882.
89. Petr, I.; Kuzmin, V.; Morrison, E.B.; Anderson, B.; Nilsson, B. (12) United States Patent 2011, 2.
90. Adams, W.M. Interpretation Theory in Applied Geophysics: F. S. Grant and G. F. West. McGraw-Hill Book Company, April 1965. 583 pp. \$17.50. *Bull. Seismol.*

- Soc. Am.* **1965**, 55, 1060.
91. Asten, M.W.; Duncan, A.C. The quantitative advantages of using B-field sensors in time-domain EM measurement for mineral exploration and unexploded ordnance search. *GEOPHYSICS* **2012**, 77, WB137–WB148, doi:10.1190/geo2011-0385.1.
 92. Goswami, S.; Bhagat, S.; Zakaulla, S.; Kumar, S.; Rai, A.K. Role of organic matter in uranium mineralisation in Vempalle dolostone; Cuddapah basin, India. *J. Geol. Soc. India* **2017**, 89, 145–154, doi:10.1007/s12594-017-0578-y.
 93. Ajay, G.; Rao, K.K.; Vijay, K.K.S.; Raju, G.D.; Venkateswarlu, V.; Bharath, K.A.Y. Rock mechanics investigations at Tummalapalle Uranium Mine of UCIL, AP BT - Recent Advances in Rock Engineering (RARE 2016).; Atlantis Press, 2016; pp. 501–504.
 94. Panaitov, G.; Bick, M.; Zhang, Y.; Krause, H. -J. Peculiarities of SQUID magnetometer application in TEM. *GEOPHYSICS* **2002**, 67, 739–745, doi:10.1190/1.1484516.
 95. Chwala, A.; Stolz, R.; Ramos, J.; Schultze, V.; Meyer, H.-G.; Kretzschmar, D. An HTS dc SQUID system for geomagnetic prospection. *Supercond. Sci. Technol.* **1999**, 12, 1036–1038, doi:10.1088/0953-2048/12/11/403.
 96. Palacky, G.J. 3. Resistivity Characteristics of Geologic Targets. In *Electromagnetic Methods in Applied Geophysics: Volume 1, Theory*; Investigations in Geophysics; Society of Exploration Geophysicists, 1988; pp. 52–129 ISBN 978-0-931830-51-8.
 97. Wang, X.C.; Zhang, J.; Zheng, X.P.; Deng, X.H.; Wu, J.J.; Yang, Y. Application of fluxgate sensor in TEM prospecting. *Wutan Huatan Jisuan Jishu* **2014**, 36, 649–654, doi:10.3969/j.issn.1001-1749.2014.06.02.
 98. Roux, L. SQUID sensors for EM systems. *Africa (Lond)*. **2007**, 417–423.
 99. Andò, B.; Baglio, S.; Bulsara, A.R.; Trigona, C. Design and characterization of a microwire fluxgate magnetometer. *Sensors Actuators A Phys.* **2009**, 151, 145–153, doi:https://doi.org/10.1016/j.sna.2009.02.029.
 100. Rao, B.P.C. *Practical Eddy Current Testing*; Alpha Sceince International, 2007; ISBN 978-1-84265-299-2.
 101. Roy, D.; Chakroborty, R.; Kaushik, B.K. Comparative study of E-shaped coil and

- evolution of new methodology for crack detection using eddy current testing. *Insight* **2013**, 55, 553–557.
102. Kriezis, E.E.; Tsiboukis, T.D.; Panas, S.M.; Tegopoulos, J.A. Eddy currents: theory and applications. *Proc. IEEE* **1992**, 80, 1559–1589, doi:10.1109/5.168666.
103. Zhang, K.; He, Y.; Dong, Z. Pulsed Eddy Current Nondestructive Testing for Defect Evaluation and Imaging of Automotive Lightweight Alloy Materials. *J. Sensors* **2018**, 2018, 1639387, doi:10.1155/2018/1639387.
104. Moulder, J.C.; Bieber, J.A.; III, W.W.W.; Rose, J.H. Scanned pulsed eddy current instrument for nondestructive inspection of aging aircraft. In Proceedings of the Proc.SPIE; 1996; Vol. 2945.
105. Park, D.G.; Angani, C.S.; Kim, G.D.; Kim, C.G.; Cheong, Y.M. Evaluation of Pulsed Eddy Current Response and Detection of the Thickness Variation in the Stainless Steel. *IEEE Trans. Magn.* **2009**, 45, 3893–3896, doi:10.1109/TMAG.2009.2024219.
106. Xu, Z.; Wu, X.; Li, J.; Kang, Y. Assessment of wall thinning in insulated ferromagnetic pipes using the time-to-peak of differential pulsed eddy-current testing signals. *NDT E Int.* **2012**, 51, 24–29, doi:https://doi.org/10.1016/j.ndteint.2012.07.004.
107. Xie, S.; Chen, Z.; Takagi, T.; Uchimoto, T. Quantitative non-destructive evaluation of wall thinning defect in double-layer pipe of nuclear power plants using pulsed ECT method. *NDT E Int.* **2015**, 75, 87–95, doi:https://doi.org/10.1016/j.ndteint.2015.06.002.
108. Král, J.; Smid, R.; Ramos, H.M.G.; Ribeiro, A.L. Thickness measurement using transient eddy current techniques. *Conf. Rec. - IEEE Instrum. Meas. Technol. Conf.* **2011**, 138–143, doi:10.1109/IMTC.2011.5944293.
109. Hosseini, S.; Lakis, A.A. Application of time–frequency analysis for automatic hidden corrosion detection in a multilayer aluminum structure using pulsed eddy current. *NDT E Int.* **2012**, 47, 70–79, doi:https://doi.org/10.1016/j.ndteint.2011.12.001.
110. He, Y.; Tian, G.; Zhang, H.; Alamin, M.; Simm, A.; Jackson, P. Steel Corrosion Characterization Using Pulsed Eddy Current Systems. *IEEE Sens. J.* **2012**, 12,

- 2113–2120, doi:10.1109/JSEN.2012.2184280.
111. Skramstad, J.; Smith, R.; Harrison, D. Enhanced detection of deep corrosion using transient eddy currents. In Proceedings of the Proc. 7th Joint DoD/FAA/NASA Conference on Aging Aircraft; 2003.
 112. Sophian, A.; Tian, G.Y.; Taylor, D.; Rudlin, J. Design of a pulsed eddy current sensor for detection of defects in aircraft lap-joints. *Sensors Actuators A Phys.* **2002**, *101*, 92–98, doi:[https://doi.org/10.1016/S0924-4247\(02\)00195-4](https://doi.org/10.1016/S0924-4247(02)00195-4).
 113. He, Y.; Luo, F.; Pan, M.; Hu, X.; Gao, J.; Liu, B. Defect classification based on rectangular pulsed eddy current sensor in different directions. *Sensors Actuators, A Phys.* **2010**, *157*, 26–31, doi:10.1016/j.sna.2009.11.012.
 114. Smith, R.; Hugo, G.R. Transient eddy current NDE for ageing aircraft - capabilities and limitations January. *Insight - Non-Destructive Test. Cond. Monit.* **2001**, *43*.
 115. Zhou, D.; Zhang, B.; Tian, G.; Wang, H. Research on Surface Defect Detection Using Pulsed Eddy Current Testing Technology. **2008**, 25–28.
 116. Tian, G.Y.; Sophian, A. Defect classification using a new feature for pulsed eddy current sensors. *NDT E Int.* **2005**, *38*, 77–82, doi:10.1016/j.ndteint.2004.06.001.
 117. Li, Y.; Yan, B.; Li, D.; Li, Y.; Zhou, D. Gradient-field pulsed eddy current probes for imaging of hidden corrosion in conductive structures. *Sensors Actuators A Phys.* **2016**, *238*, 251–265, doi:<https://doi.org/10.1016/j.sna.2015.12.026>.
 118. Kambala, S.R. Studies on Development of a Pulsed Eddy Current System for Testing Thick Stainless Steel Components, HBNI, 2017.
 119. Primdahl, F. The fluxgate magnetometer. *J. Phys. E.* **1979**, *12*, 241–253, doi:10.1088/0022-3735/12/4/001.
 120. Bartington Available online: <https://www.bartington.com/mag-03/> (accessed on Aug 18, 2020).

Thesis Highlight

Name of the Student: ljee Mohanty

Name of CI: Indira Gandhi Centre for Atomic Research **Enrolment No.:** PHYS02201504016

Thesis Title: Development of TDEM system with SQUID and fluxgate for geophysical and NDE applications

Discipline: Physical Sciences

Sub-Area of Discipline: SQUID sensor, Geophysics, NDE

Date of viva voce: 18/06/2021

- A Superconducting Quantum Interference Device (SQUID) based Time Domain Electromagnetic (TDEM) system is developed and tested at laboratory level using aluminum plates as conducting target (Fig 1). The performance of the system was compared with an in-house developed induction coil sensor.
- Central loop sounding measurements were performed using SQUID based system at Tumallapalle where the terrain consists of a thin conductive shale layer buried below a thick resistive layer. The measurements performed using different transmitter loops showed that SQUID is the best magnetic eye to visualize the conducting object located far below the earth surface (Fig 2).
- Dual behavior of fluxgate magnetometer was observed during TDEM measurements. On further experiment, it was confirmed that he fluxgate magnetometer works as an induction coil at early time (measuring voltage directly) and as magnetometer (measuring magnetic field) at later time (Fig 3).
- A transient eddy current non-destructive evaluation (NDE) system is developed with the combination of fluxgate and double "D" excitation coil and used for the detection of defect in aluminum plates at various depths ranging from 2 mm to 20 mm. A direct correlation between the diffusion time of eddy current and depth of the defect is established using this technique(Fig. 4)

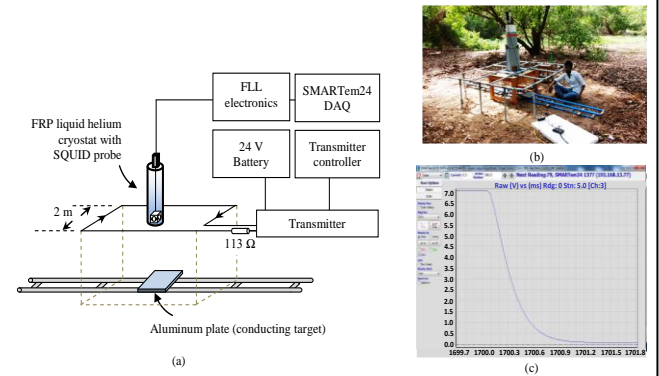


Fig.1 Test of SQUID based TDEM system using Al plates

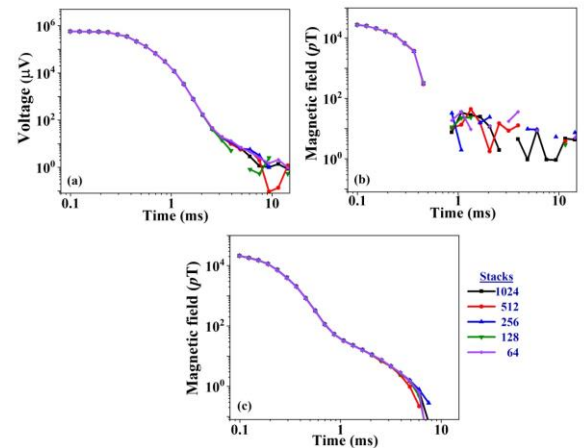


Fig.2 Decay plots showing vertical component of magnetic field recorded with (a) coil, (b) fluxgate and (c) SQUID

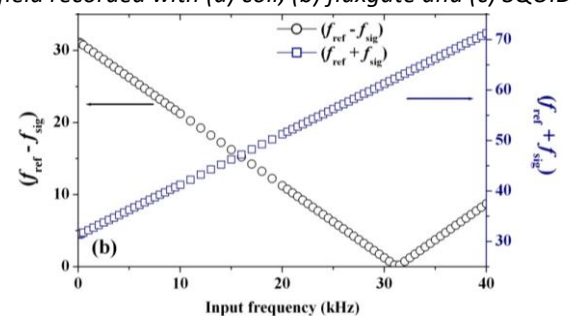


Fig.3 Frequency of different predominant peak voltages at given input frequencies.

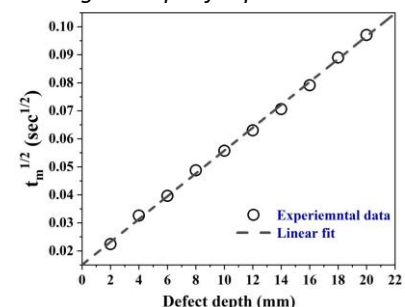


Fig.4 Square root of diffusion time (t_m) for defect located at various depths